Electron vortices: Beams with orbital angular momentum

S. M. Lloyd, M. Babiker,* G. Thirunavukkarasu, and J. Yuan†

Department of Physics, University of York, Heslington, York, YO10 5DD, United Kingdom

(published 16 August 2017)

The recent prediction and subsequent creation of electron vortex beams in a number of laboratories occurred after almost 20 years had elapsed since the recognition of the physical significance and potential for applications of the orbital angular momentum carried by optical vortex beams. A rapid growth in interest in electron vortex beams followed, with swift theoretical and experimental developments. Much of the rapid progress can be attributed in part to the clear similarities between electron optics and photonics arising from the functional equivalence between the Helmholtz equations governing the free-space propagation of optical beams and the time-independent Schrödinger equation governing freely propagating electron vortex beams. There are, however, key differences in the properties of the two kinds of vortex beams. This review is primarily concerned with the electron type, with specific emphasis on the distinguishing vortex features: notably the spin, electric charge, current and magnetic moment, the spatial distribution, and the associated electric and magnetic fields. The physical consequences and potential applications of such properties are pointed out and analyzed, including nanoparticle manipulation and the mechanisms of orbital angular momentum transfer in the electron vortex interaction with matter.

DOI: 10.1103/RevModPhys.89.035004

CONTENTS

*m.babiker@york.ac.uk
†jun.yuan@york.ac.uk

I. INTRODUCTION

Electron vortex beams are a new member of an expanding class of experimentally realizable freely propagating vortex states having well-defined orbital angular momentum (OAM) about their propagation axis, the prototypical example of which is the much studied optical vortex beam. The term vortex beam refers to a beam of particles (electrons, photons, or otherwise) that is freely propagating and possesses a wave front with quantized topological structure arising from a

singularity in phase taking the form $e^{il\phi}$ with ϕ the azimuthal angle about the beam axis and l an integer quantum number also known as the topological charge (or winding number). The topological structure of the wave front was first described by Nye and Berry (1974) as a screw-type dislocation in the wave trains in analogy with crystal defects.

Over the last two decades optical vortices have been a subject of much interest, after the publication of the seminal work of Allen *et al.* (1992) in which the quantized orbital angular momentum of a Laguerre-Gaussian (LG) laser mode was examined [the earlier discussion of optical vortices in laser modes by Coullet, Gil, and Rocca (1989) did not emphasize the quantization of the orbital angular momentum about the propagation axis]. Since then, optical vortices have been intensively studied leading to many diverse applications (Allen, Padgett, and Babiker, 1999; Allen, Barnett, and Padgett, 2003; Andrews and Babiker, 2012), including optical tweezers and spanners for various applications (He *et al.*, 1995; Dholakia *et al.*, 2002; Grier, 2003; Ladavac and Grier, 2004): micromanipulation (Galajda and Ormos, 2001); classical and quantum communications (Yao and Padgett, 2011); phase contrast imaging in microscopy (Fürhapter *et al.*, 2005; Züchner, Failla, and Meixner, 2011; Baranek and Bouchal, 2013); and further proposed applications in quantum information and metrology (Molina-Terriza, Torres, and Torner, 2007; Yao and Padgett, 2011) and astronomy (Lee *et al.*, 2006; Thidé *et al.*, 2007; Tamburini *et al.*, 2011). The discussion of photonic spin and orbital angular momentum in various situations and the similarities and differences between the two types of angular momentum have led to new ways of thinking about and examining orbital angular momentum in this context. The spin and orbital angular momentum cannot be clearly separated in general, i.e., without the imposition of the paraxial approximation (Barnett and Allen, 1994; Van Enk and Nienhuis, 1994; O'Neil *et al.*, 2002), which leads to the possibility of the entanglement of the 2 degrees of freedom (Mair *et al.*, 2001; Khoury and Milman, 2011). More subtle quantum effects due to the interaction of optical vortices with atoms and molecules involve internal atomic transitions at near resonance with the beam frequency. Here too optical forces and torques are at play (Babiker, Power, and Allen, 1994; Allen *et al.*, 1996; Andersen *et al.*, 2006; Lembessis, Ellinas, and Babiker, 2011; Surzhykov *et al.*, 2015), leading to the trapping and manipulation of individual atoms in certain regions of the beam profile, with promising applications in the new field of atomtronics (Andersen *et al.*, 2006; Seaman *et al.*, 2007; Pepino *et al.*, 2010; Lembessis and Babiker, 2013), as well as the proposed generation of atom vortex beams (Hayrapetyan *et al.*, 2013; Lembessis *et al.*, 2014). A related recent advance in matter vortex beams is the realization of neutron vortex beams in the laboratory (Clark *et al.*, 2015).

Although the basic concepts in terms of beam formation of electron vortices essentially stem from those encountered in the optical vortex case, the electron vortex is distinguished by additional properties, most notably the electric charge and half-integer spin. They are thus fermion vortex states characterized by a scalar field in the form of the Schrödinger wave function for nonrelativistic electrons and Dirac spinors for the ultrarelativistic electron beams, while optical vortex beams are bosonic states described by vector fields. Furthermore, there are substantial differences in scale. Currently, electron vortices created in a medium-voltage (100–300 kV) electron microscope have de Broglie wavelengths of the order of picometers while optical vortices in the visible range have wavelengths of the order of several hundreds of nanometers. Electron vortex beams can thus probe much smaller features than is possible for the optical vortex beams, and as such the range of applications of electron vortices is predicted to be substantially different from the existing scope of optical vortex beams.

The earliest work on particle vortex lines is due to Bialynicki-Birula, Bialynicka-Birula, and Śliwa (2000), Bialynicki-Birula and Bialynicka-Birula (2001), and Bialynicki-Birula *et al.* (2001). The current research activity specifically in electron vortex beams and their OAM content was stimulated by work due to Bliokh *et al.* (2007), shortly followed by the experimental realization in several laboratories (Uchida and Tonomura, 2010; Verbeeck, Tian, and Schattschneider, 2010; McMorran *et al.*, 2011). It has now been established that electron vortices can be created inside electron microscopes and there exist a number of techniques for vortex beam creation, including computer generated holographic masks applied in similar ways to those routinely adopted in the creation of optical vortex beams (Heckenberg, McDuff, Smith, Rubinsztein-Dunlop, and Wegener, 1992; Heckenberg, McDuff, Smith, and White, 1992). This review aims to describe the recent developments in the expanding field of electron vortex physics and highlights significant areas of potential applications. Specifically, electron vortex beams are hoped to lead to novel applications in microscopical analysis, where the orbital angular momentum of the beam is expected to provide new information about the crystallographic, electronic, and magnetic composition of the sample. Chiral-dependent electron diffraction has been detected (Juchtmans *et al.*, 2015; Juchtmans, Guzzinati, and Verbeeck, 2016) as well as the demonstration of magnetic-dependent electron energy-loss spectroscopy (EELS) (Verbeeck, Tian, and Schattschneider, 2010), and it is predicted that the high resolution achievable in the electron microscope will lead to the ability to map magnetic information at atomic or near-atomic resolution. Additionally, the inherent phase structure of the vortex is considered ideal for applications in high resolution phase contrast imaging, as required for biological specimens with low absorption contrast (Jesacher *et al.*, 2005). Applications of electron vortex beams are, however, not restricted to diffraction, spectroscopy, and imaging—the orbital angular momentum of the beam may also be used for the manipulation of nanoparticles (Gnanavel, Yuan, and Babiker, 2012; Verbeeck, Tian, and Tendeloo, 2013), leading to electron spanners analogous to the widely used optical tweezers and spanners. Electron vortex states are also relevant in the context of quantum information and, in particular, the electron vortex may potentially be used to impart angular momentum into vortices in Bose-Einstein condensates (Fetter, 2001). The orbital angular momentum and magnetic properties of the electron vortex may also find potential uses in spintronic applications, either in the characterization of spintronic devices or in contexts employing

spin-polarized current injection, through spin-to-orbital angular momentum conversion processes (Karimi *et al.*, 2012).

Our aim in writing this review has been to strive to provide a report on the current state of the new subject of electron vortex beams and their interactions. We endeavored to survey much of the relevant literature, but any omissions of specific references would certainly be inadvertent and we apologize for not having come across them. For more focused prospectives, the interested reader can consult recently published papers on the subject (Verbeeck *et al.*, 2014; Harris *et al.*, 2015; Bliokh *et al.*, 2017).

The outline of this review is as follows: Sec. II introduces the quantum mechanics governing the propagation of electron vortex beams, namely, the wave equation discussed in the nonrelativistic and relativistic regimes. The mechanical and electromagnetic properties arising from the vortex mass and electric charge are then considered, along with the role of the vortex fields in the spin-orbit interaction within the beam. Section III covers the dynamics of the electron vortex in external fields. Section IV discusses the various methods for the realization of electron vortex beams in the laboratory that have hitherto been considered, drawing comparison with the creation of optical vortex beams wherever such an analogy can be identified. Section V deals with the methods one can use to analyze the various properties associated with vortex beams. The interaction of electron vortex beams with matter is covered in Sec. VI. The prospects of using electron vortex beams to determine chirality and other magnetic information are discussed in terms of both theoretical and experimental considerations, with concluding remarks about the field given in Sec. VII.

II. QUANTUM MECHANICS OF ELECTRON VORTEX BEAMS

Freely propagating vortex states having the required $e^{il\phi}$ phase factor may be written as solutions to the Schrödinger, Klein-Gordon, and Dirac equations (Bliokh *et al.*, 2007; Bliokh, Dennis, and Nori, 2011; Schattschneider and Verbeeck, 2011; Bliokh and Nori, 2012a, 2012b; Karlovets, 2012; van Boxem, Verbeeck, and Partoens, 2013) yielding nonrelativistic, relativistic, and spinor electron vortex beams, respectively. The spatial distributions of these vortex solutions may take various forms in the relativistic, nonrelativistic, and paraxial limits and each state is characterized by the distinguishing feature of a vortex, namely, the node on the propagation axis. Such states have been mostly described either by the Bessel functions, prototypes of nondiffracting vortex beams (McGloin and Dholakia, 2005), or by the LG functions which are well known in optics (Allen *et al.*, 1992), with LG representing a beam with a well-defined waist at the focal plane. Since both the Bessel and Laguerre-Gaussian sets of functions form complete orthonormal basis sets, any beam, vortex or otherwise, may be described in terms of these vortex states. In the nonparaxial and relativistic limits of the Dirac equation, the spin of the electron also plays a role, and the particular distribution is modified by a spin-orbit interaction intrinsic to the beam (see Sec. II.D). Note that there is an interesting alternative approach describing electron vortices as a natural consequence of the skyrmion model of a fermion (Bandyopadhyay, Basu, and Chowdhury, 2014, 2016, 2017; Chowdhury, Basu, and Bandyopadhyay, 2015), but this will not be discussed any further in this review.

The remainder of this section introduces the specific properties of the electron vortex beam mainly in the nonrelativistic and paraxial limits, focusing on solutions to the Schrödinger equation. This will not only enable direct comparison with the commonly applied paraxial solutions in optics, a comparison facilitated by the functional equivalence between the Schrödinger and the scalar Helmholtz equations, but also illustrates the most important properties of electron vortex beams and serves as a basis for understanding more complex vortex beams.

A. Phase properties of vortex beams

The phase structure of a vortex wave is topologically different to that of a plane wave. In contrast to a plane wave, with phase fronts that are normal to the propagation direction, the phase front of the vortex wave describes a helix about the axis of propagation (Nye and Berry, 1974) such that the phase is dependent on the angular position about the axis. This topological structure was first described by Nye and Berry (1974) as screw-type dislocations in wave trains, in analogy with crystal defects. The topological charge l (also called the winding number) quantizes this winding such that there are l twisted wave fronts about the beams axis, or equivalently a phase change of $2\pi l$ during a full rotation about the axis as shown in Fig. 1. The phase factor of $e^{il\phi}$ that gives rise to this helical phase structure is a characteristic feature of orbital angular momentum (cf., the similar phase factor in the azimuthal components of the orbital angular momentum-containing hydrogenic wave functions). The functions characterizing a vortex beam propagating with a well-defined axis (taken along the z direction) have a general form which can be conveniently written in cylindrical coordinates $\mathbf{r}(\rho, \phi, z)$:

$$\psi_l(\mathbf{r}, t) = u(\rho, z)e^{il\phi}e^{ik_z z}e^{-i\omega t}, \tag{1}$$

with $u(\rho, z)$ a suitable mode function such as the Laguerre-Gaussian functions (Sec. II.B.1), which are characterized by the azimuthal index l and the radial index p, or the Bessel functions of the first kind (Sec. II.B.2), which are characterized by just the azimuthal index l. The helical phase structure of the vortex beam leads to the phase at the core of the beam as indeterminate since it is connected to all possible phases of the wave. This central phase singularity is not physically viable and is compensated by the requirement that all functions must vanish on axis (at the location of the singularity), giving the beam a cross-sectional distribution in the form of a ring, or concentric rings. This has led to the nickname of "doughnut" beams for a particular class of vortex beams—the Laguerre-Gaussian vortices with nonzero winding number $|l|$, but zero radial index ($p = 0$), each being a bright ring surrounding a central dark core. The requirement that all vortex functions must vanish on axis is, however, not sufficient to describe a vortex beam—there must be some topological difference between a region of the beam containing the vortex and a region that does not (Nye and Berry, 1974). For the present purposes, the topology of the vortex

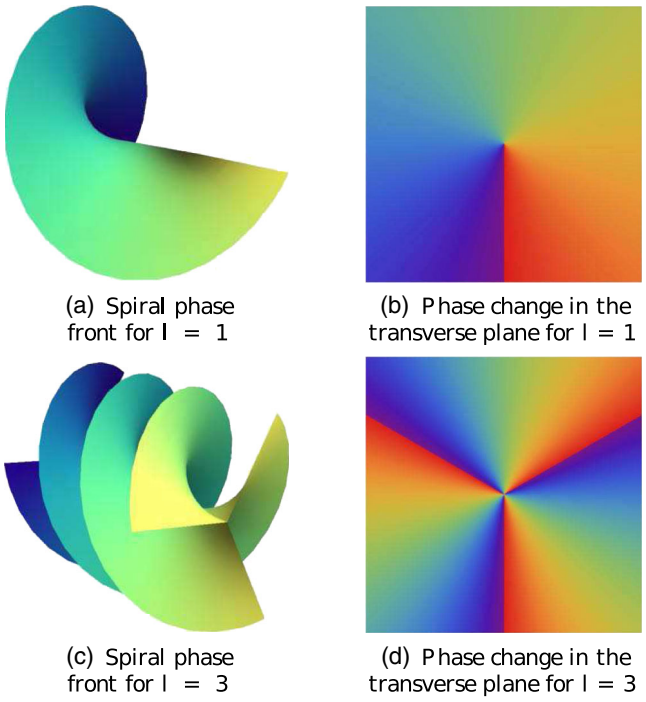

FIG. 1. The phase character of $l = 1$ and 3 vortex beams. (a) The single helix phase front of an $l = 1$ vortex around the beam axis. (b) The corresponding continuous phase ramp in one of the transverse planes perpendicular to the beam axis. The total phase change on one rotation is exactly 2π. For the $l = 3$ vortex there are three helical surfaces of constant phase, each moving around the axis as shown in (c). This leads to a total phase change on one rotation of exactly 6π. We used wrapped phase representation, with all phases mapped to values between 0 and 2π [represented between blue to red in the 2D phase maps in (b) and (d)], so there are three "artificial" phase jumps from 0 to 2π in the phase-wrap representation as shown in (d). In both cases, the only real phase discontinuity of significance is on the beam axis.

describes the connectedness of the phase fronts. The phase front of the vortex is topologically distinct from that of a plane wave, as one cannot be transformed into the other through continuous deformations. Similarly, the $l = 1$ phase front cannot be deformed into the $l = 2$ or any other l phase front, and this is the reason why the winding number l has also been termed the topological charge, characterizing the "strength" of the vortex. As pointed out earlier, the phase front of any vortex is characterized by the factor $e^{il\phi}$ leading to a phase singularity along the propagation axis. In order to appreciate the significance of the topological charge we assume that the function ψ given in Eq. (1) represents a wave function of a vortex beam state of a particle of mass m. It is easy to show that a closed loop integration of the probability current density

$$\mathbf{j}(\mathbf{r}) = \frac{\hbar}{2mi}\{\psi^*(\mathbf{r},t)\nabla\psi(\mathbf{r},t) - \psi(\mathbf{r},t)\nabla\psi^*(\mathbf{r},t)\}$$

along a path C encircling the axis gives a quantized value proportional to the topological charge of the beam (Bialynicki-Birula, Bialynicka-Birula, and Śliwa, 2000),

$$\oint_C \mathbf{j}(\mathbf{r})\cdot d\mathbf{s} = \frac{2\pi\hbar}{m}l, \tag{2}$$

where $d\mathbf{s}$ is a line displacement vector tangential to the path C.

For the vortex beam given in Eq. (1) we have the normalized probability current density

$$\mathbf{j}(\mathbf{r}) = \frac{\hbar}{m}\left(\frac{l}{\rho}\hat{\boldsymbol{\phi}} + k_z\hat{\mathbf{z}}\right). \tag{3}$$

Integrating this about a loop enclosing the z axis gives $(2\pi\hbar/m)l$, while any other closed path gives zero, showing the topological distinction between a region of space containing the vortex and one that does not. Thus, on circling the z axis an additional phase of $2\pi l$ is acquired.

B. Vortex beam solutions of the Schrödinger equation

The wave function $\psi(\mathbf{r},t)$ describing an electron vortex beam is a solution of the Schrödinger equation, namely,

$$\mathcal{H}\psi(\mathbf{r},t) = \mathcal{E}\psi(\mathbf{r},t), \tag{4}$$

where $\mathcal{E}$ is the energy eigenvalue. In free space, the Hamiltonian $\mathcal{H}$ is given by the kinetic energy of the electron beam only

$$\mathcal{H} = \frac{\mathbf{p}^2}{2m}, \tag{5}$$

where $\mathbf{p}$ is the linear momentum operator. Equation (4) can be rearranged to look like the Helmholtz equation for monochromatic light:

$$\nabla^2\psi(\mathbf{r},t) + k^2\psi(\mathbf{r},t) = 0, \tag{6}$$

where k is the magnitude of the wave vector of the electron beam and is given by

$$k^2 = \frac{2m\mathcal{E}}{\hbar^2}. \tag{7}$$

This equivalence is the basis for treating freely propagating electrons and light on the same footing, at least at the scalar field level. Indeed the fields of electron microscopy, ion beam physics, and accelerator physics started on this basis. The same is true for the electron vortex beam research.

In general, the vortex solution of the Schrödinger equation requires the complex wave functions to be identically zero to cope with the phase indeterminacy at the vortex core (Bialynicki-Birula, Bialynicka-Birula, and Śliwa, 2000). This means that both real and imaginary parts of the wave function should be zero separately. Each condition defines a surface and the vortex core can be considered as the intersection of the two surfaces, resulting in a line of vortex cores. In the following, we first consider two simple solutions in which the vortex core forms a straight line along the z axis. We then introduce a specific and a general solution, which is more useful in the context of the practical electron vortex beams which are usually generated under bandwidth-limited

conditions. In general, the vortex lines can be curved, closed, and knotted (O'Holleran *et al.*, 2008), but they can be regarded as a superposition of the simpler straight vortex lines introduced later.

1. Laguerre-Gaussian beams

Optical vortex beams are most commonly discussed in terms of Laguerre-Gaussian modes, as these are a good approximation to the vortex modes created from Hermite-Gaussian laser modes (Lax, Louisell, and McKnight, 1975; Padgett, 1996). The Laguerre-Gaussian vortex beam state arises as a solution of the paraxial approximation of the Helmholtz equation for light or Schrödinger equations for electrons in free space:

$$\left(\nabla_\perp^2 + 2ik_z\frac{\partial}{\partial z}\right)\psi = 0, \tag{8}$$

where ψ is a component of the vector field and the subscript $\perp$ in $\nabla_\perp$ indicates differentiation only with respect to in-plane (transverse) coordinates. This equation describes a component of the relevant field propagating in the z direction with an axial wave vector of magnitude k_z. The variations along the axis are considered so small that the second axial derivative may be neglected (Kogelnik and Li, 1966; Lax, Louisell, and McKnight, 1975). The solutions of Eq. (8) represent a vortex for which the magnitude of the transverse momentum $\hbar k_\perp$ is much smaller than the axial momentum $\hbar k_z$ (overall $k_\perp^2 + k_z^2 = k^2$). A suitable vortex solution to Eq. (8) is the Laguerre-Gaussian form, which has a Gaussian envelope modified radially by a Laguerre polynomial, with appropriate phase factors. We have, written in cylindrical polar coordinates $\mathbf{r} = (\rho, \phi, z)$,

$$\begin{aligned}\psi_{p,l}^{\mathrm{LG}}(\mathbf{r},\mathrm{t}) = {} & \frac{C_{lp}z_R}{\sqrt{z_R^2+z^2}}\left(\frac{\sqrt{2}\rho}{w(z)}\right)^l L_p^l\left(\frac{2\rho^2}{w^2(z)}\right) \\ & \times e^{ik_z z}e^{-i\omega t}e^{il\phi} \\ & \times e^{\{-[\rho^2/w^2(z)]+[ik_z\rho^2 z/2(z_R^2+z^2)]-i(2p+|l|+1)\tan^{-1}(z/z_R)\}},\end{aligned} \tag{9}$$

where $L_p^l(x)$ is the generalized Laguerre polynomial, with azimuthal index l, radial index $p \geq 0$, and normalization factor $C_{lp} = \sqrt{2^{|l|+1}p!/\pi(|l|+p)!}$. The z dependence of the Gaussian envelope is depicted in Fig. 2, with the characteristic parameters of width $w(z)$ and Rayleigh range z_R given by

$$w(z) = w_0\sqrt{1+\left(\frac{2z}{k_z w_0^2}\right)^2}, \tag{10}$$

$$z_R = \frac{k_z w_0^2}{2}, \tag{11}$$

where $w_0 = w(0)$ is the beam radius at focus. The radial profile of the beam varies with the indices p and l. The azimuthal index l is responsible for the beam orbital angular momentum $l\hbar$ per electron and may take any integer value,

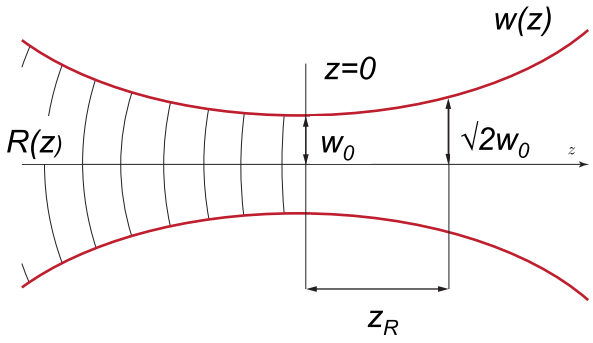

FIG. 2. Schematic representation of the Gaussian profile showing the characteristic parameters, namely, the width $w(z)$, with w_0 the width at the narrowest part of the beam. z_R is the Rayleigh range and $R(z)$ is the in-plane radius of curvature at axial position z

either positive or negative. The radial index $p \geq 0$ specifies the number of intensity maxima, i.e., the number of rings in the radial intensity distribution, such that the beam has $p+1$ maxima (for $l = 0$, the beam has a central spot, and p additional rings). The transverse distributions of the Laguerre-Gaussian beams are displayed in Fig. 3 for various sets of l and p. As can be seen, the modes with $|l| > 0$ have a central minimum, and Eq. (9) has the appropriate $e^{il\phi}$ phase

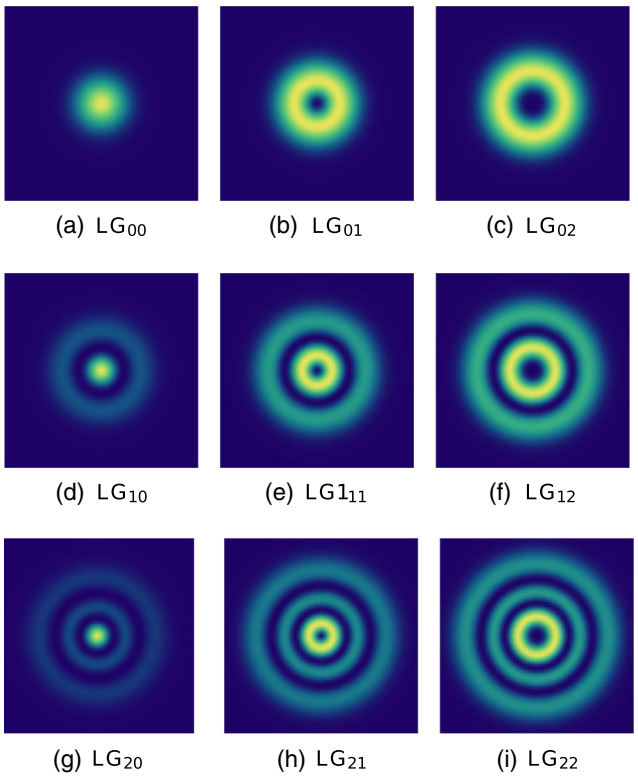

FIG. 3. Intensity distribution patterns for the $\mathrm{LG}_{\mathrm{pl}}$ modes, shown in the $z = 0$ plane. Intensity is given by $|\psi_{p,l}^{\mathrm{LG}}|^2$. The concentric ring structure of the orbital angular momentum carrying modes is clear, with $p+1$ rings. The color scale shows the intensity variation within individual modes (not the relative intensity variation across all modes). The Laguerre-Gaussian modes with $l < 0$ have the same intensity distributions as shown; however, the phase (not shown) has the opposite sign.

factor, indicating that the Laguerre-Gaussian modes are endowed with the required feature of phase vortices.

In addition to the phase factor relating to the orbital angular momentum, the Laguerre-Gaussian beam also has the following Gouy phase factor:

$$\exp\left[-i(2p+|l|+1)\arctan\left(\frac{z}{z_R}\right)\right] \tag{12}$$

which is associated with the focusing of the beam at the waist plane (Feng and Winful, 2001; Petersen *et al.*, 2014). As a result a convergent Gaussian beam experiences a phase change of $\pi/2$ as it passes through the focal plane from $-\infty$ to $+\infty$, whereas the phase shift of the Laguerre-Gaussian beam on focusing is given as

$$-(2p+|l|+1)\frac{\pi}{2}. \tag{13}$$

The Gouy phase shift arises due to the spatial confinement of the beam, leading to momentum components in the transverse direction that contribute to the dynamic phase of the beam (Feng and Winful, 2001; Petersen *et al.*, 2014). Near the focal plane, the rate of change of the transverse momentum of the Laguerre-Gaussian beam is larger than that of the fundamental Gaussian beam due to the more complex radial profile. The magnitude of the Gouy phase change thus depends on the radial and azimuthal mode indices.

2. Bessel beams

The Bessel-type electron vortex beam wave function takes the form

$$\psi_l^B(\mathbf{r},t) = N_l J_l(k_\perp \rho) e^{il\phi} e^{ik_z z} e^{-i\omega t}, \tag{14}$$

where $J_l(k_\perp\rho)$ is the Bessel function of the first kind, of order l, where, l is the topological charge, or winding number. The wave numbers k_z and $k_\perp$ are the axial and transverse wave vector components such that $|\mathbf{k}| = \sqrt{k_z^2 + k_\perp^2}$. N_l is a suitable normalization factor determined by the specific boundary conditions of the beam. Except for $l = 0$, all other Bessel functions satisfy $J_l(0) = 0$, so that they are suitable for describing a vortex beam. Their spatial distribution functions are functions of the radial coordinate ρ only, so that in contrast to Laguerre-Gaussian beams, freely propagating Bessel beams are nondiffractive (Durnin, Miceli, and Eberly, 1987), and the use of the full Helmholtz or Schrödinger equations coincides with the paraxial limit in this case. The Bessel beams are indeed the simplest type of vortex beams and so provide an ideal theoretical platform to determine the general characteristics of vortex beams.

The oscillatory nature of Bessel functions gives the Bessel beam a cross section of concentric rings, decreasing in brightness away from the axis. This concentric ring structure is shown in Fig. 4. However, unlike the Laguerre-Gaussian function, which decays exponentially with radial position, the Bessel function is infinite in extent, so that in principle the beam contains an infinite number of rings. Each ring of the Bessel beam carries the same power in the case of an optical vortex beam (Durnin, Miceli, and Eberly, 1987), while for electron vortex beams the relevant property is the current, which implies infinite power being carried by the beam, which is of course physically unrealistic. What is meant by a physical Bessel-type beam is a beam that has amplitude modulation similar to a Bessel function, over a finite radius, and whose core components behave nondiffractively (such that the central maximum or minimum persists with very little spreading) over a reasonable, but finite, propagation length (McGloin and Dholakia, 2005). These are achievable by several methods in optics including axicon lenses, annular apertures, and holograms (Durnin, Miceli, and Eberly, 1987; McGloin and Dholakia, 2005) and have also been generated in electron optics using kinoforms (Grillo, Gazzadi *et al.*, 2014). A kinoform is a wave front reconstruction device (Jordan *et al.*, 1970).

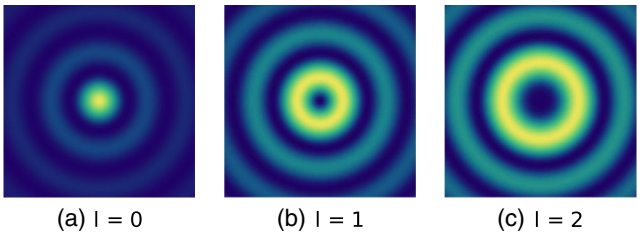

FIG. 4. The intensity $|\psi_l^B(\mathbf{r})|^2$ of a Bessel beam with (a) $l = 0$, (b) $l = 1$, and (c) $l = 2$. The Bessel modes with $l < 0$ have the same intensity distributions as shown; however, the phase (not shown) has the opposite sign.

In the momentum representation $\mathbf{k}'(k'_\perp, \phi', k'_z)$ the Bessel beam has the form

$$\tilde{\psi}_l(\mathbf{k}') = \frac{i^{-l}}{2\pi}\frac{e^{il\phi'}}{k_\perp}\delta(k_z - k'_z)\delta(k_\perp - k'_\perp), \tag{15}$$

which is interpreted as a superposition of plane waves of varying $k_\perp$ such that $k = \sqrt{k_\perp^2 + k_z^2}$ for each wave (see Fig. 5). For a given k_z the possible $k_\perp$ lie on a ring on the surface of constant k, so that there is a cone of plane waves of varying $\mathbf{k}$ that constitute the Bessel beam (McGloin and Dholakia, 2005; Bliokh, Dennis, and Nori, 2011), with the phase of each given by $e^{il\varphi}$. This is the principle by which axicon lenses produce the rings of a Bessel-type beam (Herman and Wiggins, 1991). The conical propagation leads to another interesting property of the Bessel beam, namely, that the original spatial distribution is reconstructed after propagation past an obstruction (MacDonald *et al.*, 1996; McGloin and Dholakia, 2005), as has been demonstrated for electron vortex Bessel beams (Grillo, Karimi *et al.*, 2014).

3. Bandwidth-limited vortex beams

In electron vortex beam research, the limited transverse spatial coherence of practical electron sources means that finite radius vortex modes defined using a circular aperture (or pupil) function are more appropriate in real situations. The simplest bandwidth-limited vortex beam is generated by the Fraunhofer diffraction of a plane wave by a spiral phase plate with the transmission function

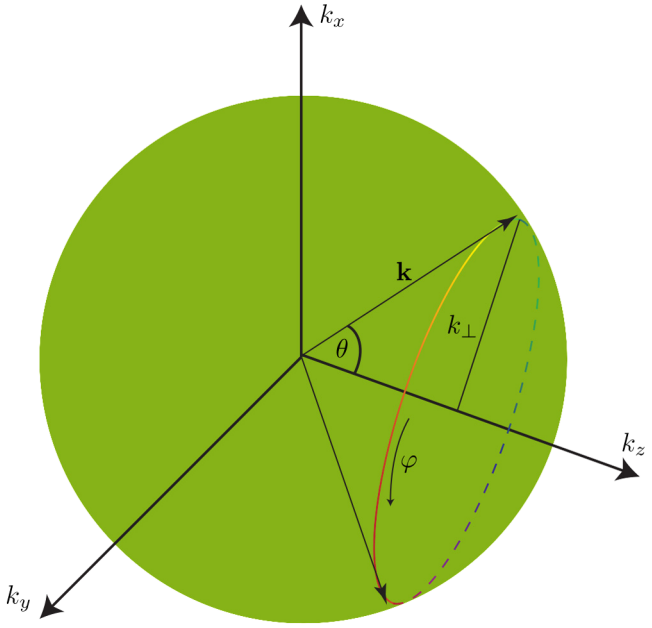

FIG. 5. The Fourier transform of the Bessel beam results in a set of waves of fixed k_z and varying k_x and k_y, such that $k_\perp = \sqrt{k_x^2 + k_y^2}$. The vortex Bessel beam illustrated here has a phase factor $e^{il\varphi}$, so that the phase changes by $2\pi l$ on rotation about the k_z axis. This is illustrated for $l = 1$. The relationship between k_z and $k_\perp$ fixes the cone angle θ.

$$\psi(\rho', \phi', z) = e^{il\phi'} e^{ik_z z} \tag{16}$$

through an aperture of finite radius $R_{\max}$. We used the convention for the momentum or Fourier space representation of the variables as in Eq. (15), since the truncation is in practice taking place in the aperture plane of a convergent electron lens as shown in Fig. 6.

The diffracted beam intensity is related to the Fourier transform of the transmitted wave, which can be written as (Kotlyar *et al.*, 2006, 2007; Lubk, Clark *et al.*, 2013)

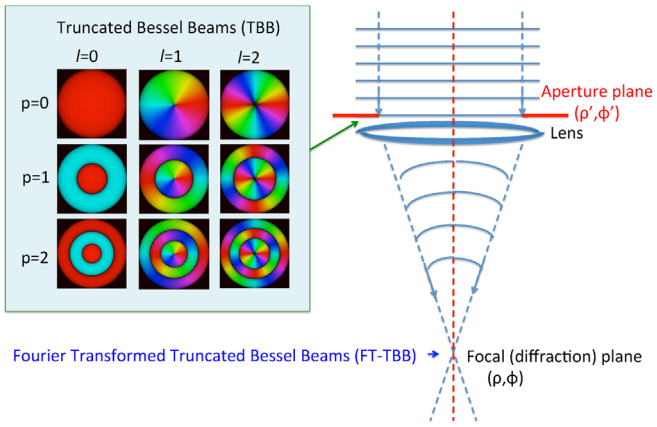

FIG. 6. The intensity and phase distribution of the transverse wave functions of FT-TBB at $z = 0$. From Thirunavukkarasu *et al.*, 2017 and are plotted for the same relative scale.

$$\tilde{\psi}(\rho, \phi, z) = e^{il\phi} \frac{2\pi i^l 2^{-l} \rho^l R_{\max}^{2+l}}{(2+l)\Gamma(1+l)} \times {}_1F_2\left(1 + \frac{l}{2}; 2 + \frac{l}{2}; 1 + l; -\frac{1}{4}\rho R_{\max}^2\right), \tag{17}$$

where ${}_pF_q(a; b; c; z)$ is the generalized hypergeometric function. This is a limiting case of hypergeometric-Gaussian beams (Karimi *et al.*, 2007) due to diffraction of apertured spiral phase masks by a Gaussian beam.

To represent the wave form of the arbitrary beam in similar bandwidth-limited situations, an orthonormal basis set characterized by orbital angular momentum was recently reported for vortex beams (Thirunavukkarasu *et al.*, 2017), including both the azimuthal and radial quantum numbers l and p, respectively. It is based on describing the normal modes of the transverse wave front confined to a finite radius at the pupil or aperture plane by an orthonormal set of truncated Bessel functions, much like the solutions of the allowed normal modes of surface vibrations on a drum surface:

$$\psi_{p,l}^{TBB}(\rho', \phi', z) = N_{p,l} e^{ik_z z} e^{il\phi'} J_l(k_\perp^{p_l} \rho') \quad \text{for } \rho' \le R_{\max}, \tag{18}$$

where the radial and azimuthal indices are p and l, respectively, following the convention used in the case of LG modes. We again used the cylindrical coordinates (ρ', ϕ', z) to describe the location in the aperture plane and $R_{\max}$ is the radius of the circular aperture. The magnitude of the transverse wave vector $k_\perp^{p_l}$ takes the discrete values $\lambda_{p,l}/R_{\max}$, with $\lambda_{p,l}$ the $(p+1)$th zero of the lth order Bessel function J_l, and $R_{\max}$ is the radius of the aperture. The truncated Bessel functions, whose amplitudes are for $\rho \ge R_{\max}$, together with the azimuthal phase factor form a complete two-dimensional basis set of the OAM modes at the aperture plane. The Fourier transform of these truncated Bessel beams forms a complete set of conjugated quantum bases which we termed Fourier transformed truncated Bessel beams (FT-TBB):

$$\psi_{p,l}^{\text{FT-TBB}}(k_\rho, \phi, z) = i^l \lambda_{p,l} J_l'(\lambda_{p,l}) e^{il\phi} \frac{J_l(k_\rho R_{\max})}{k_\perp^{p_l 2} - k_\rho^2}, \tag{19}$$

where k_q is the transverse wave vector of the diffracted beams. At the focal plane of a lens of power $1/f$, the corresponding radial displacement (ρ) is given by $f k_q / k_z$ $(\sim f k_q / k_0)$. The corresponding wave function in the focal plane coordinate (ρ, ϕ) becomes

$$\psi_{p,l}^{\text{FT-TBB}}(\rho, \phi, z) = i^l \lambda_{p,l} \frac{f}{k_0} J_l'(\lambda_{p,l}) e^{il\phi} \frac{J_l(k_\rho R_{\max})}{\rho_{p_l}^2 - \rho^2}, \tag{20}$$

where $\rho_{p,l}$ is the radius of the most prominent doughnut ring and is given by $\lambda_{p,l} f / R_{\max} k_0$.

The inset in Fig. 6 shows the schematic phase distribution of some of the low order basis wave functions of the truncated Bessel beams (TBB). Also shown is the conjugate relationship between the TBB and the FT-TBB.

The amplitude and phase of the first three p modes of the $l = 1$ FT-TBB subset are shown in Fig. 7, respectively. These results show that the higher order radial modes are

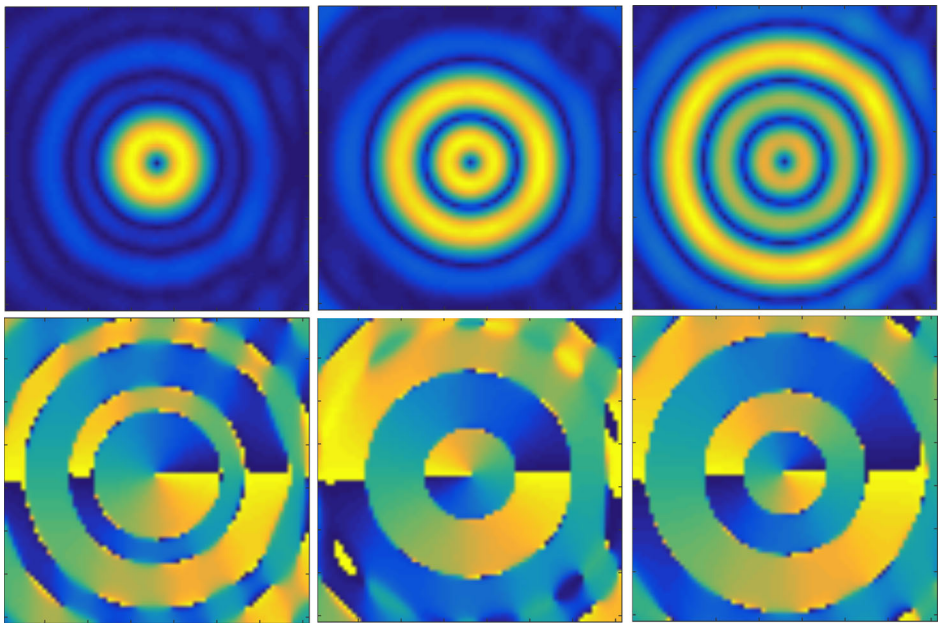

FIG. 7. Computer-simulated fine structure of the diffraction of truncated Bessel beams (FT-TBB): the first row is for intensity and the second row for the corresponding phase distribution. From left to right, for the FT-TBB vortex beams with $l = 1$ but with different radial modes ($p = 0$, 1, and 2). Adapted from Thirunavukkarasu *et al.*, 2017.

distinguished by $p + 1$ bright rings, reminiscent of the corresponding LG modes (Allen *et al.*, 1992). However, the similarity does not extend to the additional faint ring structures that can be seen in the amplitude distribution of the FT-TBB$_{1,3}$ mode. These small ringed structures are caused by the ringing effect of the sharply defined aperture. Another noticeable feature is that the largest amplitude occurs when k_ρ approaches $k_\perp^{p_l}$, in which case the wave function locally becomes a sinc function of the radial coordinate.

This can also be understood by regarding the original truncated beam as the product of the unobstructed Bessel beam and a top-hat mask function. The transverse structures of the vortex beam at the focal plane can be considered as the convolution of the Fourier transform of the Bessel function (whose transverse structure is a ring with a radius controlled by the radial size of the first dark zone in the truncated beam) and that of the top-hat mask (which is the well-known Airy pattern with side band ring structures). This is consistent with the mathematical form of the Fourier transform of the normal modes in the aperture plane. As p increases, the size of the first node ring shrinks and the Bessel ring at the focal plane increases in size. This explains the size changes seen in Fig. 7 (first row) for different values of p. The convolution of the Bessel rings with the Airy pattern functions results in sidebands, but they preserve the circular symmetry of the main Bessel peaks. The details of the experimental realization of the FT-TBB beams can be found in Thirunavukkarasu *et al.* (2017).

The FT-TBB set of beams is one of the bandwidth-limited vortex beams whose spatial frequency is determined by the aperture size. As this FT-TBB set of modes forms a complete orthonormal set, it can be used to describe any such bandwidth-limited vortex beam. For example, the simplest and most investigated bandwidth-limited electron vortex beam as shown in Eq. (17) can be expanded in terms of linear combinations of the FT-TBB set (Schattschneider and Verbeeck, 2011).

Both LG and Bessel beams are unbound solutions and are often discussed in theoretical developments because of their mathematical simplicity. On the other hand, bandwidth-limited beams are required for the precise description of electron vortex beams produced in real situations.

C. Mechanical and electromagnetic properties of the electron vortex beam

The global mechanical properties of electron vortex modes stem from the two basic properties of electrons, namely, that the finite electron mass leads to inertial position-dependent mass fluxes which are associated global inertial linear and angular momenta of the electron vortex beam while the finite electronic charge leads to position-dependent electromagnetic fields which are further sources of global linear and angular momenta. It is instructive to derive these global properties of the electron vortex with reference to the Bessel type, for mathematical convenience. Here we outline the treatment by Lloyd, Babiker, and Yuan (2013) who were first to show that the mechanical and electromagnetic properties of electron vortices emerge directly from the quantum mechanical wave function of the vortex mode. Concentrating on the Bessel-type vortex beam for which the wave function is given in Eq. (14) and writing $\omega = \mathcal{E}/\hbar$ we have

$$\psi(\mathbf{r}, t) = N_l J_l(k_\perp \rho) e^{ik_z z} e^{il\phi} e^{-i\mathcal{E}t/\hbar}. \tag{21}$$

The vortex beam is assumed to extend along the axis over a length D which is much larger than the beam width. The normalization factor N_l follows straightforwardly in the form

$$N_l = \left(\frac{k_\perp^2}{2\pi D \mathcal{I}_l^{(1)}}\right)^{1/2}, \tag{22}$$

where $\mathcal{I}_l^{(1)}$ is the first moment integral of the Bessel function defined by

$$\mathcal{I}_l^{(1)} = \int_0^\infty |J_l(x)|^2 x dx. \tag{23}$$

1. Inertial mechanical properties

The inertial mechanical properties are associated with the finite electron mass and these can now be derived as follows. The vortex wave function $\psi(\mathbf{r},t)$ gives rise to a local mass density $\rho_m(\mathbf{r},t)$ and a mass current density $\mathbf{j}_m(\mathbf{r},t)$ which are as follows:

$$\rho_m(\mathbf{r},t) = m\psi^*(\mathbf{r},t)\psi(\mathbf{r},t), \tag{24}$$

$$\mathbf{j}_m(\mathbf{r},t) = \frac{\hbar}{2i}\{\psi^*(\mathbf{r},t)\nabla\psi(\mathbf{r},t) - \psi(\mathbf{r},t)\nabla\psi^*(\mathbf{r},t)\}. \tag{25}$$

These emerge on substituting for $\psi(\mathbf{r},t)$ in the form

$$\rho_m(\mathbf{r},t) = m|N_l|^2|J_l(k_\perp\rho)|^2, \tag{26}$$

$$\mathbf{j}_m(\mathbf{r},t) = \hbar|N_l|^2\left(\frac{l}{\rho}\hat{\boldsymbol{\phi}} + k_z\hat{\mathbf{z}}\right)|J_l(k_\perp\rho)|^2, \tag{27}$$

where $\hat{\boldsymbol{\phi}}$ and $\hat{\mathbf{z}}$ form with $\hat{\boldsymbol{\rho}}$ the standard unit vector set for cylindrical coordinates. The unit vector $\hat{\mathbf{z}}$ is along the beam axis.

The evaluation of the global inertial linear momentum of the vortex follows from the realization that the (local) mass current density ($\mathbf{j}_m$) is the same as the (local) linear momentum density [$\mathcal{P}_m$, i.e., (local) linear momentum per unit volume]. The (global) inertial linear momentum vector of the Bessel electron vortex beam ($\mathbf{P}_m$) then follows by volume integration. We have

$$\mathbf{P}_m = \int \mathcal{P}_m(\mathbf{r},t)dV = \int \mathbf{j}_m(\mathbf{r},t)dV. \tag{28}$$

We find

$$\mathbf{P}_m = \hbar|N_l|^2 D \times \int_0^\infty \int_0^{2\pi} d\phi\left\{k_z\hat{\mathbf{z}} + \frac{l}{\rho}\hat{\boldsymbol{\phi}}\right\}|J_l(k_\perp\rho)|^2\rho d\rho. \tag{29}$$

It is easy to see that the azimuthal component in the integrand of $\mathbf{P}_m$ when integrated over the volume leads to a zero value because of a vanishing angular integral. By contrast the z component leads to a finite result. Direct integration of the z component in Eq. (29) gives

$$\mathbf{P}_m = 2\pi\hbar k_z D\mathcal{I}_l^{(1)}|N_l|^2\hat{\mathbf{z}} = \hbar k_z\hat{\mathbf{z}}, \tag{30}$$

where we made use of Eq. (22). The result $\mathbf{P}_m = \hbar k_z\hat{\mathbf{z}}$ is the inertial linear momentum of the Bessel electron vortex beam. Note that the inertial linear momentum is axial, involving only the axial component k_z of the wave vector. There are no in-plane components, neither as azimuthal nor radial, and there is no dependence on $k_\perp$. Note also that the azimuthal linear momentum density is nonzero, but as we have shown its volume integral vanishes. This is consistent with the cylindrical symmetry of the vortex beam.

The (local) inertial orbital angular momentum density ($\boldsymbol{\mathcal{L}}_m$) is defined as the moment of the (local) inertial linear momentum density. We have

$$\boldsymbol{\mathcal{L}}_m = \mathbf{r}\times\boldsymbol{\mathcal{P}}_m(\mathbf{r},t) = \hbar|N_l|^2(\rho\hat{\boldsymbol{\rho}} + z\hat{\mathbf{z}})\times\left\{\frac{l}{\rho}\hat{\boldsymbol{\phi}} + k_z\hat{\mathbf{z}}\right\}|J_l(k_\perp\rho)|^2. \tag{31}$$

Integration of this over the volume leads us to the (global) inertial orbital angular momentum vector ($\mathbf{L}_m$). We find

$$\mathbf{L}_m = \int \boldsymbol{\mathcal{L}}_m dV = \hbar|N_l|^2\int_{-D/2}^{D/2}\int_0^{2\pi}\int_0^\infty\left\{l\hat{\mathbf{z}} - \rho k_z\hat{\boldsymbol{\phi}} - \frac{l}{\rho}z\hat{\boldsymbol{\rho}}\right\} \times |J_l(k_\perp\rho)|^2\rho d\rho d\phi dz. \tag{32}$$

It is easy to verify that the angular and radial integrals lead to vanishing results and only the axial component survives. Using Eq. (22) the inertial angular momentum can be written in the form

$$\mathbf{L}_m = 2\pi l\hbar D\mathcal{I}_l^{(1)}|N_l|^2\hat{\mathbf{z}} = \hbar l\hat{\mathbf{z}}. \tag{33}$$

Equation (33) shows that, in general, the electron vortex beam carries only an axial inertial orbital angular momentum equal to $\hbar l$ and that, as is the case with the inertial linear momentum of the vortex, there are no transverse components. The components of the inertial angular momentum L_x and L_y are both zero as well as the inertial linear momentum components P_x and P_y. It turns out that this feature is not a preserve of electron vortex beams alone and holds for all pure vortex beams including the Bessel- and Laguerre-Gaussian-optical vortex beams.

2. Electromagnetic mechanical properties

We have so far concentrated on the inertial mechanical properties of the electron vortex beam, i.e., those due to the finite electron mass and such a theory applies to any electrically neutral particle vortex beam. However, an electron vortex beam also carries electric and magnetic fields $\mathbf{E}(\mathbf{r})$ and $\mathbf{B}(\mathbf{r})$ by virtue of the finite electric charge and magnetic moment. These fields have been evaluated by Lloyd *et al.* (2012) for a Bessel electron vortex beam generated under a condition that would be found in an electron microscope. The outlines are as follows.

Direct use of Maxwell's equations with the charge and current distributions of the electron vortex beam considered as

sources enables the evaluation of the specific electric and magnetic fields of the electron vortex beam. The Bessel electron vortex beam defined in Eq. (14) possesses cylindrically symmetric charge and current density distributions, each varying only as a function of the radial coordinate ρ, so that the electric and magnetic fields also have such a cylindrical symmetry. Respectively, the charge and current densities for the electron Bessel beam are found to be

$$\rho_e(\rho) = -e|N_l|^2 J_l^2(k_\perp \rho), \tag{34}$$

$$\mathbf{j}_e(\rho) = -\frac{e\hbar|N_l|^2}{m_e} J_l^2(k_\perp \rho)\left(\frac{l}{\rho}\hat{\boldsymbol{\phi}} + k_z \hat{\mathbf{z}}\right). \tag{35}$$

As with a linear charge and current source, the electron vortex beam possesses an electric field in the radial direction and a magnetic field in the azimuthal direction. In addition, due to the helical (solenoidlike) nature of the charged current density distribution, the Bessel vortex beam is characterized by an axial magnetic field component (Lloyd *et al.*, 2012). The electric field for the Bessel beam of the order of l is found to be

$$\mathbf{E}(\rho) = -\hat{\boldsymbol{\rho}}\frac{e|N_l|^2}{2\varepsilon_0} \times \rho[J_l^2(k_\perp\rho) - J_{l-1}(k_\perp\rho)J_{l+1}(k_\perp\rho)]. \tag{36}$$

This is valid for any l, including the nonvortex Bessel beam of $l = 0$. Similarly, the azimuthal component of the magnetic field of the same electron vortex beam is found to take the form

$$B_\phi(\rho) = e\mu_0\hbar\frac{k_z|N_l|^2}{2m_e} \times \rho[J_l^2(k_\perp\rho) - J_{l-1}(k_\perp\rho)J_{l+1}(k_\perp\rho)]. \tag{37}$$

Finally, the axial component of the magnetic field is given by

$$B_z(\rho) = e\mu_0\hbar\frac{|N_l|^2}{2m_e}\left(1 - \frac{4^{-l}\rho^{2l}{}_2F_3[\{l, l+1/2\}; \{l+1, l+1, 2l+1\}; -\rho^2]}{l^2[\Gamma(l)]^2}\right), \tag{38}$$

where ${}_pF_q[\{a_1 \cdots a_p\}; \{b_1 \cdots b_q\}; z]$ is the generalized hypergeometric function, and $\Gamma(x)$ is the gamma function. This general form reduces to a series of products of Bessel functions for particular values of l (Abramowitz and Stegun, 1972). Equations (36)–(38) are valid for the Bessel beam of infinite radial extent. In order to estimate the field strengths for vortices such as would typically be generated in an electron microscope, the wave function Eq. (14) may be truncated after a finite number of rings, i.e.,

$$\psi_l^t(\mathbf{r}) = \psi_l(\mathbf{r})\Theta(\rho - \rho_{l,n}), \tag{39}$$

where $\Theta(x)$ is the Heaviside step function, and $\rho_{l,n} = \alpha_{ln}/k_\perp$ is the radius corresponding to the nth zero of the Bessel function of the order of l, such that $J_l(\alpha_{ln}) = 0$. This wave function may then be applied to generate the charge and current densities of the truncated beam $(\rho_e)_l^t$ and $\mathbf{j}_l^t$, which are the sources for the electric and magnetic fields associated with the truncated vortex beam. We now consider a typical electron vortex beam created in a typical electron microscope. We choose a truncated Bessel beam with a single ring and the following parameters, which are typical for contemporary electron microscopes:

$$\begin{aligned} \text{beam energy:}\ & \mathcal{E} = 200\ \text{keV}, \\ \text{beam current:}\ & I = 1\ \text{nA}, \\ \text{axial wave vector:}\ & k_z = 2.291\,04 \times 10^{12}\ \text{m}^{-1}, \\ \text{radial wave vector:}\ & k_\perp = 2.291\,04 \times 10^{10}\ \text{m}^{-1}. \end{aligned}$$

The normalization factor N_l can be expressed in terms of the beam current I, which is a measurable quantity. We have

$$N_l^2 = \frac{Ik_\perp^2 m}{2\pi e\hbar k_z \int_0^{\alpha_{1l}} J_l^2(x)x\,dx}. \tag{40}$$

Figures 8 and 9 show the spatial distributions of the field components for the truncated Bessel vortex beams having $l = 1$ and 10. The field strengths are seen to be rather small for the parameters chosen. However, the field strengths scale linearly with the electric current (I), so that, in principle, electron vortices with larger field strengths could be produced experimentally. The z component is particularly interesting as it arises due to the vortex nature of the beam and is highly localized in a region of the order of an Å. Note that although the field strengths are particularly small, their gradients are rather large within the core region and the axial magnetic field gradient is of the order of hundreds of Tm^{-1}. This suggests that the electron vortex can impart a large force on a magnetic particle. Thus the electron vortex beam could potentially find applications in investigation of quantum mechanical phase effects due to localized magnetic systems and has implications for the possibility of observing the Aharonov-Bohm effect (Aharonov and Bohm, 1959) at small scales.

In general the vortex electric field is radial and is a function of the radial coordinate ρ only. It can be written succinctly as

$$\mathbf{E}(\rho) = \hat{\rho}E_\rho(\rho), \tag{41}$$

while the vortex magnetic field has two orthogonal components, one axial and another azimuthal

$$\mathbf{B}(\rho) = \hat{\mathbf{z}}B_z(\rho) + \hat{\boldsymbol{\phi}}B_\phi(\rho). \tag{42}$$

The (local) electromagnetic linear momentum density emerges straightforwardly as

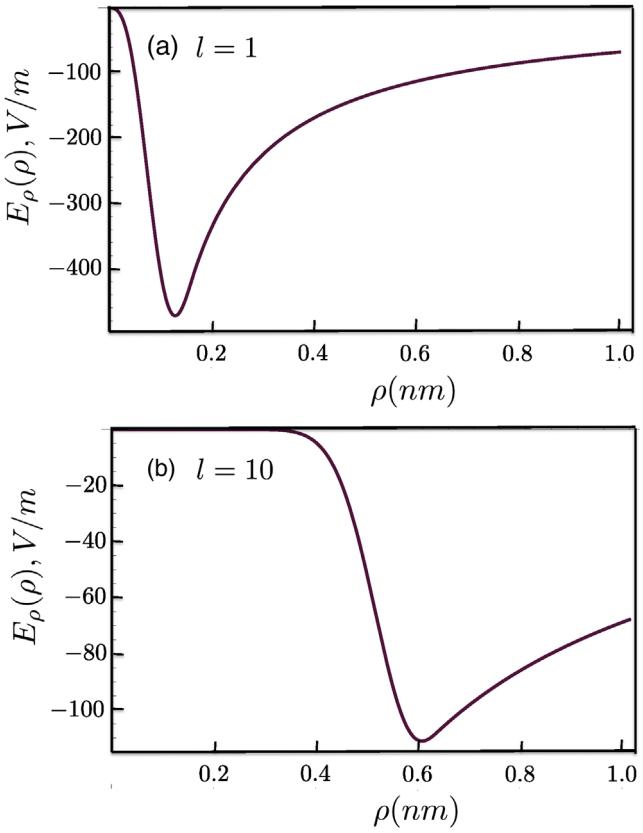

FIG. 8. The electric fields of the Bessel beams of finite radial extent, for (a) $l = 1$ and (b) $l = 10$, respectively. Adapted from Lloyd *et al.*, 2012.

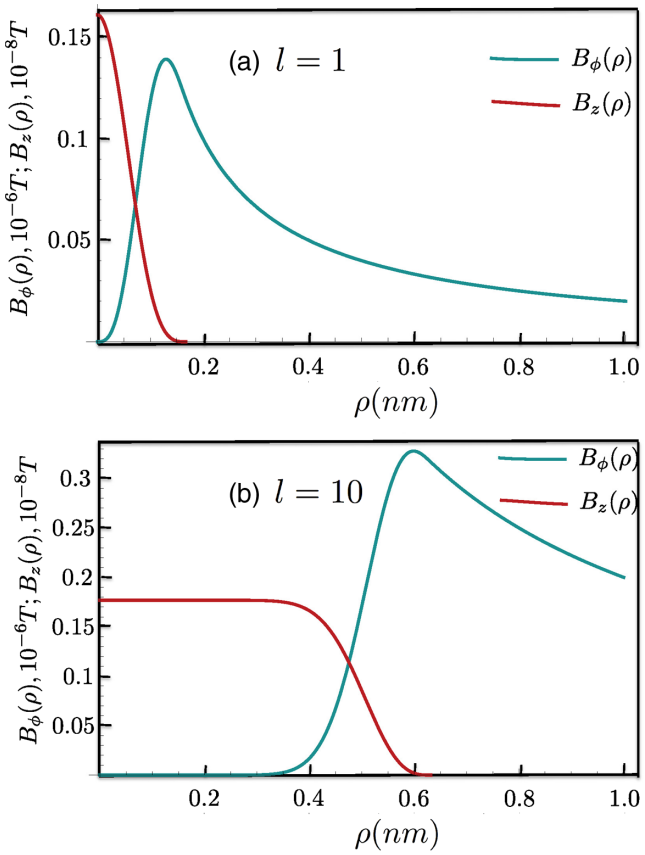

FIG. 9. The magnetic fields of the Bessel beam of finite radial extent, for (a) $l = 1$ and (b) 10, respectively. Note that the z components of the magnetic fields are 2 orders of magnitude smaller than the ϕ component. We assumed that the vortex beam is sufficiently long, as for a current carrying solenoid, allowing us to ignore beam ending effects. Adapted from Lloyd *et al.*, 2012.

$$\begin{aligned}\mathcal{P}_{\text{em}} &= \epsilon_0 \mathbf{E} \times \mathbf{B} \\ &= \epsilon_0 \{\hat{\mathbf{z}} E_\rho B_\phi - \hat{\boldsymbol{\phi}} E_\rho B_z\}, \end{aligned} \tag{43}$$

and the corresponding (global) electromagnetic linear momentum of the vortex beam follows by volume integration. Evaluating the integral over z yields

$$\mathbf{P}_{\text{em}} = \epsilon_0 D \int_0^\infty \rho d\rho \int_0^{2\pi} d\phi \{\hat{\mathbf{z}} E_\rho B_\phi - \hat{\boldsymbol{\phi}} E_\rho B_z\}. \tag{44}$$

Since the fields are functions only of ρ (Lloyd *et al.*, 2012), once again we note that the ϕ component gives a vanishing integral and we are left only with the axial component. We have

$$\mathbf{P}_{\text{em}} = \hat{\mathbf{z}} 2\pi\epsilon_0 D \int_0^\infty E_\rho B_\phi \rho d\rho. \tag{45}$$

The radial integration can be done numerically using expressions for the fields as functions of ρ.

Next we evaluate the electromagnetic angular momentum contributions as the integrals of the moment of the electromagnetic linear momentum density. We have

$$\begin{aligned}\mathbf{L}_{\text{em}} &= \int dV \mathbf{r} \times \mathcal{P}_{\text{em}} \\ &= \epsilon_0 \int dV \{\hat{\boldsymbol{\rho}} z E_\rho B_z - \hat{\boldsymbol{\phi}} \rho E_\rho B_\phi - \hat{\mathbf{z}} \rho E_\rho B_z\}, \end{aligned} \tag{46}$$

and it is easy to verify that we have a vanishing ϕ integral. The integral of the ρ component also vanishes and only an axial component remains. We then have

$$\mathbf{L}_{\text{em}} = -\hat{\mathbf{z}} 2\pi\epsilon_0 D \int_0^\infty E_\rho B_z \rho^2 d\rho. \tag{47}$$

Equations (45) and (47) are two further contributions to the mechanical properties of the electron vortex beam due to the vortex electromagnetic nature to be added to Eqs. (30) and (33) arising from the inertial properties.

Lloyd, Babiker, and Yuan (2013) considered orders of magnitude that could arise in a feasible experimental arrangement assuming electron vortices created inside a 1 nA electron microscope of energy 200 keV and transverse wave vector component $k_\perp = 0.01 k_z$. Estimates for the electromagnetic linear and orbital angular momenta in this scenario are found to be as follows:

$$P_{\mathrm{em}} \approx 10^{-34}\ \mathrm{kg\,m\,s^{-1}}, \tag{48}$$

$$L_{\mathrm{em}} \approx 10^{-48}\ \mathrm{J\,s}. \tag{49}$$

These are both extremely small compared to the inertial counterparts. The ratios are as follows:

$$\frac{P_{\mathrm{em}}}{P_{\mathrm{m}}} \approx 10^{-12}, \tag{50}$$

$$\frac{L_{\mathrm{em}}}{L_{\mathrm{m}}} \approx 10^{-14}, \tag{51}$$

so for practical purposes the electromagnetic linear and orbital angular momenta in such an electron microscope vortex beam are very small. However, in other contexts the electromagnetic contributions could be non-negligible as, for example, when the vortex beam is created in a linear accelerator.

Lloyd, Babiker, and Yuan (2013) also speculated on the orders of magnitude when electron vortex beams are used to rotate nanoparticles. They focused on the effects of the vortex beam on a nanoparticle in the form of a small cylinder of radius R and length $d = R$ whose axis is assumed to coincide with that of the vortex beam. A laser beam acts to first levitate the nanoparticle against gravity as well as the axial force of the vortex beam so that we have only rotational dynamics. For orientation as to orders of magnitude we assume that a minimum angular momentum of $\hbar$ is transferred to the nanoparticle. We can estimate a value for the angular frequency of a nanoparticle of fused silica of mass density of approximately $2.2 \times 10^3\ \mathrm{kg\,m^{-3}}$ and radius of 10^{-8} m and we find using $\hbar = I\Omega$ is

$$\Omega \approx 87.6\ \mathrm{Hz}, \tag{52}$$

where I is the moment of inertia of the particle about its axis. This is much higher than the angular frequency reported by Gnanavel, Yuan, and Babiker (2012) and Verbeeck, Tian, and Tendeloo (2013) for a gold nanoparticle on a support. The experiments seem to indicate that the rotation is damped due to friction between the nanoparticle and the support. The setup described by Lloyd, Babiker, and Yuan (2013) in which the nanoparticle is optically levitated would eliminate the effects of friction due to a support. Nanoparticles of fused silica would be easier to rotate as a controlled optical levitation of a metallic nanoparticle would be more difficult to achieve.

D. Intrinsic spin-orbit interaction

The spin-orbit interaction (SOI) arising in the nonrelativistic limit is well understood for electrons with orbital angular momentum bound within atomic orbitals; a similar phenomenon can be described for a vortex propagating in a radially inhomogeneous, but axially invariant field (Leary, Reeb, and Raymer, 2008; Leary, Raymer, and van Enk, 2009; Lloyd *et al.*, 2012). The source of this coupling is well known in the case of an external field; however, in the case of relativistic electron vortices, an intrinsic spin-orbit interaction is also shown to arise (Bliokh, Dennis, and Nori, 2011). The origin of the interaction is different in the two cases (the extrinsic, nonrelativistic coupling compared to the intrinsic coupling within the relativistic beams) however, the coupling mechanisms are similar and may be viewed as the electron traveling in an effective magnetic field, or alternatively as a manifestation of geometric phase (Leary, Reeb, and Raymer, 2008; Bliokh, Dennis, and Nori, 2011). The geometrical origins of the spin-orbit coupling have also been invoked to explain the origin of spin-orbit interaction in optical vortices, which of course are unaffected by a magnetic field (Allen, Lembessis, and Babiker, 1996; Bérard and Mohrbach, 2006; Bliokh, 2006; Leary, Raymer, and van Enk, 2009). In this section the effects and basis of the spin-orbit interaction in electron vortex beams are discussed.

In the relativistic and nonparaxial limits, the electron vortex beam exhibits an intrinsic spin-orbit interaction (Bliokh, Dennis, and Nori, 2011), in which the orbital angular momentum depends upon the spin polarization of the beam. Setting $c = 1$, the relativistic and nonparaxial electron vortex eigenstates are found to be (Bliokh, Dennis, and Nori, 2011)

$$\begin{aligned}\Psi_l = \frac{e^{ik_z z - i\omega t}}{\sqrt{2}} \Bigg[& \begin{pmatrix} \sqrt{1+\frac{m}{E}}\mathbf{w} \\ \kappa\sigma_z \cos\theta \mathbf{w} \end{pmatrix} e^{il\phi} J_l(k_\perp \rho) \\ & + i \begin{pmatrix} 0 \\ 0 \\ -\beta\kappa \sin\theta \\ 0 \end{pmatrix} e^{i(l-1)\phi} J_{l-1}(k_\perp \rho) \\ & + i \begin{pmatrix} 0 \\ 0 \\ 0 \\ \alpha\kappa \sin\theta \end{pmatrix} e^{i(l+1)\phi} J_{l+1}(k_\perp \rho) \Bigg], \end{aligned} \tag{53}$$

where $\mathbf{w}$, the two component spinor characterizing the electron polarization in the rest frame with $\mathcal{E} = m$, is given by

$$\mathbf{w} = \begin{pmatrix} \alpha \\ \beta \end{pmatrix}, \tag{54}$$

with α and β the projections of the spin polarization state in the basic eigenstates of S_z in the electron rest frame and $|\alpha|^2 + |\beta|^2 = 1$. $\kappa = \sqrt{1 - m/\mathcal{E}}$ and the angle θ describes the angle of the cone of Bessel plane waves, as shown in Fig. 5.

It can be seen that two "extra" modes arise in the relativistic electron vortex solutions, making the relativistic electron vortex a mixed state of l and $l \pm 1$ Bessel modes for spin $s = \pm 1/2$. These modes represent contributions of the small components of the Dirac spinor and vanish in both the nonrelativistic and paraxial limits. In the nonrelativistic limit $\kappa \to 0$, and in the paraxial limit we have $\sin\theta \to 0$ so that the pure l mode is recovered. Such solutions demonstrate that spin and orbital angular momentum are not always separately well defined except within the paraxial limit, with the relativistic electron vortex solutions showing similarities to the nonparaxial optical vortex solutions which also demonstrate an intrinsic spin-orbit interaction (Barnett and Allen, 1994;

Jáuregui, 2004; Bliokh *et al.*, 2010). Such an SOI is described as intrinsic as it does not require the influence of an external field or propagation medium; the nonparaxial or relativistic solutions are eigenmodes of the total angular momentum operator, but not separately of the spin and orbital angular momentum operators (Barnett and Allen, 1994; Bliokh *et al.*, 2010; Bliokh, Dennis, and Nori, 2011).

The origin of the intrinsic spin-orbit interaction is geometric in nature, arising from the momentum dependence of the modified spin and orbital angular momentum operators required to maintain the invariance of the total orbital angular momentum $\mathbf{J}$. This leads to a Berry gauge field $\mathbf{k}\times\mathbf{S}/k^2$, with corresponding curvature $\mathbf{k}/k^3$ having a monopole structure (Bliokh *et al.*, 2010; Bliokh, Dennis, and Nori, 2011). This monopole curvature leads to the accumulation of the Berry phase about the momentum spectrum of the Bessel beam (see Fig. 5), shifting the relative phase of the plane waves and modifying the orbital angular momentum of the beam. The solid angle of the curvature field subtended by the Bessel beam spectrum determines the magnitude of the coupling; a larger range of $k_\perp$, i.e., a larger cone opening angle θ, increases the Berry phase shift across the spectrum. Thus, in the paraxial approximation the spin-orbit interaction disappears, and spin and orbital angular momentum are fully separable. The geometrical arguments discussed here are also applicable to the extrinsic spin-orbit interactions, with the gauge and curvature in such cases originating from a gross orbital trajectory of the beam, such as in the photonic spin and orbital Hall effects (Bliokh, 2006; Bliokh *et al.*, 2008) and the motion of electrons in an inhomogeneous effective magnetic field (Bérard and Mohrbach, 2006; Leary, Reeb, and Raymer, 2008; Karimi *et al.*, 2012) or the propagation of photons in an inhomogeneous medium (Bérard and Mohrbach, 2006; Leary, Raymer, and van Enk, 2009).

Bliokh and Nori (2012b) extended the treatment of the electron vortex to polychromatic beams and showed that such a beam can carry intrinsic OAM at an arbitrary angle to the mean momentum of the beam.

III. DYNAMICS OF THE ELECTRON VORTEX IN EXTERNAL FIELD

Electrons subject to an external magnetic field obey a Schrödinger equation of the form

$$\mathcal{H}\psi=\frac{(\mathbf{p}-e\mathbf{A})^2}{2m}\psi, \tag{55}$$

where $\mathbf{p}^{\mathrm{kin}}=\mathbf{p}-e\mathbf{A}$ is the kinetic linear momentum operator with $\mathbf{A}$ the magnetic vector potential. For example, for a magnetic field $\mathbf{B}$ in the axial z direction, the magnetic vector potential is azimuthal in the direction

$$\mathbf{A}=\frac{B\rho}{2}\hat{\boldsymbol{\phi}}. \tag{56}$$

Solutions of the Schrödinger equation in the presence of several different field configurations have been investigated (Bliokh *et al.*, 2012; Gallatin and McMorran, 2012; Greenshields, Stamps, and Franke-Arnold, 2012; van Boxem, Verbeeck, and Partoens, 2013; Greenshields *et al.*, 2014; Velasco-Martínez *et al.*, 2016; Schattschneider, Grillo, and Aubry, 2017). The Landau configuration involves a constant magnetic field in a fixed direction (Landau and Lifshitz, 1977; Bliokh *et al.*, 2012; Gallatin and McMorran, 2012; Greenshields, Stamps, and Franke-Arnold, 2012), while the Aharanov-Bohm configuration can involve a single line of flux (Bliokh *et al.*, 2012). The vortex propagation direction may be transverse (Gallatin and McMorran, 2012), parallel (Bliokh *et al.*, 2012; Greenshields, Stamps, and Franke-Arnold, 2012) to the direction of the field, or in an arbitrary orientation (Greenshields *et al.*, 2014), and the interaction between the magnetic moment with the external field leads to interesting dynamics, as we now explain.

A. Parallel propagation

For the case when the electron vortex beam is propagating in the same direction as the magnetic field ($\mathbf{B}=B_z\hat{\mathbf{z}}$) the nonrelativistic Hamiltonian of the system takes the form (Greenshields, Stamps, and Franke-Arnold, 2012)

$$\mathcal{H}=\frac{p_z^2}{2m}+\frac{p_\perp^2}{2m}+\frac{1}{2}m\omega_L^2\rho^2+\omega_L(L_z\hat{\mathbf{z}}+g_s\mathbf{S}), \tag{57}$$

where L_z is the axial component of the orbital angular momentum operator, $\mathbf{S}$ is the spin vector operator, g_s is the gyromagnetic ratio, and $\omega_L=eB_z/2m$ is the Larmor frequency. Here the subscripts z and $\perp$ stand for axial and transverse vector components, respectively.

In the Aharonov-Bohm configuration, with a single flux line, the solutions to Eq. (55) take the form of Bessel beams, with current density winding around the flux line (Bliokh *et al.*, 2012). Similarly, the coaxially propagating eigenstates of Eq. (55) for a vector potential as in Eq. (56) have the form of nondiffracting Laguerre-Gaussian modes, with a fixed "magnetic" width (w_B) and magnetic Rayleigh range (z_B) given by the strength of the field (Bliokh *et al.*, 2012; Greenshields, Stamps, and Franke-Arnold, 2012)

$$w_B=2\sqrt{\frac{\hbar}{|e\mathbf{B}|}},\qquad z_B=2\frac{\sqrt{2\mathcal{E}m}}{|e\mathbf{B}|}. \tag{58}$$

The presence of the field alters the probability current density (Bliokh *et al.*, 2012) $\mathbf{j}\to(1/m)\langle\psi|\hat{\mathbf{p}}-e\mathbf{A}|\psi\rangle$, so that the z component of the observable kinetic OAM may be written as

$$\langle L_z\rangle=\frac{m\int\rho j_\phi dV}{\langle\psi|\psi\rangle}. \tag{59}$$

The Bessel beam eigenstates of the single flux line take the form

$$\psi^{\mathrm{AB}}=NJ_{|l-\bar{\alpha}|}(k_\perp)e^{i(l\phi+k_zz)}, \tag{60}$$

which are still eigenstates of $\hat{L}_z$, with eigenvalue $\hbar l$, but the observable OAM is now different. Bliokh *et al.* (2012) introduced a parameter $\bar{\alpha}=e\varphi/2\pi\hbar$ where φ is the magnetic

flux. The expectation value of the observable kinetic OAM is then given by

$$\langle L_z \rangle = \hbar(l - \bar{\alpha}), \tag{61}$$

while the charge density distribution is also altered, so that Bessel beams with $l = \pm 1$ do not have symmetric charge distributions in the presence of an external field. This is due to a Zeeman interaction between the magnetic moment of the beam and the field. Here, due to the infinitesimal localization of the flux line along a node of the Bessel beam, there is no energy or phase shift within the beam.

If the vector potential $\mathbf{A}$ relates to a constant magnetic field $\mathbf{B}$, the beam then undergoes phase and energy shifts. In this case, the eigenfunctions of Eq. (55) take the form of nondiffracting Laguerre-Gaussian modes, being radially described by the Laguerre-Gaussian functions, but having no width variation (Bliokh *et al.*, 2012; Greenshields, Stamps, and Franke-Arnold, 2012):

$$\psi^L = N_{l,p} \frac{1}{w_B} \left(\frac{\sqrt{2}\rho}{w_B} \right)^{|l|} L_p^{|l|} \left(\frac{2\rho^2}{w_B^2} \right) \times e^{-\rho^2/w_B^2} e^{il\phi} e^{ik_{l,p} z} \tag{62}$$

with w_B given by Eq. (58), and the longitudinal (axial) momentum now depends on the OAM and radial quantum numbers. Since the beam propagates parallel to the field, there is no transverse deflection, and the gross trajectory is unchanged; however, the circulation within the vector potential alters the beam phase as well as the observable orbital angular momentum, depending on the relative direction of the circulation of the field and the electron vortex. The energy eigenvalues take the form

$$\begin{aligned} \mathcal{E} &= \frac{\hbar^2 k_z^2}{2m} - \hbar\omega_L l + \hbar|\omega_L|(2p + |l| + 1) \\ &= \frac{\hbar^2 k_z^2}{2m} + \hbar|\omega_L|(2n_L + 1), \end{aligned} \tag{63}$$

i.e., the dynamics is that of free motion with superposed quantized Landau levels of index n_L, such that

$$n_L = p + \frac{|l|}{2}[1 + \mathrm{sgn}(Bl)]. \tag{64}$$

The second term of Eq. (63) has the form of a Zeeman interaction between the field and the orbital angular momentum, while the third term has the same form as the Gouy phase term in the diffracting Laguerre-Gaussian beam, relating to the transverse confinement of the mode (Feng and Winful, 2001). The Landau levels described by Eq. (64) are due to the combined effects of the Zeeman and Gouy phase shifts (Bliokh *et al.*, 2012; Greenshields, Stamps, and Franke-Arnold, 2012), where the Zeeman energy shift may be written in terms of the observable orbital angular momentum

$$\mathcal{E} = \frac{\hbar^2 k_z^2}{2m} - \omega_L \langle L_z \rangle, \tag{65}$$

with $\langle L_z \rangle$ incorporating the Gouy phase shift

$$\begin{aligned} \langle L_z \rangle &= \hbar \left(l + \mathrm{sgn}(B) \langle \frac{2\rho^2}{w_B^2} \rangle \right) \\ &= \hbar[l + \mathrm{sgn}(B)(2p + |l| + 1)]. \end{aligned} \tag{66}$$

The Gouy and Zeeman energy shifts lead to additional phase accumulation on the propagation of the vortex mode, described by the phase factor of $e^{-i\Delta(z/z_B)}$, with

$$\Delta = [l + \mathrm{sgn}(B)(2p + |l| + 1)]. \tag{67}$$

Unlike the Bessel beam eigenfunctions of the single flux line, the charge density distributions of the Landau Laguerre-Gaussian beams are not affected by the external field. On the other hand, the current density is altered in a surprising way, as shown in Fig. 10. If the beam orbital angular momentum vector is parallel to the field direction then the current density flow is in the same direction as that of the free-space Laguerre-Gaussian mode, and the observable OAM is enhanced. For those modes with $l \leq 0$ the observable orbital angular momentum turns out to be independent of the orbital angular momentum of the mode and is always greater than zero (Bliokh *et al.*, 2012; Greenshields, Stamps, and Franke-Arnold, 2012), so that there is now circulation in the current density of those modes with $l = 0$. Additionally, the current density of the modes with $l < 0$ changes direction at the radius of maximum intensity, $\rho_m = w_B\sqrt{|l|/2}$, due to competition between the negative intrinsic vortex current, which dominates at $\rho < \rho_m$, and the positive circulation induced by the external potential (Bliokh *et al.*, 2012).

Greenshields *et al.* (2014) explored the conceptual issue of conservation of orbital angular momentum for an electron beam in a uniform collinear magnetic field. They showed that the electric field associated with an electron beam with an extended probability distribution, such as that discussed by Lloyd *et al.* (2012) for the electron Bessel beam, when coupled to the external magnetic field, contributes an angular momentum which precisely ensures the conservation of the canonical orbital angular momentum of the electron beam in a magnetic field.

B. Transverse propagation

Substituting Eq. (56) into Eq. (55) and choosing Laguerre-Gaussian solutions propagating perpendicular to the magnetic field reveals interesting dynamics relating to the orientation of the OAM vector projected onto the electron trajectory or the helicity of the beam (Gallatin and McMorran, 2012)

$$\Sigma = \mathbf{L} \cdot \mathbf{p}/|\mathbf{p}|. \tag{68}$$

In such a field, an electron wave packet with orbital angular momentum follows the gross circular trajectory expected from classical electrodynamics, orbiting around the z axis at the

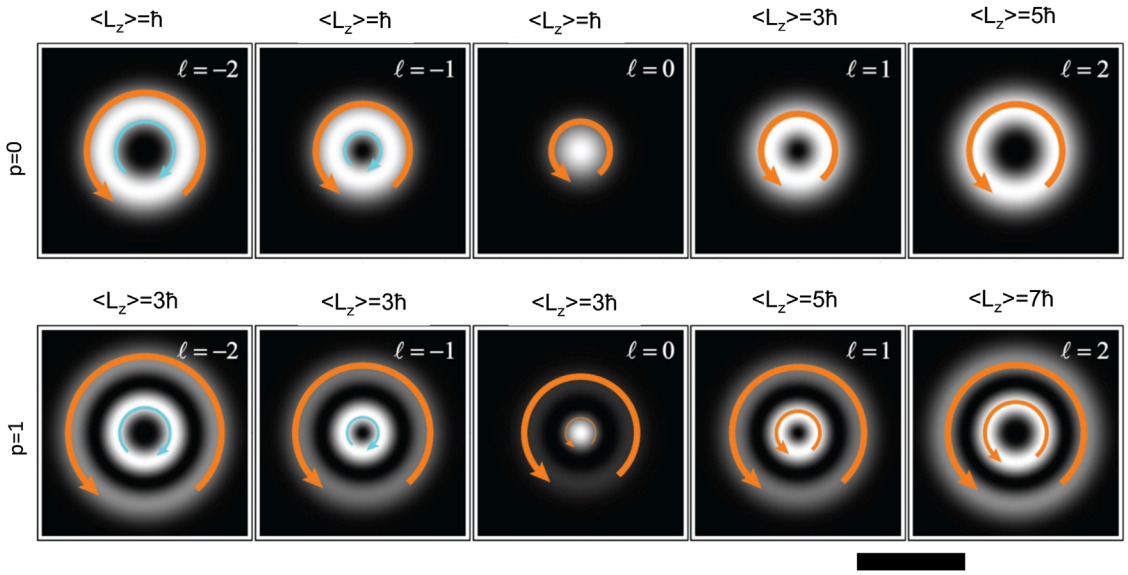

FIG. 10. The effect of the magnetic field on the circulating current of the nondiffracting Laguerre-Gaussian vortex modes for a magnetic field directed in the positive z direction, such that the vector potential has the same sense of circulation as the $l > 1$ vortex modes. The local character of the azimuthal current is indicated with arrows; it can be seen that the presence of the field induces circulation, even in the modes for which $l = 0$. For those modes with $l > 0$ the observable OAM (listed at the top of each figure) is increased from that of the bare mode, while those beams with $l \leq 0$ have a fixed observable OAM, determined by the field strength and the radial quantum number p. For those beams with $l < 0$ the azimuthal current changes direction at the point of maximum intensity. The top (bottom) panel is for the nondiffracting LG vortex modes with radial index $p = 0$ ($p = 1$). The scale bar length is $2w_B$. Adapted from Bliokh *et al.*, 2012.

cyclotron frequency $\omega_c = e|\mathbf{B}|/m$, with the expected quantized Landau levels. The spin helicity is conserved, however, the orbital angular momentum vector is found to precess with the Larmor frequency (equal to half the cyclotron frequency) $\omega_L = \omega_c/2$. Thus, on traversing a cyclotron orbit, the resulting orbital angular momentum vector now points in the direction opposite to the initial orientation, as shown in Fig. 11 (Gallatin and McMorran, 2012).

In addition to the rotation of the angular momentum vector, the physical extent of the wave packet is also found to be oscillatory when the propagating states are not exact eigenstates of the Hamiltonian equation (55) (Gallatin and McMorran, 2012; Greenshields, Stamps, and Franke-Arnold, 2012). Competition between diffractive effects arising from the propagation of the beam and focusing effects arising due to the confinement of the harmonic potential of the gross circular motion cause the length and width of the wave packet to oscillate, as can be seen in Fig. 11. These effects can be balanced to avoid such oscillations for wave packets having the characteristic width and the Rayleigh range determined by the strength of the field (Bliokh *et al.*, 2012; Gallatin and McMorran, 2012; Greenshields, Stamps, and Franke-Arnold, 2012):

The rotation of the orbital angular momentum helicity has important implications for electron vortex beams subject to transverse external fields. In particular, the transverse field components of the magnetic electron lenses may cause some reorientation of the orbital angular momentum vector as the beam spirals about the focal point. In particular, this effect will have consequences for the orientation of the beam orbital angular momentum when the sample is inside the lens field, as the change in orientation will not be reversed by the transverse fields of the opposite direction at the exit of the lens. On the other hand, these transverse components are small so that the dominant effect is expected to come from the vortex propagating coaxially with the vector potential.

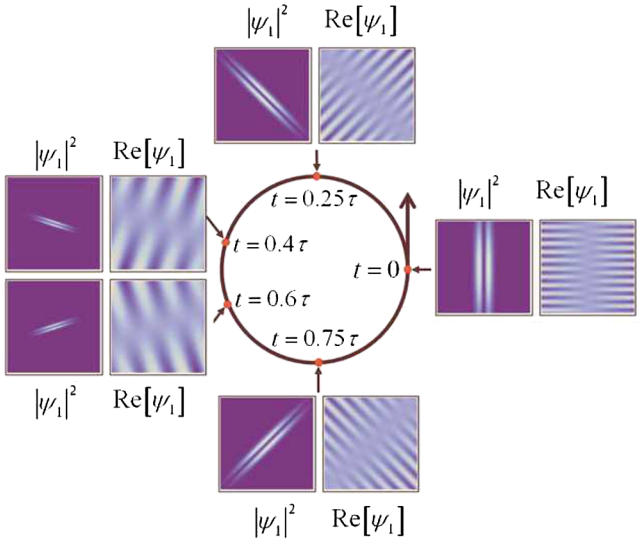

FIG. 11. Phase and intensity of the electron wave packet around the circular cyclotron trajectory. The wave packet can be seen to rotate at $\omega_L = \omega_c/2$, such that after one rotation the OAM vector points opposite to the original direction. The length and width of the wave packet also oscillates on rotation with the cyclotron frequency. Note that the scale of the plots of $\Re(\Psi_1)$ is roughly 5 orders of magnitude smaller than that of the $|\Psi_1|^2$ plots, so that the phase can be seen. From Gallatin and McMorran, 2012.

C. Rotational dynamics of vortex beams

By rotation dynamics, we mean the rotation of the transverse structure of the vortex beams as a function of the distance along the beam axis. As the beams are traveling waves, this can also be considered as the time evolution of the wave fronts. This is to be distinguished from the time-dependent changes in the transverse structure of the vortex beams at a given plane perpendicular to the beam axis. Such time-dependent changes are due to the coherent interference of electron waves with different energies, a process which is more challenging to investigate experimentally.

The phase change due to the influence of a constant magnetic field parallel to the beam axis may be observed in the form of rotations of asymmetric superposition of vortex states (Bliokh *et al.*, 2012; Greenshields, Stamps, and Franke-Arnold, 2012; Guzzinati *et al.*, 2013). This effect is very similar to the Faraday effect in optics causing rotation of spin polarization (Faraday, 1936; Nienhuis, Woerdman, and Kuščer, 1992). The orientation of linearly polarized optical beams rotates on propagation through a magnetic field, due to circular birefringence acting oppositely on the two spin components. This effect is not observed for optical orbital angular momentum, although a "mechanical Faraday effect" can be induced with the rotation of the medium through which the optical vortex superposition propagates (Franke-Arnold *et al.*, 2011). In electron beams such an orbital Faraday effect arises due to the Zeeman interaction between the field and the vortex magnetic moment, with apparent rotation due to the difference in the action of the field on the phase of the vortices counterpropagating and copropagating with the field (Bliokh *et al.*, 2012; Greenshields, Stamps, and Franke-Arnold, 2012). While observable in the electron microscope as an image rotation, it is quite distinct from the Lorentz force rotation that is well known in electron lens systems, with the Faraday rotation occurring even when there is no transverse motion of the beam axis with respect to the field.

Although the presence of the field causes a change in the phase, the rotation effect is observable only in the superposition of vortex states, due to the rotational symmetry of the single vortex mode. The superposition may have a zero or a nonzero net angular momentum, referred to as "balanced" or "unbalanced" superposition, respectively. In each case the rotation is independent of l, depending instead on the energy of the beam and the strength of the field. For the balanced superposition given by

$$\psi_b = \psi^{LG}_{l,p} + \psi^{LG}_{-l,p'} \tag{69}$$

the intensity distribution is that of a "petal" pattern with $2l$ lobes. As discussed, the change in phase on propagation is given as $\Delta z/z_B$. For superposition with fixed energy, the change in phase due to the presence of the field will necessarily be different for each vortex component, with the deviation from the kinetic phase factor given as $k = k_z \mp \mathrm{sgn}(B)\Delta/z_B$ for the $\pm l$ modes, respectively. The Gouy phase shift affects both components in the same way, whereas the Zeeman term leads to an l dependent phase of $\mp\,\mathrm{sgn}(B)lz/z_B$ for the $\pm l$ components. The phase difference between the two beams is observable as a rotation of the interference pattern by an angle (Bliokh *et al.*, 2012; Greenshields, Stamps, and Franke-Arnold, 2012)

$$\delta\phi_{l,-l} = \mathrm{sgn}(B)z/z_B. \tag{70}$$

This is independent of l, varying with the strength of the field and the energy of the beam through the characteristic length $z_B = \hbar k_z/m\omega_L$, so the characteristic frequency of the image rotation is the Larmor frequency.

Unbalanced superpositions of two or more vortex states are those for which the net angular momentum of the beam is nonzero. For example,

$$\psi_{ub} = \psi^{LG}_{0,p} + \psi^{LG}_{l,p'}. \tag{71}$$

Such a superposition has an intensity profile characterized by l off-axis vortices. In the case of the unbalanced superposition under the influence of the magnetic field, the existence of image rotations depends on the relative direction of the field and the beam propagation (Bliokh *et al.*, 2012). For the case when the beam is propagating along the field direction with a net positive OAM, i.e., $l\mathrm{sgn}(B) > 0$ the mode rotates on propagation, with the rotation angle given by

$$\delta\phi_{0,l} = 2\mathrm{sgn}(B)z/z_B, \tag{72}$$

which is, once again, independent of the value of the orbital angular momentum. On the other hand, for those situations having $l\mathrm{sgn}(B) < 0$ there is no image rotation at all, due to the additional Gouy phase terms canceling with the Zeeman phase acquired from the countercirculating field (Bliokh *et al.*, 2012).

D. Extrinsic spin-orbit interaction

The extrinsic SOI for electron vortex beams arises from the magnetic moment of the electron interacting with an effective magnetic field due to its motion within an inhomogeneous external potential. In order to facilitate SOI in the vortex beam, the external field must be radially inhomogeneous and axially invariant. In the nonrelativistic limit, the appropriate SOI may be derived by performing a Foldy-Wouthuysen transformation of the Dirac equation in the presence of fields (Bjorken and Drell, 1964). The Foldy-Wouthuysen transformation is a unitary transformation $U = e^{iS(t)}$, where $S(t)$ is an odd, self-adjoint operator. The Foldy-Wouthuysen transformation diagonalizes the Dirac Hamiltonian such that the particle and antiparticle solutions are not mixed, allowing the small components of the spinor wave functions to be systematically incorporated and their residual effects ultimately neglected (Foldy and Wouthuysen, 1950). The transformation takes the form

$$\mathcal{H}_{\mathrm{FW}} = e^{iS(t)}\left(\mathcal{H} - i\hbar\frac{\partial}{\partial t}\right)e^{-iS(t)}, \tag{73}$$

where H is the Dirac Hamiltonian. Applying the transformation and expanding in powers of $(mc^2)^{-1}$ yields a series expansion of the Dirac Hamiltonian for particle solutions. The

first few terms give the Pauli equation, the nonrelativistic Schrödinger equation with relativistic corrections, including the spin-orbit interaction term

$$\mathcal{H}_{\mathrm{FW}} = mc^2 + e\Phi + \frac{\mathbf{p}^2}{2m} - \frac{\mathbf{p}^4}{8m^3c^2} - \frac{e\hbar}{2m}\boldsymbol{\sigma}\cdot\mathbf{B} - \frac{e\hbar^2}{8m^2c^2}\nabla\cdot\mathbf{E} - \frac{e\hbar}{4m^2c^2}\boldsymbol{\sigma}\cdot(\mathbf{E}\times\mathbf{p} - \mathbf{p}\times\mathbf{E}), \tag{74}$$

where Φ is the Coulomb potential. The last term is relevant for the spin-orbit interaction; since we deal with the external electrostatic field we have $\nabla\times\mathbf{E}=0$. Additionally $\mathbf{E} = -\nabla\Phi$, so that the SOI may be written as (Leary, Reeb, and Raymer, 2008; Lloyd *et al.*, 2012)

$$\mathcal{H}_{\mathrm{SO}} = -\frac{e\hbar}{4m^2c^2}\left(\frac{1}{\rho}\frac{\partial\Phi}{\partial\rho}\right)\boldsymbol{\sigma}\cdot(\hat{\boldsymbol{\rho}}\times\mathbf{p}) = -\frac{e}{2m^2c^2}\left(\frac{1}{\rho}\frac{\partial\Phi}{\partial\rho}\right)\mathbf{S}\cdot\mathbf{L}. \tag{75}$$

It can be seen that, in contrast to the atomic SOI, only the z components of the spin and orbital angular momenta are relevant. This SOI Hamiltonian may now be applied perturbatively to the nonrelativistic vortex solutions to find the energy shift for the parallel or antiparallel spin and orbital angular momenta:

$$\delta_{(l,s)} = -\hbar^2 ls\langle\psi|\xi|\psi\rangle, \tag{76}$$

where

$$\xi = \frac{e}{2m^2c^2}\left(\frac{1}{\rho}\frac{\partial\Phi}{\partial\rho}\right). \tag{77}$$

For a positive Coulomb potential, with electric field pointing radially outward, the parallel (antiparallel) states shift upward (downward) in energy (Leary, Reeb, and Raymer, 2008; Lloyd *et al.*, 2012). This causes a splitting of the parallel and antiparallel states, which can be observed in the rotation of the superposition of parallel and antiparallel states having the same s but opposite l. The interference between such states gives rise to a characteristic "petal-like" interference pattern. If the parallel and antiparallel states have slightly different beam energies then the petal pattern will rotate as a function of time. On the other hand, if the energy is kept fixed then the two states will have different axial momenta, and the pattern will rotate as a function of position (Leary, Reeb, and Raymer, 2008). This allows for the possibility of observation of the relative splitting between the parallel and antiparallel angular momentum vortex states.

Consider again the electron vortex of Sec. III. The extrinsic spin-orbit coupling results may be used to find the approximate energy splitting of an electron in a vortex beam, traveling within the mean field generated by the beam current. For an electron vortex with $l = 1$, the electric field is of the order of a few hundred Vm^{-1}, giving a splitting of $\mathcal{E}$ of the following magnitude:

$$\Delta_{l=1} \approx 3\times10^{-13}\ \mathrm{eV}. \tag{78}$$

This is very small, too small for direct measurement within the electron microscope; however, an indirect measurement might be a possibility, such as those involving spin-flip processes of a spin-polarized beam.

In the optical vortex case, the role of the external field is played by the refractive index of an inhomogeneous, anisotropic medium (Marrucci, Manzo, and Paparo, 2006). The coupling between the spin and orbital angular momentum of light has been exploited in the generation of polarized optical vortices, using specially structured liquid crystal cells, known as q plates (Marrucci, Manzo, and Paparo, 2006; Marrucci, 2013). Particular choices of the liquid crystal structure allow for the complete conversion of spin angular momentum into orbital angular momentum, controlling the sign of the resulting OAM through the polarization of the input mode. A similar conversion process for electron vortex beams, involving q plates with a specially structured magnetic field configuration, has also been proposed (Karimi *et al.*, 2012; Grillo *et al.*, 2013).

E. Electron vortex in the presence of laser fields

The Schrödinger equation of a quasirelativistic electron vortex beam in the presence of an electromagnetic field was set out in Lloyd, Babiker, and Yuan (2012a). For relativistic electron beams, a second-order Dirac equation incorporating a transverse electromagnetic field $\mathbf{A}$ is given by ($c = 1$)

$$\left[(\hat{\mathbf{p}} - e\mathbf{A})^2 - m^2 - \frac{ie}{2}F_{\mu\nu}\sigma^{\mu\nu}\right]\Psi = 0, \tag{79}$$

where $\hat{\mathbf{p}}^\mu = (i\partial_t, -i\nabla)$ is the electron four momentum operator, and $F_{\mu\nu} = \partial_\mu A_\nu - \partial_\nu A_\mu$ is the electromagnetic field tensor. $\sigma^{\mu\nu}$ is the spin tensor defined by $2\sigma^{\mu\nu} = \gamma^\mu\gamma^\nu - \gamma^\nu\gamma^\mu$, with γ^μ the 4×4 Dirac matrices. Bialynicki-Birula and Radożycki (2006) showed that classical (cyclotron) and quantum (Landau) orbits of a charged particle in a constant magnetic field can be controlled by electromagnetic waves with embedded vortex lines.

One area of interest is in the interaction of the electron vortex beam in the presence of a strong field generated by an ultrashort light pulse. Hayrapetyan *et al.* (2014) examined the case of a head-on collision of a relativistic electron vortex beam and a short laser pulse and showed that the orbital angular momentum components of the laser field couple to the total angular momentum of the electrons, causing the center of the beam to be shifted with respect to the center of the field-free electron vortex beam. Theoretical estimates suggest that a shift of 0.02 nm may be induced in a 300 kV electron vortex beam using a moderately strong laser pulse, so experimental observation is challenging but feasible.

Ivanov (2012b) considered the case for electron-photon interactions and demonstrated the entanglement arising from conservation of the sum of the helicity shown in Eq. (80) for particle-particle collisions also applies in the case of electron-photon interactions. There are also plans to use inverse Compton scattering of laser light by electron vortex beams

to generate structured x-ray beams (Seipt, Surzhykov, and Fritzsche, 2014).

In addition to the dynamics of the interactions of freely propagating vortices and antivortices, collisions between electrons and other particles carrying orbital angular momentum may also be considered (Ivanov and Serbo, 2011; Jentschura and Serbo, 2011; Ivanov, 2012b; Seipt, Surzhykov, and Fritzsche, 2014), with implications for generating high energy vortices of various species. In such two-particle scattering situations, there are several possible outcomes—the particles may be scattered to a range of final states, including plane-plane or vortex-plane wave states (Ivanov and Serbo, 2011; Jentschura and Serbo, 2011), or vortex-vortex entangled states (Ivanov, 2012b). In high energy electron-particle scattering, due to the scattering geometry, such collision processes are suitably described by consideration of the orbital helicity of each particle, i.e., the projection of the orbital angular momentum onto the particles momentum. When both particles are allowed to scatter into a final vortex state from an initial plane-vortex collision it is found that there are 2 degrees of entanglement between the two states—the transverse momentum $k_\perp$ and the orbital helicity Σ. It is found that the sum of the helicities of the two final states is approximately the same as the helicity of the incident vortex state, i.e.,

$$\Sigma_{f,1} + \Sigma_{f,2} \approx \Sigma_i, \tag{80}$$

the larger helicity tending to accompany the larger transverse momentum, which may fall within a range determined by the transverse momentum of the incident vortex (Ivanov, 2012b). This result may be applied to generate vortex-entangled particles or different species by collision, or additionally opens up the possibility of applying vortex states to high energy particle physics through colliding high energy vortex electrons with protons or other particles.

IV. GENERATION OF ELECTRON VORTEX BEAMS

Because of the similarities between the wave equations for electron and optical vortices, it has in many cases been relatively straightforward to adapt successful ideas from optical vortex research to similar ends in electron vortex applications. For the particulars of optical vortex generation, we refer the interested reader to the more recent reviews (Molina-Terriza, Torres, and Torner, 2007; Yao and Padgett, 2011). Broadly, the methods by which electron vortex beams may be generated may be classified into three main categories involving phase plates, diffractive optics, and electron optics, with those based on phase plates and diffractive optics being analogs of optical vortex technologies and electron optics methods forming an entirely new area. Initial success in electron vortex beam production involved materials-based diffractive elements and phase plates; however, the electron optics approach appears promising in terms of versatility and overcoming the efficiency limitations of the holographic plates (Yuan, 2014). In addition, photoemission was considered to be a possible source of electron vortex beams (Takahashi and Nagaosa, 2015).

A. Phase plate technology

The concept of the phase plate for an electron beam is not new (Nagayama, 2011), with early examples such as the Zernike phase plate designed for enhancing phase contrast of biological materials (Kanaya *et al.*, 1958). In the absence of any external fields, the effective refractive index for an electron traveling within a solid is given by (Reimer and Kohl, 2008)

$$n_{\text{eff}} = 1 - \frac{eU}{\mathcal{E}} \frac{\mathcal{E}_0 + \mathcal{E}}{2\mathcal{E}_0 + \mathcal{E}}, \tag{81}$$

where $\mathcal{E}_0$ is the electron rest mass energy, $\mathcal{E}$ is the kinetic energy of the incident electron, and U is the material specific mean inner potential. For example, n_{eff} is approximately 1.000 82 in silicon nitride for 100 keV electrons. The relative phase shift for a material of thickness Δt is then given by

$$\Delta\phi = 2\pi(n_{\text{eff}} - 1)\frac{\Delta t}{\lambda}. \tag{82}$$

For example, to achieve a relative phase delay of π for a 200 keV beam, which has a wavelength of 2.5 pm, a thickness difference in a silicon nitride film of 42 nm is required (Shiloh *et al.*, 2014); the precise thickness may vary (Bhattacharyya, Koch, and Rühle, 2006; Grillo, Gazzadi *et al.*, 2014; Harvey *et al.*, 2014) depending on many experimental factors such as the crystallinity of the film or the surface coating both intended and incidental such as carbon contamination.

Spiral phase plates are well known in optical vortex beam generation (Turnbull, 1996; Sueda *et al.*, 2004; Yao and Padgett, 2011) and consist of a thin film plate of a refractive material whose thickness changes continuously about the axis. The helical shaped thickness profiles of the plates impart angular momenta to a transmitting laser beam. Phase plates may be produced for millimeter wavelengths down to optical wavelengths (Turnbull, 1996; Sueda *et al.*, 2004; Yao and Padgett, 2011).

The first experimental demonstration of an electron vortex beam by Uchida and Tonomura (2010) involved the use of a stepped spiral phase plate constructed of stacked graphite flakes. Their stepped phase plate was made of spontaneously stacked flakes of graphite, leading to a discrete rather than a continuous change of its thickness profile. The edges of the steps cause extra phase jumps to appear at different points in the beam cross section in addition to the discrete 2π phase change of the desired vortex structure. This was observed in Uchida and Tonomura's experimental results via interference patterns and in-plane phase profile. The transmitted beam thus did not demonstrate the required characteristics of a pure vortex state with integer orbital angular momentum, but was nevertheless the first experimental demonstration of a freely propagating mixed vortex state. However, the particular arrangement of the graphite flakes cannot be properly controlled and they lead to phase defects. In addition, being made of carbon, under the influence of the high energy electron beam the flakes are subject to damage and deformation, and the phase plate loses its integrity. As such, the stepped graphite

phase plate is not suitable for long-term, reproducible vortex generation.

The production of continuous spiral phase plates was recently attempted using focused ion beam etching of a silicon nitride membrane (Shiloh *et al.*, 2014). However, the resulting doughnut-shaped beam profile has an opening, indicating a noninteger vortex beam has been produced (Berry, 2004), probably because of the difficulty of achieving precise refractive index and wavelength matching requirements. It was estimated that 1 nm thickness error results in 2%–3% unwanted variation in phase. On the other hand, a similar phase variation can be obtained by a change of 1 kV in the electron energy, indicating that there is some room for adjustment after the phase plate has been made. Thus the challenge of fabricating the spiral phase plate for the electron vortex beam is to produce a thickness profile to the required smoothness and precision. Another inherent problem of using matter-based electron-optical elements is the unavoidable scattering of the transmitted electrons other than those arising from mean inner potential. This can cause undesired effects such as additional phase shift or loss of coherence.

B. Holographic diffractive optics

Holographic reconstruction is a well-known technique in both optical and electron microscopy (Gabor, 1948; Tonomura, 1987; Saleh and Teich, 1991). It was used to increase image resolution by reconstructing the image from the interference pattern between the diffracted and nondiffracted components of the incident wave. The same principles of holography may be used to reconstruct an image or a wave function. The method involves passing an input wave through a computer generated hologram (CGH) generated via the interference between a reference wave and the required output mode. Most of the holographic diffractive optical masks produced to date are constructed out of thin membrane films of materials such as silicon nitride. This either can be of varying thicknesses for phase grating structures or can be of a uniform thickness with additional heavy metal coating, forming a binary amplitude grating structure. There was also a proposal to use the Kapitza-Dirac effect to produce electron vortex beams by the formation of optical dislocated gratings (Handali, Shakya, and Barwick, 2015). When a pulsed laser source is used this method enables pulsed electron vortex beams to be produced for use in time-resolved studies.

The holograms employed in vortex optics are constructed from the interference pattern between the vortex mode and a nonvortex reference wave:

$$I^2_{\mathrm{holo}}(\mathbf{r}) = |\psi_{\mathrm{vortex}} + \psi_{\mathrm{ref}}|^2, \tag{83}$$

where the choice is often for the reference wave to be a tilted plane wave, although other waves such as spherical reference waves (Saitoh *et al.*, 2012; Verbeeck, He Tian, and Béché, 2012) can also be used.

The holographic masks for vortex beam generation are versatile and are relatively easy to produce, however, they also have their drawbacks. Most of the masks reported to date are based on binary amplitude modulation holography (Verbeeck, Tian, and Schattschneider, 2010; McMorran *et al.*, 2011; Clark *et al.*, 2012), and as such produce very low intensity in the desired diffraction orders of approximately 6% of the incident beam intensity. This is because most of the beam intensity incident on the mask is blocked, although improvements have recently been reported with the use of phase modulation holograms (see Sec. IV.B.3). Furthermore, since multiple diffraction modes are produced in the binary holographic mask, the isolation of a mode of interest for specific applications can be tricky (Idrobo and Pennycook, 2011; Krivanek *et al.*, 2014; Pohl *et al.*, 2016) and this feature limits the practical use of holographic masks as a vortex beam generator.

1. Binarized amplitude mask

Direct interference of a vortex beam with a plane reference wave produces a characteristic pattern of fringes with smoothly varying intensity. The reproduction of this continuous variation, in terms of varying either film thickness or some other properties of the materials, is as or even more technically demanding as the fabrication of a smoothly varying spiral phase plate. A more practical alternative is to replace the continuous intensity variation by a discrete variation, such as the selective total removal of material in order to mask the beam, where empty spaces correspond to fringe maxima, and material regions of beam blocking thickness correspond to minima of the interference pattern. Such a mask is known as a binary amplitude hologram and is well known in optics (Lee, 1979). For electron beams, binary holographic masks may be relatively simply fabricated by focused ion beam (FIB) etching or electron lithography. Using such a binarized CGH mask, Verbeeck, Tian, and Schattschneider (2010) produced the first pure electron vortex beam. The principles behind generating a suitable binarized transmission grating can be demonstrated using the case of a simple vortex mode traveling in the z direction (neglecting any normalization factors, see Sec. II.B.3) given by

$$\psi_{\mathrm{vortex}}(\mathbf{r}) \equiv \psi_l(\mathbf{r}) = e^{il\phi}e^{ik_z z}. \tag{84}$$

The hologram pattern is generated by the interference of this mode with a reference plane wave traveling at an angle such that k_x is the component of the plane wave momentum orthogonal to the z direction:

$$\psi_{\mathrm{ref}}(\mathbf{r}) \equiv \psi_p(\mathbf{r}) = e^{ik_x x}e^{ik_z z}. \tag{85}$$

Any component of the plane wave momentum in the z direction does not contribute to the interference pattern. The interference is constructed by evaluating the superposition of the two waves at $z = 0$:

$$I_{\mathrm{holo}} = \tfrac{1}{4}|\psi_l + \psi_p|^2, \tag{86}$$

which is particular to the beam of interest. The prefactor is chosen to produce a pattern which oscillates between 0 and 1. For the phase vortex, the characteristic pattern is an edge dislocation, with $l + 1$ edges, also known as a fork dislocation. The interference pattern may then be binarized by clipping the pattern, for example,

$$I^{bi}_{\text{holo}}(\rho,\phi) = \begin{cases} 1 & I_{\text{holo}} \geq 0.5, \quad \rho \leq R_{\max}, \\ 0 & I_{\text{holo}} < 0.5, \quad \rho > R_{\max}, \end{cases} \tag{87}$$

for a maximum aperture radius $R_{\max}$. A similar process has been followed to produce holographic masks using Bessel or Laguerre-Gaussian vortex functions (Clark *et al.*, 2012). Despite the different radial structures of the Bessel, Laguerre-Gaussian, or the simple vortex beam of Eq. (84), the resulting binarized holographic masks are very similar (Clark *et al.*, 2012), indicating the binarization primarily picks out the strong intensity modulation due to the phase variation and "irons out" the more subtle amplitude variation of the different types of vortex modes.

The binary masks for $l = 1$ and $l = 3$ Bessel beams are displayed in Fig. 12, showing the corresponding $l + 1$ edge dislocations. Such mask patterns are then embedded into something opaque to the radiation of interest—a printed film (Heckenberg, McDuff, Smith, Rubinsztein-Dunlop, and Wegener, 1992; Heckenberg, McDuff, Smith, and White, 1992) or a spatial light modulator (Yao and Padgett, 2011) for optical beams, or in the case of electron beams a FIB etched metal or silicon nitride film (Verbeeck, Tian, and Schattschneider, 2010; McMorran *et al.*, 2011)—and placed into the path of the incident beam. Diffraction of the beam through the masks produces the desired vortex beams.

The far-field diffraction pattern resulting from the transmission of a plane wave through a CGH mask is given by the Fourier transform of the mask. This produces a nondiffracted zero-order beam, along with a series of vortex beams and their complex conjugates. From ordinary diffraction grating theory, we know that even harmonics will be absent if the widths of the masked grating elements are half of their spacing (Born *et al.*, 1997). When this condition is only approximately satisfied, a common occurrence for many binary amplitude masks, the odd order diffraction beams are usually more intense than the even order beams. An example for the diffraction of a binary amplitude CGH mask is shown in Fig. 13.

A characteristic feature of the binarization process is to introduce higher diffraction orders, generated from the step edge approximation to the sinusoidal transmission variation expected from the straightforward superposition of the vortex and the reference waves. This allows for the generation of higher order vortex beams than those encoding the original interference pattern, due to the inclusion of the high order harmonics of the original superposition in the binary holographic mask. Taking advantage of this mechanism, very high orders of orbital angular momentum have been demonstrated in electron beams. Using a CGH mask designed for $l = 25$ beams, vortices with $l = 100$ have been demonstrated (McMorran *et al.*, 2011). Naturally, these higher order diffracted beams are significantly less intense than the first-order beams. Recently, it was shown that an electron vortex beam of winding number $l = 200$ can be generated from the first-order diffraction peak (Grillo *et al.*, 2015).

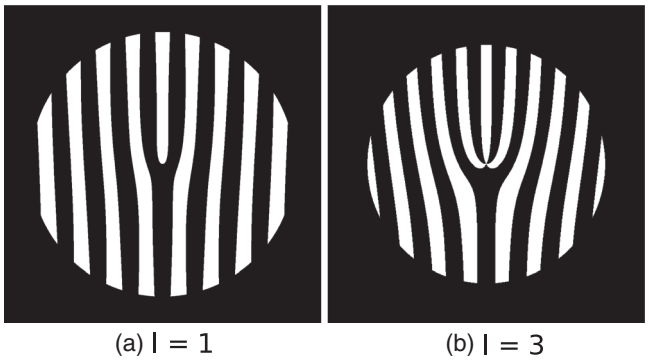

FIG. 12. The typical forked mask pattern produced by binarization of the interference pattern between a Bessel vortex wave and a plane reference wave for (a) $l = 1$ beam, and (b) $l = 3$ beam.

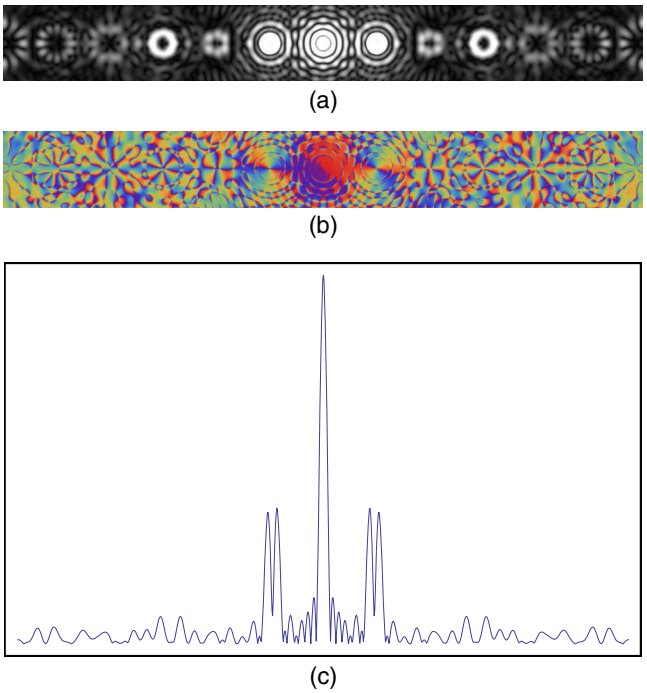

FIG. 13. The far-field diffraction pattern and phase distribution of the binary CGH amplitude mask to produce ($l = 1$, $p = 1$) FT-TBB beams shown in Fig. 7. (a) The diffracted beams, with several diffraction orders present; high intensity is indicated by white, zero by black. The phase of the beams is shown in (b), the opposite phase of the two sets of sidebands can be seen, with the nth order beams displaying a phase change of $2\pi n$. The rainbow scale indicates phase change from 0 (red) to 2π (purple). (c) The intensity of the various vortex beams. The central minima of all the diffracting beams are clear in the intensity patterns.

The CGH mask itself is not chiral, and so unlike a phase plate cannot impart orbital angular momentum to the transmitted beam by directly modulating the phase of the wave front. Instead, the mask decomposes the input plane wave into a set of left- and right-handed vortices, so that the vanishing total orbital angular momentum of the incident wave is conserved [and so the mask may also act as a mode analyzer (Saitoh *et al.*, 2012)]. The various diffraction orders propagate from the mask at some angle ϕ_s to the optical axis of the incident beam, so that in the far-field different vortex beams are angularly separated. The magnitude of the transverse wave vector of the reference wave k_x relative to the longitudinal wave vector k_z determines the angles at which the diffracted beams exit the hologram, such that a large k_x increases the

angular separation between the different diffracted orders (Heckenberg, McDuff, Smith, Rubinsztein-Dunlop, and Wegener, 1992; McMorran *et al.*, 2011). The angle of the first-order diffracted beam, for a Bessel vortex beam, is

$$\phi_s = \frac{\lambda}{d} = \frac{k_x}{k_z} \tag{88}$$

for grating separation d, which is related inversely to k_x. The nth order diffracted beam emerges at an angle $n\phi_s$ while the zero-order beam propagates along the original direction of the incident wave. A particular diffraction order of interest may be realigned to this optical axis by illuminating the hologram with a beam with transverse momentum nk_x (Schattschneider *et al.*, 2012). The transverse momentum of the vortex beam itself $k_\perp$ is determined by the size of the mask aperture; for the Bessel beam we have

$$k_\perp = \frac{\lambda_{1l}}{R_{\max}} \tag{89}$$

with $\lambda_{1l} \approx 3.81$ the first zero of the Bessel function $J_l(x)$. A similar relationship applies for other vortex beams. For example, in the case of the Laguerre-Gaussian modes, λ_{1l} is replaced by the relevant radius of the Laguerre-Gaussian mode at $z = 0$.

In a binary hologram, the phase information is encoded as a lateral shift of the interference fringes, suggesting that the phase structure of the vortex beam can be recovered whatever the shape of the fringe (Clark *et al.*, 2012).

CGH masks are much more versatile and controllable than spiral phase plates as described in Sec. IV.A. Each diffraction order is a pure phase vortex of strength nl as each is a unique vortex "harmonic" of the incident vortex beam with orbital angular momentum of integer order $l\hbar$. The CGH masks may be constructed out of materials that are resistant to beam damage and will have a longer useful lifetime than a spiral phase plate constructed of graphite thin films; in addition the results are directly reproducible, and in principle any order of orbital angular momentum may be specified, as demonstrated by the production of electron vortex beams with high values of orbital angular momentum (McMorran *et al.*, 2011). On the other hand, note that the binary CGH mask itself will block much of the incoming beam, so that only ~50% of the incident intensity is transmitted. Approximately 25% of the incident intensity is channeled into the zero-order beam, with the higher order beam decreasing in intensity. The first-order diffracted beams share ~12% of the incident intensity, which is not sufficient for many experimental applications.

Forked apertures have been used to generate electron vortices in transmission electron microscopes (TEM) (Verbeeck, Tian, and Schattschneider, 2010; McMorran *et al.*, 2011; Verbeeck *et al.*, 2011; Schattschneider *et al.*, 2012) and are now a standard technique in experimental electron vortex physics. The first proof-of-principle demonstration involved a 5 μm diameter CGH mask cut from platinum foil, with a single fork dislocation generating left- and right-handed vortex beams. The second instance of this holographic vortex generation involved silicon nitride films milled with very high resolution features (McMorran *et al.*, 2011); the high resolution milling allowed for the cutting of narrowly spaced gratinglike linear patterns, so that the diffracting beams produced had a large angular separation. The high resolution milling also enabled the fine features of holographic masks for generating vortex beams of higher order to be accurately reproduced. A forked mask encoding a vortex beam with a topological charge $l = 25$ was demonstrated. For structural stability of this fine featured CGH mask, the edge dislocation is not reproduced within the central region. However, leaving a solid block at the very center of the mask did not seem to significantly impair the function of the mask, and vortices with clear central dark cores were produced with the fourth-order diffracted beam carrying $100\hbar$ orbital angular momentum (McMorran *et al.*, 2011), demonstrating the versatility of the uses of binary CGH masks over spiral phase plates.

The phase structure and vorticity of the resulting beams were confirmed by observation of the forked interference fringes (Verbeeck, Tian, and Schattschneider, 2010; McMorran *et al.*, 2011), and by the persistence of the axial dark core of the vortex on propagation and diffraction (McMorran *et al.*, 2011). A beam that simply has an annular profile will spread radially both inward and outward, obliterating the central zero intensity away from the focal point, whereas a beam with a phase singularity must preserve this singularity as the orbital angular momentum must be conserved.

2. Binary phase mask

The binarized CGH masks rely on the amplitude modulation of the transmitted wave in order to separate the orbital angular momentum components. Diffraction can also occur through a phase modulating CGH grating (Grillo, Karimi *et al.*, 2014; Harvey *et al.*, 2014) and offers an alternative method for the generation of vortex beams.

As in the case of the phase plate technology, a phase CGH mask can be produced by imprinting the desired phase change into a silicon nitride film with the thickness variation given by

$$\Delta\phi(\rho,\phi) = CU\Delta t(\rho,\phi), \tag{90}$$

where C is a coefficient determined by the energy of the electron beam and U is the mean inner potential as defined in the context of Eq. (81). The advantages of the phase grating technique are the increased control over the radial structure of the vortex beam and that it could potentially enable higher intensities to be transmitted into desired orders.

As a demonstration of the control of the radial structure of the vortex beams, Grillo, Karimi *et al.* (2014) were able to demonstrate approximate nondiffracting and self-healing electron Bessel beams over a range of 0.4 m (compared with 0.16 m for a conventional electron beam with the same spot size). This was done by encoding the following phase modulation into a phase mask:

$$\Delta\phi_l(\rho,\phi) = \Delta\phi_0 \mathrm{sgn}\left[\cos\left(k_\perp\rho + l\phi + \frac{2\pi}{d}\rho\cos\phi\right)\right], \tag{91}$$

where $\Delta\phi_0$ and d are the maximum size of the phase modulation and the wavelength of the reference plane wave

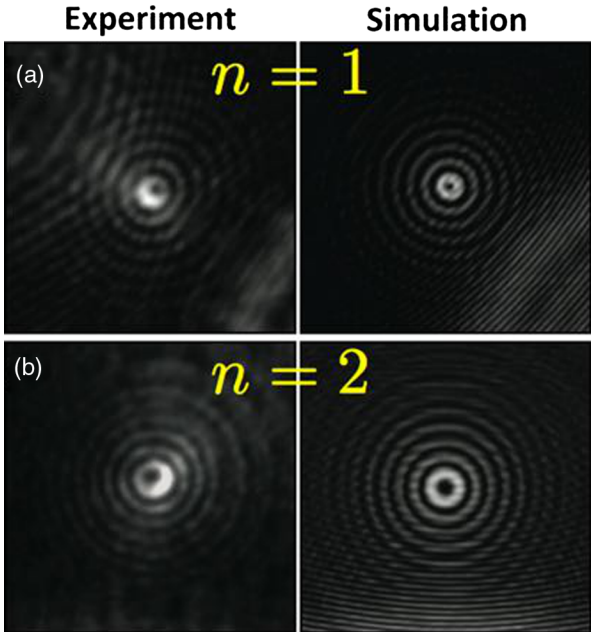

FIG. 14. Comparison of the theory and the simulation of the nonzero order approximate Bessel-type electron vortex beam. The topological order of the beams is denoted by n, which is identical to the l defined in this review. Adapted from Grillo, Karimi *et al.*, 2014.

used, respectively, and other symbols have the meaning defined in Eq. (14). Figure 14 shows two kinds of nonzero order beams representing approximate vortex Bessel beams. The multiple ring structure seen is a characteristic of the electron probability distribution of the Bessel beam. The nondiffracting nature has been observed both in the optical (McGloin and Dholakia, 2005) and now also in the electron Bessel beams (Grillo, Karimi *et al.*, 2014).

The nondiffractive nature of the electron Bessel beams might be particularly useful in electron tomography (Midgley and Dunin-Borkowski, 2009), where it can enable different planes within a material to be imaged with the same resolution, without the need to correct for the focus.

As almost all the electrons are transmitted through the phase holographic mask, the efficiency of vortex beam generation is expected to be higher than that of the amplitude holographic mask. For an ideal binary phase holographic mask, the power of diffracted electrons at the first order of diffraction can reach up to approximately 40% of the incident beam (Magnusson and Gaylord, 1978), which is about 4 times higher than that generated by the amplitude holograms. However, the pattern generated in the FIB turns into an approximate sinusoidal form, and thus the efficiency of the generated beam is approximately 17% smaller than an ideal binary profile (40%) with the same size of the thickness variation (Grillo, Karimi *et al.*, 2014; Harvey *et al.*, 2014).

3. Blazed phase mask

The increase in efficiency is an important goal for electron vortex beam generation (Yuan, 2014), since significant improvements in vortex beam brightness are required for the various applications currently being pursued. Using a

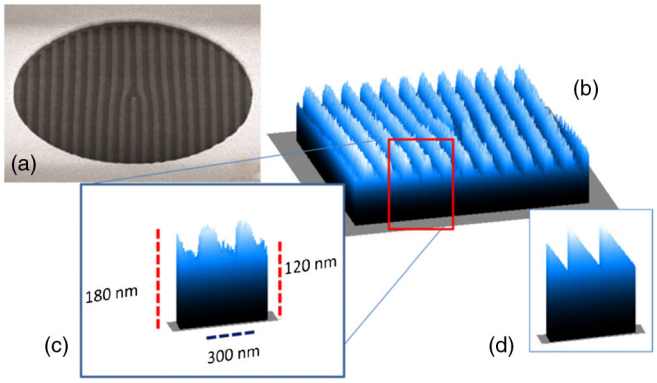

FIG. 15. The blazed phase grating. (a) An SEM image of the mask, with electron-energy-loss measured thickness profile in (b). (c) Typical heights of the grating maxima and minima, with an ideal blazed profile in (d) for comparison. Adapted from Grillo, Gazzadi *et al.*, 2014.

blazed grating approach, Grillo *et al.* demonstrated increased transmission of 25% intensity into the $l = 1$ vortex mode. As before, the specific pattern to be milled is the characteristic forked pattern; however, with the introduction of blazing to the grating pattern, a higher intensity may be projected into the desired mode. As can be seen in Fig. 15 the mask fabricated by Grillo, Gazzadi *et al.* (2014) was a good approximation to a perfectly blazed grating, and as such the results show a significant intensity decrease in the zero-order $l = 0$ vortex, with substantial increase in the first-order beam with $l = 1$; the intensity distribution of the diffraction orders is now strongly asymmetric.

Nevertheless, one fundamental issue with this phase hologram approach is the inevitable energy spread that will arise within the beam, due to the inelastic scattering of electrons as they pass through the mask. For certain applications this will not be a problem as the inelastically scattered components of the electron beam can be removed by energy filtering. However, for applications such as spectroscopy, this may result in unacceptable loss of intensity and the presence of inelastically scattered components. In such instances, the use of a purely phase shifting device such as those using electron optics alone will be required.

Note that the theoretical maximum efficiency for an ideal blazed phase hologram is 100% in optics. As no absorption and scattering are involved, this value refers to both absolute efficiency and relative transmitted efficiency in optics (Grillo, Gazzadi *et al.*, 2014). In the context of refractive-material-based blazed gratings for electron vortex beam generation, the absolute generation efficiency will be limited by the inevitable large angle elastic scattering and incoherence due to inelastic scattering processes. As a result, the absolute efficiency is much lower than the relative transmission efficiency for the electron vortex case. At the time of writing of this review, the best transmission efficiency reported by Grillo *et al.* (2016) is 37% out of a theoretical limit of 38% for their partially blazed phase mask. On the other hand, McMorran *et al.* (2017) reported a much larger value of 70% for the absolute transmission efficiency for their blazed mask. Clearly more work is needed to investigate the practical limits to the generation efficiencies using optimized blazed phase masks.

4. Choice of reference waves

The holographic mask production techniques outlined may also be applied with different reference waves. Another common choice in optics is a wave with a spherical wave front (Heckenberg, McDuff, Smith, Rubinsztein-Dunlop, and Wegener, 1992; Kotlyar *et al.*, 2006), sharing an axis with the desired mode. This also produces a characteristic interference pattern, a spiral with l arms, as shown for the $l = 1$ and 3 vortices in Fig. 16, alongside the corresponding binarized mask. The action of these holographic masks on an incident plane wave is very similar to that described for the forked mask; however, instead of the beams being separated by an angle, they are separated along the propagation direction. For the $l = 0$ nonvortex beam, the use of a spherical reference wave of curvature $1/f$ results in the familiar Fresnel zone plate, as shown in Figs. 16(a) and 16(d). The vortex and zero-order modes transmitted through the spiral hologram produced using this reference spherical wave focuses at different points separated by a distance f (Heckenberg, McDuff, Smith, and White, 1992; Verbeeck, He Tian, and Béché, 2012). When the beam as a whole is properly focused by an electron lens, the zero-order beam will be in the focal plane of the electron lens, while the first-order diffracted beams are focused at a distance f in front and behind the focal plane of the electron lens. For electron microscopy, this has the advantage that overfocusing or underfocusing the beam enables the different vortices to be brought into focus onto the focal plane, where they may then be utilized with minimum involvement from the other orders in the beam (Verbeeck, He Tian, and Béché, 2012). Unlike the forked masks, these underfocused or overfocused vortex beams should be useful for scanning electron microscopy (SEM); although the additional vortex modes will lead to a background contribution, reducing the signal-to-noise ratio of the vortex mode in focus.

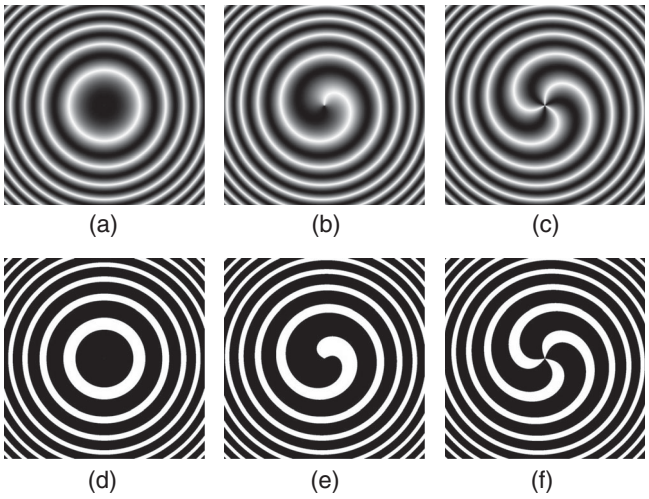

FIG. 16. Spiral interference patterns and masks of vortices interfering with spherical waves. (a) The in-plane intensity pattern for a nonvortex beam interfering with an outward propagating spherical wave; binarization of this intensity pattern, forming a Fresnel zone plate, is shown in (d). (b), (e) The continuous and binarized interference patterns, respectively, for an $l = 1$ vortex beam interfering with the spherical wave. (c), (f) The same for the $l = 3$ vortex beam.

The use of a spiral holographic mask was demonstrated for electron vortices of various topological charges (Saitoh *et al.*, 2012; Verbeeck, He Tian, and Béché, 2012). As with the high order forked mask of McMorran *et al.* (2011), the stability of the mask structure requires a reinforced (Saitoh *et al.*, 2012) center or supporting struts (Verbeeck, He Tian, and Béché, 2012); it was found in both simulations and experiments that the supporting struts did not significantly impair the integrity of the vortices produced (Verbeeck, He Tian, and Béché, 2012). However, one issue with the application of a spiral mask is that the coaxial presence of the different diffraction orders leads to a relatively large background signal, causing the intensity of the center of the vortex to be increased from zero (Verbeeck, He Tian, and Béché, 2012). In order to reduce this overlapping effect as much as possible, the focal length of the corresponding Fresnel zone plate must be very long. A long focal length f means the arms of the spiral would rapidly decrease in separation toward the edge of the aperture. This requires very fine features in the holographic mask, a requirement similar to the case involving a large k_x giving a high diffraction angle ϕ_s and decreasing the grating separation Eq. (89) in the dislocated grating mask. Additionally a highly coherent beam with a large convergence angle is required, stretching the limits of current microscope and FIB technology.

C. Electron optics methods

Material-based electron optics is not flexible, requiring a specific mask for a single type of beam generation, and is also highly inefficient. In general, modern electron microscopy avoids the use of such elements, instead relying almost exclusively on carefully controlled electrostatic and magnetic interactions to control the trajectory of the electron beams. With the exception of apertures, the shaping of the electron beam is in general accomplished by purely phase-transforming devices.

Modern aberration-corrected electron microscopy already has many multiple lenses in addition to the standard round lens (Rose, 2008). These existing multiple lens systems have been exploited to generate a structured phase shift to covert a nonvortex beam into a beam containing electron vortices, with the promise of high efficiency (Clark *et al.*, 2013). In addition, the lens aberration itself has also been used by Petersen *et al.* (2013) to show that electron diffraction catastrophes can be created in this way, containing arrays of intensity zeros threading vortex cores.

1. Spin-to-orbital angular momentum conversion

One possibility is the generation of electron vortices from spin-polarized electron beams using q filters, in analogy with the q plates of optics. So called "q plates" have been available in optics since 2006 and have found applications in quantum information; these devices are based on patterned liquid crystal (LC) filters which allow the conversion of spin-polarized optical beams to oppositely spin-polarized vortex beams (Marrucci, Manzo, and Paparo, 2006; Marrucci *et al.*, 2012). The action of the q plate is based on the birefringent action of the LC which is also inhomogeneously patterned,

such that spin and orbital angular momenta are exchanged between the beam and the LC. The LC thickness and patterning may be tuned in such a way as to facilitate the transfer of the spin and angular momentum of the beam, such that changes of spin angular momentum by 2 are accompanied by a change in OAM of $-2q$, where q refers to the order of the singular defect of the patterning of the LC optic axis. Other, more complex LC patterning may also be utilized to produce vector beams with specific polarization profiles (Cardano *et al.*, 2012).

In an electron spin-to-orbital angular momentum conversion device the conversion effect is produced by the action of a spatially varying magnetic field on the beam over a specifically matched length, inducing a spatially dependent geometric (Berry) phase (Karimi *et al.*, 2012). Such a device takes the form of a spatially inhomogeneous Wien filter, with the trajectory altering action of the magnetic field balanced by the presence of an orthogonal electric field with the same spatial inhomogeneity. As with the LC filter, the multipolar fields of the electron q filters also contain a topological defect (a field zero) at the center, the order of which determines the value of q. Quadrupole fields give a q value of -1, for hexapole fields $q = -2$, and so forth. The filter is most effective for annular beams, so that it is more efficient to add or subtract q units of orbital angular momentum from a vortex beam (for example, for discrimination between different vortex modes) rather than create a vortex beam from a Gaussian or other nonvortex beam.

Upon transmission through the q filter a precession of the electron spin is induced by the magnetic field. This is accompanied by a position-dependent geometric (Berry) phase shift, which is the source of the orbital angular momentum of the resulting beam (Karimi *et al.*, 2012). The two spin components of the electron beams are oppositely affected, so that the resulting beam is in a mixed state having orbital angular momentum $l \pm q$ and spin angular momentum $\mp 1/2$ (Schattschneider, Grillo, and Aubry, 2017). Since high brightness spin-polarized electron beams are not currently available, the q filter is not viable as a method of generating useful electron vortices; however, conversely the q filter may be used with $l = \pm 1$ vortex beam and appropriate apertures and OAM sorters to obtain nonvortex spin-polarized electron probes for various applications (Karimi *et al.*, 2012, 2014; Grillo *et al.*, 2013).

2. Magnetic monopole field

The field distribution of a magnetic monopole provided the ideal phase shift to convert a plane wave into a vortex beam (Wu and Yang, 1976). Such a monopole field has been considered for use in electron microscopy as early as 1992 (Kruit and Lenc, 1992). In the absence of such monopoles, the edge fields of a suitable thin wire magnetized along its long axis have been shown to induce a phase ramp around the beam that approaches 2π (Béché *et al.*, 2013; Blackburn and Loudon, 2014), opening the possibility of producing high-intensity vortex beams, in addition to improvements in phase contrast imaging. This method is potentially versatile, since the phase change of the beam depends on the magnetic flux contained within the needle, so that higher and noninteger vortex states may also be created (Blackburn and Loudon, 2014). When such a needle is placed in the middle of the aperture for the vortex forming lens, over 90% incident beam can be converted (Béché, Juchtmans, and Verbeeck, 2017). This high efficiency is a very useful property for many applications. This method also has the distinct feature to be independent of the energy of the electron beam, making it a potential avenue for producing ultrashort pulsed electron vortex beams. The main challenges in the use of monopolelike fields to create vortices will be the control of the fields themselves—the field geometry and strength are significantly affected by the thickness, width, and magnetization of the needle. Slight artifacts of the fabrication process may substantially affect the shape of the fields, as discussed in detail by Blackburn and Loudon (2014), resulting in some mixing of different vortex states (Béché, Juchtmans, and Verbeeck, 2017).

3. Vortex lattices

Vortices were originally described as screw-type dislocations in wave fields produced by the interference of three or more plane waves (Nye and Berry, 1974). In electron holography (Tonomura, 1987), electrostatic biprisms have been used to split the wave front of a plane wave into two tilted plane waves which are then deflected toward each other to produce standing wave patterns in the overlap region. By using two electrostatic prisms, we can obtain two overlapping standing waves. The crossings of the nodal lines in the standing waves are locations of vortices which form a regular array. Both square and triangular arrays of vortices are produced in this manner by adjusting the relative angles of the two sets of standing waves (Niermann, Verbeeck, and Lehmann, 2014; Dwyer *et al.*, 2015). Such lattices will have a pattern of vortices and antivortices regularly arranged, with locally varying orbital angular momentum density. In the square lattice, the resulting wave front contains an array of dark spots, phase singularities of topological strength $|l| = 1$ with phase circulation alternately left- or right-handed about adjacent cores. In practice, due to position-dependent phase shifting aberrations within the electron lenses or that caused by the sample, there is an overall shift in the position of the vortex cores across the array. This effect can be used to map out the phase shift in the electron-optical systems or that caused by the sample. Regular vortex arrays may also find applications in spectroscopy, so that the analysis might be performed simultaneously over a larger region of the sample, while reducing the average distance between the vortex lines and the atoms, and thus the off-axis contributions (see Sec. VI.A) (Niermann, Verbeeck, and Lehmann, 2014).

A more complex form of interference of waves is that which causes diffraction catastrophes and caustics, which can also lead to the formation of vortex arrays (Nye, 2006; Petersen *et al.*, 2013). A lattice of vortex-antivortex pairs has been shown to surround the caustics formed from both astigmatic and coma induced diffraction catastrophes in the electron microscope, along with the existence of additional vortices inside the caustic. The wave fields of such caustics present the opportunity to study complex vortex behaviors with twisted vortex trajectories and loops being apparent (Petersen *et al.*, 2013).

D. Hybrid method

1. Lens aberrations

Clark *et al.* (2013) used electron-optical aberration to generate an azimuthal phase ramp at the back-focal plane to produce an isolated electron vortex beam. Comparison of the aberration correction series and the Fourier series of the vortex phase shows that a good approximation to the vortex phase ramp can be made by minimizing all aberrations except for the various orders of astigmatism. Matching the astigmatism to the desired phase shifts and applying an annular aperture to ensure beam passage through the relevant regions of the lens and corrector allow for the appropriate phase ramp to be created (Clark *et al.*, 2013). The beam generated experimentally using such a setup was demonstrated to be a good approximation to the $l = 1$ vortex mode, exhibiting the axial minimum and the 0 to 2π phase variation. The modal decomposition showed that only 32% of the transmitted beam was in the $l = 1$ vortex mode. However, the presence of other vortex modes and the clear spatial asymmetry of the beam demonstrate that the beam produced is not as pure as that created with holographic masks (Clark *et al.*, 2013). On the other hand, the intensity of the vortex generated is approximately twice that achieved using the amplitude binary holographic mask technique; this method is more efficient for the generation of the $|l| = 1$ vortex mode. However, the generation of higher order vortices may prove to be much more challenging due to the significantly steeper phase ramp required.

2. Electron vortex mode converter

A mode converter for electron beams has been described (Schattschneider, Stöger-Pollach, and Verbeeck, 2012), acting in an analogous way to laser mode converters in optics (Beijersbergen *et al.*, 1993). The electron vortex implementation involves making use of astigmatic correctors specific to the electron microscope, as well as the use of a Hilbert phase plate. This is therefore a hybrid technique encompassing the phase plate and electron optics approaches discussed.

The Laguerre-Gaussian vortex mode may be described as a linear superposition of two Hermite-Gaussian modes with a phase difference of $\pi/2$. The Hermite-Gaussian modes do not themselves carry orbital angular momentum, however by exploiting the difference in Gouy phase for astigmatic Hermite-Gaussian modes, such a superposition can be produced resulting in a Laguerre-Gaussian mode with well-defined orbital angular momentum and phase singularity (Beijersbergen *et al.*, 1993). The experimental procedure for electron vortices described by Schattschneider, Stöger-Pollach, and Verbeeck (2012) relies on a lens with variable astigmatism, so that the focal points of the x and y transverse parameters may be set independently. This may then be used to generate a Laguerre-Gaussian mode from a Hermite-Gaussian mode. An approximation to a Hermite-Gaussian mode has been generated using a Hilbert phase plate (Danev *et al.*, 2002), which imparts a phase shift of π between the two halves of the beam, similar to the phase difference of π between the two lobes of the Hermite-Gaussian mode. The Hermite-Gaussian mode is then passed through the astigmatic converter, oriented at 45° to the transverse axes of the astigmatic converter, so that the astigmatism acts on the two x and y components. The foci of the astigmatic lens are set so that a relative Gouy phase difference is created between the two transverse profiles in the back-focal plane to obtain a Laguerre-Gaussian beam profile (Schattschneider, Stöger-Pollach, and Verbeeck, 2012).

A proof-of-principle experimental result has been demonstrated. Although a phase singularity is apparent at the center of the back-focal plane, the resulting profile does not have rotational symmetry, and so the beam is not in a pure Laguerre-Gaussian mode. The discrepancy from the simulated results arises due to defocus and, importantly, strong beam absorption in transmission through the Hilbert phase plate (Schattschneider, Stöger-Pollach, and Verbeeck, 2012). Nevertheless, the electron vortex mode converter is an attractive prospect if these effects can be overcome, as it enables the generation of electron vortices of high intensity, of up to 90% of the incident plane wave intensity, as opposed to ≈6% using the holographic masks.

V. VORTEX BEAM ANALYSIS

Any study of the electron vortex beam will inevitably involve some characterization of its properties. This will also be useful in, for example, examining transfer of orbital angular momentum in experiments involving interactions with various forms of matter and light. We now briefly review the techniques that have been developed for electron vortex beam analysis.

A. Interferometry

The simplest approach is to examine the intensity profile of the beam cross section. For a given point in the wave front in a vortex beam, the existence of the conjugate point with antisymmetry in phase ensures that their coherent superposition on the beam axis will always lead to destructive interference. This is responsible for the persistence of the central dark spot in the vortex beam. Thus the observation of the doughnut ring in the beam cross section is taken to be a signature of a nonzero topological charge. However, we also need to know the sign and the magnitude of the topological charge and the radial structure. For example, the radial structure of the Laguerre-Gaussian beam is specified by the radial index p in Eq. (9). As for the identification of the pure OAM states, some progress has been made, as we summarize next.

1. Electron holography

The interference of a pure vortex beam with a plane reference wave results in a forked interference fringe, a property that is fundamental to the holographic mask technology introduced in Sec. IV.B. The interference experiment can be performed in an electron microscope equipped with an electron biprism (Tonomura, 1987). A biprism is usually a positively charged wire. Two halves of the wave front on either sides of the charged wire will experience transverse shear because the negatively charged electrons will be attracted toward the positively charged wire. The resulting

overlap of the wave fronts forms holographic fringes. If only a parallel beam falls onto the regions containing the charged wire, linear gratinglike interference structure will be observed. In traditional electron holography, a sample is inserted in the path of one-half of the split wave front so that the extra phase and amplitude modification can be recorded as the additional shift of the fringe as well as the modulation of the fringe contrast. In vortex beam analysis, the sample may be replaced by a vortex converter such as a spiral phase plate or an holographic diffraction mask. The vortex phase structure imprint on the interference fringes is a dislocation or a fork structure, such that the number of the forks in the interference pattern is equal to the magnitude of the topological charge and the orientation of the fork can be related to the sign of the topological charge of the beam. This electron holographic method was used by Uchida and Tonomura (2010) to demonstrate for the first time the phase structure of an electron vortex beam.

2. Knife-edge and triangle aperture diffractive interferometry

Electron holography using the electron biprisim technique is available only in specialized microscopes, so alternative methods had to be developed. The simplest holography method, without the use of an electronic biprism, is the knife-edge holography method. This creates a reference wave by utilizing the beam-bending effect associated with the Fresnel diffraction of electrons from the edge of an aperture. Verbeeck, Tian, and Schattschneider (2010) used this to demonstrate the production of vortex beams by a holographic mask.

A useful variation of this method is the use of a triangular aperture. The interference of the Fresnel fringes from three neighboring edges of the triangle results in a triangular lattice structure which depends strongly on the topological charge of the vortex beam (Hickmann *et al.*, 2010). It is then a simple matter to count the number of spots in the resulting interference pattern to determine the topological charge.

Note that these methods work only in out-of-focus conditions.

3. Diffraction

The phase structure of the vortex beam can also be studied by the diffraction method. A hologram mask can be used to determine the topological charge of the beam (Saitoh *et al.*, 2013; Guzzinati *et al.*, 2014). In this method, a forked grating structure, formed from the interference of a plane wave and a vortex wave of topological charge of l_{grating}, is used as a beam analyzer. The vortex beam is diffracted by the grating structure and the far-field diffraction pattern is examined. The diffraction of the dislocated grating adds $n \times l_{\text{grating}}$ to the topological charge of the resulting diffracted beams, where n is the order of the diffraction and takes the values of $0, \pm 1, \pm 2$, etc. The total topological charge of the diffracted beams is given by

$$m = nl_{\text{grating}} + l. \tag{92}$$

In particular, the diffracted beam with $m = 0$ has an intense central spot and so can be easily identified. This allows the OAM content of the incident beam to be easily determined using Eq. (92), if gratings with different topological charges are employed. Other methods such as the simple multiple pinhole plates have also been suggested, with mixed results due to possible effects such as aliasing effects (Clark *et al.*, 2014).

In general, the identification of the vortex beams of mixed orders is difficult. But Saitoh *et al.* (2013) suggested that if a pin-hole aperture is also used on the diffracted beam, the vortex beam can be sorted into different components according to their topological charge.

B. Mode conversion analysis

One of the simplest methods is based on the conversion of Hermite-Gaussian modes to generate Laguerre-Gaussian beams (Allen *et al.*, 1992; Courtial and Padgett, 1999). Here the mode conversion is run in reverse and the vortex beam is decomposed into Hermite-Gaussian beams with characteristic modes. In optics this is achieved using a cylindrical lens while in electron optics (Guzzinati *et al.*, 2014; Shiloh *et al.*, 2015) use is made of an astigmatism corrector which is readily available in a typical electron microscope. For higher order vortex beams, we might have mixed radial modes sharing the same OAM quantum number. This may result in a complex superposition of the pattern. Thus the method is more useful for vortex beams of small topological charges. The sign of the topological charge can be read out through the sense of the rotation of the resulting Hermite-Gaussian pattern because of the l-dependent Gouy rotation.

The approaches adopted so far can all be traced to original methods developed for characterizing optical vortex beams and they work well for single pure OAM states. The challenge occurs when one has to deal with mixed OAM states. Optical approaches such as multipoint interferometers (Berkhout and Beijersbergen, 2008), geometric transformations by phase manipulation (Berkhout *et al.*, 2010), and the use of multiple interferometers in a cascade setup (Leach *et al.*, 2004) are currently difficult to implement in the existing electron microscope setup, so a new approach is required especially for the characterization in the single electron region. For practical reasons, the holographic diffraction mask and the aperture masking methods are difficult to implement for atomic size vortex beams, making the astigmatism transformation method currently the most realistic method for atomic scale pure vortex beams. For efficient sorting of electron vortex beams in general, electron optics are preferred and a refractive device was recently proposed by McMorran *et al.* (2017).

C. Image rotation

Because the azimuthal dependence of a pure vortex beam is encoded in the phase factor $e^{il\phi}$ independent of z, the cross-sectional image of any pure vortex beam is circularly symmetric so any potential rotation is not detectable. This method is therefore not suitable for the characterization of the rotation of the pure states. On the other hand, the circular symmetry will be broken in a mixed state vortex beam, resulting in an asymmetrical cross-sectional beam intensity. This can be achieved by different methods, ranging from simply cutting a pure vortex beam by a knife-edge-like mask

to create an asymmetrical cross-sectional distribution (Guzzinati *et al.*, 2014), to the careful preparation of a superposition of pure vortex beams (Greenshields, Stamps, and Franke-Arnold, 2012) or a vortex-endowed C-shaped beam (Mousley *et al.*, 2015). The rotation of the transverse image of the electron vortex beam can be measured as a function of the propagation distance or as a function of the magnetic field strength. In that way, measurements of the image rotation along the z direction can be used to study the Zeeman or Gouy effects of the electron vortex beam (Schachinger *et al.*, 2015).

1. Gouy rotation

The Gouy phase is due to spatial confinement of the vortex beams near focus (Feng and Winful, 2001; Petersen *et al.*, 2014). In the absence of an external magnetic field or when the field strength is so small that the magnetic effect can be ignored to the first order, the main contribution to the image rotation is due to the variation of the Gouy phase difference between OAM beams with different topological charges. The Gouy phase difference changes rapidly near the beam waist, so that the Gouy rotation is most easily observed around the focus plane, as shown by Guzzinati *et al.* (2013).

2. Zeeman rotation

One of the consequences of using a magnetic lens to focus electron beams is that all electron beam trajectories with transverse velocity components undergo Larmor precession. In electron microscopy, this results in the well-known image rotation phenomenon (Reimer and Kohl, 2008). Early microscopists had to take this into account when comparing microscope images taken at different magnifications as the excitation of the magnetic field in the lens changes. In modern transmission microscopy, lens design is such that the rotation effect due to different lenses cancels out, so electron microscopists need not be concerned with such effect.

The presence of the external magnetic field also causes complex and interesting changes in the phase of the electron vortex beam as described in Sec. III. However, for nanoscale vortex beams that are being generated inside electron microscopes where the saturated field strength is typically on the order of 2 T, the effect of the magnetic field would be very weak (Babiker, Yuan, and Lembessis, 2015). To see the magnetic field induced rotation, one has to go to either much stronger magnetic fields or vortex beams of large transverse structures. In general, such rotation should be accompanied by changes in the radial direction due to competition of the beam diffraction and the confining effects of the magnetic field (Greenshields, Stamps, and Franke-Arnold, 2012). In special cases, when the vortex beam has the characteristic beam width w_B given in Eq. (58), one can study the rotation of the Landau states given by Eq. (62).

These image rotations have been experimentally observed in the electron microscope, for both the balanced and unbalanced superpositions (Guzzinati *et al.*, 2013). The experimental situation differs from the theoretical treatments previously outlined in that the fields are not uniform, and the beams have a well-defined focal plane. As such, the actions of the Zeeman and Gouy phase shifts both contribute, with the Gouy shifts dominating in the vicinity of the focus of the beam, due to the transverse confinement (Feng and Winful, 2001), and the Zeeman shift is more apparent at large radial distances from the beam axis, due to the magnetic fields of the lenses. For the unbalanced superposition, the difference between those states, with the net OAM aligned and antialigned with the direction of the magnetic field, is shown in the net addition of the separated rotations due to the Zeeman and Gouy terms (Guzzinati *et al.*, 2013). Such Zeeman-Gouy phase effects may find applications in vortex beam analysis, since this offers a method by which oppositely oriented vortices may be differentiated, by the observation, or lack of, image rotations in known magnetic fields. For beams with a Landau state transverse mode given by Eq. (62), rotation in either Larmor, cyclotron (double Larmor), or zero frequency have been observed (Schattschneider, Schachinger *et al.*, 2014), consistent with the prediction of Bliokh *et al.*, 2012. However, the use of the knife edge resulted in the mode broadening due to an approximate uncertainty principle for angular position and angular momentum (Franke-Arnold *et al.*, 2004), so the measurement cannot be taken for a vortex beam in a pure Landau state.

D. Vortex-vortex interactions and collisions

General considerations of vortex-vortex collisions have been discussed (Bialynicki-Birula, Bialynicka-Birula, and Śliwa, 2000; Bialynicki-Birula *et al.*, 2001; Berry and Dennis, 2007, 2012) for the cases where there are two or more phase singularities present in the wave field. In such cases, the behavior of the vortices becomes somewhat complicated, with possible phenomena including the creation, annihilation, and crossing of vortex lines. For the electron vortex, experimental demonstrations of wave fields with two (Hasegawa *et al.*, 2013) or several (Niermann, Verbeeck, and Lehmann, 2014) phase singularities have been realized in the electron microscope. In the first case, a specially prepared holographic mask with two phase defects (edge dislocations) was used to embed two phase singularities into the resulting first-order beams (Hasegawa *et al.*, 2013), while the second involved two orthogonally acting biprisms arranged in such a manner as to generate a lattice of vortices through wave interference.

For the case when two vortices are present in the beam, the behavior and interaction of the two vortices can be examined as the beam passes through focus. Holographic masks incorporating two edge defects were produced to generate two vortices of topological change $|l| = 1$ slightly displaced from one another—the two vortices may be either aligned or antialigned, in which case the behavior as they propagate takes on a different character. For the case when the two vortices are aligned, they are found to precess about each other within the first-order diffracted beams, whereas for the case when the vortices are antialigned the lines of phase singularity are attracted to each other, eventually annihilating. Both effects are attributed to the change in the Gouy phase as the vortices pass through the focal point (Hasegawa *et al.*, 2013). For the aligned beams the Gouy phase shift occurs in the same direction, so that the beam rotates in the same direction at

the same rate, whereas the phase shift is opposite for the antialigned vortices, causing them to annihilate.

E. Factors affecting the size of the vortex beam

The possibility of using electron vortex beams to probe the properties of materials with atomic resolution requires the generation of atomic scale vortex beams with cross sections in the Å scale. Sub-Å focused electron probes have been demonstrated and available for more than a decade (Batson, Dellby, and Krivanek, 2002). In a modern transmission electron microscope, a probe size as small as 0.5 Å can be achieved using a highly coherent source with a large convergence angle and corrective optics for the minimizing of aberrations in the probe forming lens (Erni *et al.*, 2009). Can we replace the circular aperture with a top-hat-like transmission function with an azimuthal phase gradient to produce an electron vortex beam, such as the beam defined in Sec. II.B.3, in the Å range? To answer this question, we need to first define what is meant by the size of nonvortex beams as well as that of vortex beams.

A simple estimate of the ring size of the single donut vortex beam can be obtained by considering the quantized orbital angular momentum of a circulating particle flux in a circle of radius ρ_l. We make use of the standard expression for the angular momentum $\mathbf{L} = \boldsymbol{\rho}_l \times \mathbf{p}$ and that the maximum size of the linear momentum transferred by the diffraction of electron beams passing through an aperture subtending a half angle α is equal to αk_0, where $\hbar k_0$ is the momentum of the electrons. The size of the donut ring is then given by

$$\rho_l \sim \frac{l\hbar}{\alpha\hbar k_0} = \frac{l\lambda}{2\pi\alpha}. \tag{93}$$

For all the beams passing through such an aperture, the uncertainty principle also implies that the minimum beam size ($\Delta\rho$) due to diffractive broadening is given by

$$\Delta\rho \sim \frac{\hbar}{\Delta p} = \frac{\hbar}{\alpha\hbar k_0} \sim \frac{\lambda}{2\pi\alpha}. \tag{94}$$

These order-of-magnitude estimates show that both ρ_l and $\Delta\rho$ are controlled by the convergence angle subtended by the lens aperture ($\alpha = R_{\max}/f$) but for different physical reasons. To be more precise, one needs to know the exact electron wave functions because the spatial distributions of the electrons are known to be diffuse in space and vary for different types of vortex beams as reviewed in Sec. II.B. For example, the size of the donut rings (ρ_l) in LG beams introduced in Sec. II.B.1 scales with $\sqrt{l}$ (Lembessis and Babiker, 2016), but for bandwidth-limited vortex beams produced by the Fraunhofer diffraction of a finite-radius plane waves impinging on a spiral phase plate (Sec. II.B.3), the ring size scales with l (Curtis and Grier, 2003). For the FT-TBB discussed in Sec. II.B.3, there is a nonlinear dependence on l. On the other hand, the diffraction-limited width of an ideal nonvortex beam is given by the size of the Airy disk [$\Delta\rho = 1.22\lambda/\alpha$ (Airy, 1834)]. Combining the two different effects an approximate empirical formula for the overall vortex beam size ($\tilde{\rho}_l$) emerges as (Curtis and Grier, 2003)

$$\tilde{\rho}_l = 2.585\frac{\lambda f}{\pi R_{\max}}\left(1 + \frac{l}{9.80}\right). \tag{95}$$

This suggests that the diffraction-limited singly charged vortex beam size is only about 10% larger than the nonvortex beam. With a microscope capable of a 0.5 Å nonvortex beam, a singly charged vortex beam of sub-Å size should be possible.

Experimentally, most studied electron vortex beams can be effectively obtained as some forms of bandwidth-limited beams with wave function truncation by a hard aperture at the plane of the focusing lens (Verbeeck *et al.*, 2011; Schattschneider *et al.*, 2012; Béché, Juchtmans, and Verbeeck, 2017). The scalar diffraction theory of such a case was thoroughly investigated in the course of optical vortex studies (Kotlyar *et al.*, 2005) and this compares favorably with the theoretical investigations when finite source size effects or even spherical aberration is taken into account, where appropriate (Schattschneider *et al.*, 2012). In situations where a small convergent beam is used (Verbeeck *et al.*, 2011; Schattschneider *et al.*, 2012), the ring diameter of the vortex beam can be accurately measured and the experimentally obtained values agree with those emerging from optical diffraction theory. For example, in a TEM with a round condenser aperture subtending a convergence angle of 21 mrad, the size of the Airy pattern of the nonvortex beam is 1 Å using the Rayleigh resolution criterion for the case of an electron vortex beam with $l = 1$ and a minimum full width at half maximum (FWHM) diameter of 1.2 Å. The reason that it is the FWHM that is used in this case instead of the ring size is the broadening effect of the spatial distribution due to the finite source size (incoherent broadening), estimated at 0.7 Å. Incoherent broadening effects, when these are significant, result in a less visible central dip of the vortex beam (for an example, see Fig. 17). Incoherent broadening plays an increasingly important role in atomic size electron vortex beam experiments as a size-limiting factor (Löfgren *et al.*, 2016), but its influence can be taken into account in the same manner as done routinely in describing focused nonvortex beams commonly used in scanning transmission electron microscopy (Kirkland, 2010). For an electron vortex beam generated inside a 300 kV scanning transmission electron

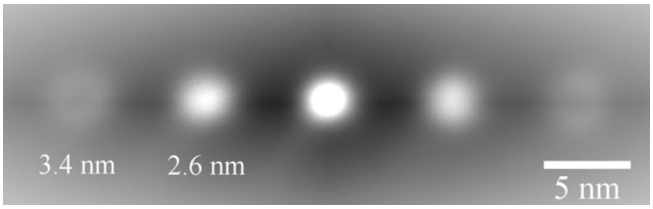

FIG. 17. Vortex probes at focus of the condenser lens of a JEOL 2200FS aberration-corrected tranmission electron microscope operating at 200 kV. The central spot is the image of the nonvortex beam, while the other spots are images of the diffracted vortex beams produced by a forked diffractive hologram with a binary pattern similar to that given in Fig. 12. Sizes of the first and second vortex cores at FWHM are 3.4 and 2.6 nm, respectively. Because of the incoherent effect, the intensity dip is only partially visible for the second-order vortex beam.

microscope a probe size of the order of 0.87 Å has been demonstrated (Béché, Juchtmans, and Verbeeck, 2017), invalidating the early too pessimistic prediction (Idrobo and Pennycook, 2011). As the current resolution of electron microscopes is not yet wavelength limited, there is still scope to reduce the vortex beam size further.

VI. INTERACTION WITH MATTER

The interaction of an electron vortex beam with single atoms was considered (Lloyd, Babiker, and Yuan, 2012a, 2012b; Yuan, Lloyd, and Babiker, 2013; van Boxem, Partoens, and Verbeeck, 2014, 2015), as well as Mott scattering (Serbo *et al.*, 2015) when the spin-orbit interaction is taken into account. The related radiative capture of a vortex electron by an ion was also investigated (Matula *et al.*, 2014). We focus on chiral-specific interactions in this section.

A. Chiral-specific spectroscopy

The practical generation of electron vortex beams was accompanied by the suggestion that such vortex probes might initiate, as a first application, a new type of EELS involving orbital angular momentum transfer (Uchida and Tonomura, 2010; Verbeeck, Tian, and Schattschneider, 2010; McMorran *et al.*, 2011). The first experiment on EELS using electron vortex beams was reported by Verbeeck, Tian, and Schattschneider (2010). In this experiment, a 50 nm thick Fe film was placed inside the field of the objective lens such that it was magnetically saturated. A nonvortex beam was transmitted through the iron film and the transmitted beam then passed through a forked holographic mask at a slight defocus such that the various orbital angular momentum components were separated into distinct vortex beams. Comparing the energy-loss spectra of the two first-order transmitted vortex beams showed a dichroic effect in the iron L_2 and L_3 edges, understood to indicate a transfer of orbital angular momentum between the beam and the internal electronic states of the iron atoms. The electron vortex energy-loss spectrum corresponds well to similar x-ray magnetic circular dichroism (XMCD) spectra (Thole *et al.*, 1992; Carra *et al.*, 1993), so that the magnetization of the sample is said to be clearly identified. However, since this 2010 result was reported there have been no further experimental reports of an observed magnetic dichroism, and there has been much discussion as to whether electron vortex beams could provide an advantage over existing methods in electron beam chiral dichroism spectroscopy. Nevertheless, a great deal of theoretical work has been carried out, uncovering the subtle physics involving orbital angular momentum transfer and the best conditions for its observation (Rusz and Bhowmick, 2013; Yuan, Lloyd, and Babiker, 2013; Schattschneider, Löffler *et al.*, 2014).

Comparing the results of the iron dichroism experiment with the well-known XMCD spectra of iron suggests that there is a similar transfer of orbital angular momentum between the beam electron and the internal atomic states, in contrast to the case of optical vortices, in which no orbital angular momentum transfer can arise in dipole transition (Babiker *et al.*, 2002; Andrews, Dávila Romero, and Babiker, 2004; Jáuregui, 2004) [see also Alexandrescu, Di Fabrizio, and Cojoc (2005)] nor were any observed (Araoka *et al.*, 2005; Löffler, Broer, and Woerdman, 2011; Giammanco *et al.*, 2017). The mechanisms of the atomic-vortex interactions are quite different in the optics and electron cases. In the optics case the interaction Hamiltonian arising from the minimal coupling prescription does not exhibit the required chirality to mediate orbital angular momentum transfer, in contrast to the long-range Coulomb interaction between the atomic and vortex electrons (Lloyd, Babiker, and Yuan, 2012a, 2012b).

1. Matrix elements for OAM transfer

Writing the interaction Hamiltonian as the sum of the Coulomb interactions between the atomic constituents and the vortex electron, we have

$$\mathcal{H}_{\rm int} = -\frac{e^2}{4\pi\epsilon_0}\left(\frac{1}{|\mathbf{r}_v - \mathbf{R} + (m_e/M)\mathbf{q}|} - \frac{1}{|\mathbf{r}_v - \mathbf{R} + (m_p/M)\mathbf{q}|}\right), \tag{96}$$

where $M = m_p + m_e$ is the mass of the atom, and the relevant position vectors are shown in Fig. 18. This interaction Hamiltonian may now be expanded as a multipolar series and applied as a scattering perturbation to a set of initial and final states of the well-known hydrogenic wave functions and vortex wave functions to yield the selection rules of the

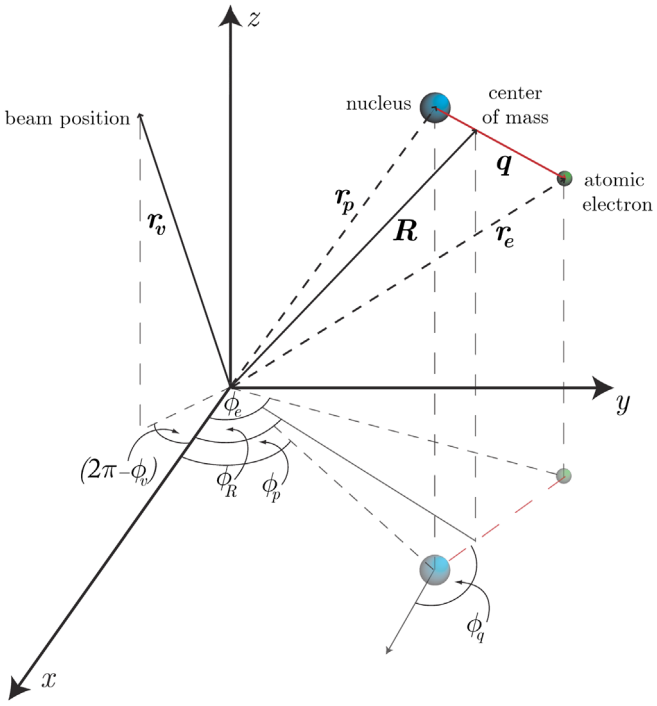

FIG. 18. The atomic model system interacting with a vortex beam whose cylindrical axis is along the z direction of the laboratory frame of reference. The vectors $\mathbf{r}_e, \mathbf{r}_p, \mathbf{R}$, $\mathbf{q}$, and $\mathbf{r}_v$ refer, respectively, to the position vectors of the atomic electron, the nucleus, the center of mass, the internal position relative to the center of mass, and the position variable of the vortex electron. The corresponding ϕ's represent the azimuthal angles and these are important for the description of the phase factors.

interaction (Lloyd, Babiker, and Yuan, 2012a, 2012b). In the leading (dipole) order the transition matrix element is found to reduce to

$$\mathcal{M}_{fi} = \frac{e^2}{4\pi\epsilon_0}(\mathcal{C}_l^{+1}\delta_{[(L+l),(L'+l'+1)]}\delta_{m,m'-1} + \mathcal{C}_l^{-1}\delta_{[(L+l),(L'+l'-1)]}\delta_{m,m'+1} + \mathcal{C}_l^{0}\delta_{[(L+l),(L'+l')]}\delta_{m,m'}), \tag{97}$$

where the C_l's are complex functions of the internal coordinate $\mathbf{q}$ to the first order. The selection rules deducible from the matrix element show that in the dipole approximation a single unit of orbital angular momentum may be absorbed (released) by the atomic electron from (to) the combined orbital angular momentum of the electron vortex and atomic center of mass. The combination of the vortex and center of mass orbital angular momenta allows for the possibility of the rotation of the center of mass, provided the atom is not fixed, which lays the foundations for the manipulation of larger particles though OAM exchange (Gnanavel, Yuan, and Babiker, 2012; Verbeeck, Tian, and Tendeloo, 2013). Further analysis of the quadrupole and higher order interaction terms demonstrates similar selection rules in which zero, one, or two units of orbital angular momentum may be transferred; higher order multipole terms of order n mediate the transfer of zero or n units of orbital angular momentum.

2. The effect of off-axis vortex beam excitation

In expanding the interaction Hamiltonian about the atomic center of mass, this analysis does not fully demonstrate the complications arising from the extrinsic nature of the vortex orbital angular momentum. It is illuminating to determine the modal expansion of an off-axis beam from the perspective of the atomic nucleus and compute the weighted scattering amplitudes to the various possible transfer channels. The interaction Hamiltonian remains the same as that of Eq. (96), but now the initial and final vortex states have to be written as expansions about the center of mass frame, rather than being given in the laboratory frame, as before. This is accomplished by use of the Bessel function addition theorem (Abramowitz and Stegun, 1972) (see Fig. 18 for the relevant notation)

$$J_l(k_\perp) = e^{-il(\phi_v-\phi_n)} \times \sum_{p=-\infty}^{\infty} J_{l-p}(k_\perp\rho_n)J_p(k_\perp\rho_v')e^{i(l-p)\phi_n}e^{ip\phi_v'}. \tag{98}$$

This results in the original vortex beam of topological charge l being described with respect to a new axis, the origin of which is common with the atomic nucleus, in terms of an infinite series of Bessel functions $J_p(k_\perp\rho_v')$, with weighting functions given by $J_{l+p}(k_\perp\rho_n)$. Thus, the relative location of the atom with respect to the axis of the incident vortex beam determines the precise modes that the atomic electron "sees" to interact with. For an atom situated directly on the beam axis, the original $p = l$ mode is the only contribution, since in this case only the weighting term $J_0(k_\perp\rho_n)$ is nonzero (see also Fig. 19, left panel). However, for an atom displaced from the beam axis, the next atom- centered vortex modes $p = l \pm 1$ become significant even at small distances, of the order of a fraction of the radius corresponding to the first Bessel function zero $\lambda_{11}/k_\perp \approx 0.1$ nm for $l = 1$, i.e., within the first ring of the Bessel beam. It is clear that slight displacement from the beam axis leads to the contributions of vortex modes with winding numbers different from the overall angular momentum quantum number of the beam l (see also Fig. 19, right panel). The expanded Bessel function may then be used to define an effective operator

$$\mathcal{O} = \langle\Psi_f'|\mathcal{H}_{\rm int}|\Psi_i'\rangle \tag{99}$$

which determines the selection rules when applied to the atomic states, where $\Psi'_{i(f)}$ refers to the initial (final) wave function involving the expanded Bessel function of Eq. (98). Applying the Bessel addition theorem a second time allows for the expansion in terms of the in-plane dipole moment of the atom, making apparent the specific multipolar character of the transfer interaction (Yuan, Lloyd, and Babiker, 2013).

When the atom is off axis, there are several available channels for atomic excitation, in view of both the multipolar nature and the specific Bessel mode of the expansion, as illustrated in Fig. 19. It can be seen that, in contrast to the straightforward on-axis case, for an atom localized at an off-axis position the change in the orbital angular momentum of the beam does not necessarily indicate a corresponding change in the OAM of the internal dynamics of the atom. At

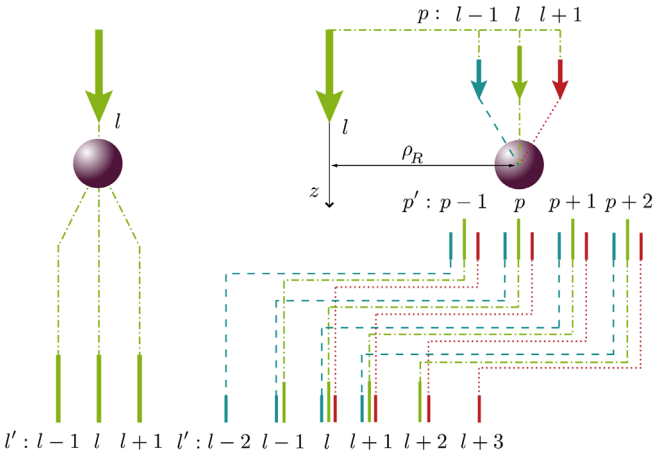

FIG. 19. Illustration of the various interaction channels available in (a) the case in which the atom is situated on axis, and (b) the off-axis case. In (a), any change in OAM of the atomic electron is immediately apparent as a change in OAM of the transmitted beam $\Delta l = l' - l$. The case in (b) is more complicated due to the expansion modes having various OAM p, which may each transfer any number of units of OAM to the atomic electron. The resulting changes Δl values may correspond to a variety of combinations of expansion modes and multipolar transitions, as shown. However, due to the relative strengths of the expansion modes and multipolar atomic transitions, the dominant interaction channels arise from the dipole interaction with the $p = l$ mode. Note that p is used here only to indicate the OAM modes involved in an off-axis vortex beam, not as a radial index as in the rest of the text. From Yuan, Lloyd, and Babiker, 2013.

first sight this would seem to present a large obstacle to the use of vortex beams to probe chiral information. However, after taking into account the relative intensities of the various interaction channels, one can show that for the dipole excitation case the off-axis contributions are an order of magnitude smaller than the on-axis contribution, with intensity decaying rapidly farther away from the axis, so that the principal transitions in any such chiral spectroscopy experiment are those having the XMCD-like selection rules of Eq. (97). Additionally, higher order multipole transitions will contribute to the background signal, but these are also found to be much smaller in magnitude compared to the dipole contribution, due to the much smaller overlap of the Bessel functions involved (Yuan, Lloyd, and Babiker, 2013).

The off-axis contributions to an experimental electron-energy loss spectrum may be further reduced to produce an acceptable signal-to-noise ratio, by making use of a confocal TEM setup, ensuring that the signal contributions come from those atoms lying on or very close to the microscope axis and reducing the nonchiral signal from atoms displaced from the axis (Schattschneider, Löffler *et al.*, 2014). As pointed out, interactions in these regions are most likely to involve the $p = l$ modes, and thus the change in orbital angular momentum of the vortex in the laboratory frame is indicative of the atomic change in magnetic quantum number. A schematic of such an experiment is shown in Fig. 20. A vortex beam is incident on a sample, with the resulting transmitted beam split into the various orbital angular momentum components by a OAM analyzer. After passing through the sample, the transmitted beam contains several different OAM components l' from the various interactions, along with the original value l from electrons passing through unscattered. Analysis of the various OAM components allowed the determination of the change in the OAM of the atom. It was shown that a suitable analyzer may take the form of a forked holographic mask in conjunction with a pinhole (Saitoh *et al.*, 2013). The pinhole will enable the isolation of specific OAM components for measurement of EELS spectra for that channel, allowing detection of only those transmitted electrons having $l' = 0$, for example, those that have suffered a loss (gain) of one unit of orbital angular momentum in the interaction with an $l = +1$ (-1) incident vortex. The pinhole acts to select only those transitions that have both $p = l$ contributions and that are scattered to $l' = p' = 0$ states. Repeating the experiment using a vortex beam of opposite OAM, i.e., $-l$ will enable a dichroism spectrum to be obtained.

The advantage of this method over the experiment demonstrated by Verbeeck, Tian, and Schattschneider (2010) should be an increase in signal-to-noise ratio, since the forward and reverse interactions are treated separately (the additional off-axis features and higher-multipole excitations also contribute to a background noise with a nonvortex incident beam). In this way, probing specific atomic transitions is feasible with varying incident vortices, including higher order multipole transitions using incident vortices with orbital angular momentum greater than $\pm\hbar$. On the other hand, since the transmitted intensities in these cases are expected to be small, the experimental conditions must be optimized so that long collection times may be utilized. An

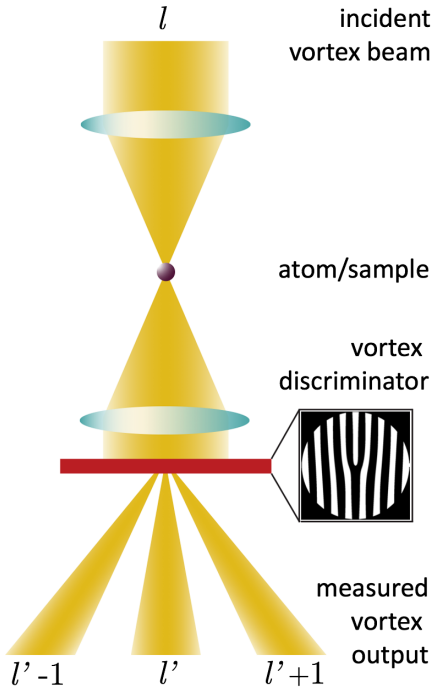

FIG. 20. Schematic of suggested experimental setup for OAM based spectroscopy using electron vortices. A vortex beam produced by a holographic mask or other suitable method (not shown) is incident onto a thin sample in the specimen plane. After interaction with the sample, the transmitted beam is then passed through a forked mask in order to separate the various vortex components. A pinhole placed in the diffraction plane allows isolation of those modes that have an OAM of 0 after passing though the mask; these can then be detected to obtain EELS.

experimental feasibility study is encouraging (Schachinger *et al.*, 2017), especially for amorphous magnetic materials.

Since they were first reported, it was suggested that electron vortex beams may be combined with the atomic resolution microscope probes to enable chiral spectroscopy with atomic resolution (Verbeeck, Tian, and Schattschneider, 2010; Idrobo and Pennycook, 2011; Verbeeck *et al.*, 2011; Lloyd, Babiker, and Yuan, 2012b; Rusz and Bhowmick, 2013; Yuan, Lloyd, and Babiker, 2013). However, there is currently some debate as to the conditions under which such high resolution will be achievable and the limits of application of the vortex beam (Pohl *et al.*, 2015). Specifically, are the subnanometer scale vortex beams described by Verbeeck *et al.* (2011) suitable for atomic resolution dichroism experiments? It was argued that the subnanometer FWHM of such beams is not sufficient due to the inherent incoherence in the microscope. On the other hand, it was also argued that it is only in the atomic resolution limit that vortex chiral dichroism experiments will give any improvement over the intrinsic electron magnetic circular dichroism (EMCD) effect due to the crystal structure acting to diffract the vortex modes (Rusz and Bhowmick, 2013). Simulations of inelastic scattering of vortex beams through iron crystals up to 20 nm thick shows that magnetic information is available only when the radius of the vortex beam is of the order of the atomic radius. In this case, the energy filtered diffraction signal shows a magnetic component of approximately 10% of the background, nonmagnetic signal and is strongly dependent on the position of

incidence within the unit cell, so displaying atomic resolution (Rusz and Bhowmick, 2013).

The inelastic scattering of an electron vortex beam by atoms was also further investigated for hydrogen by van Boxem, Partoens, and Verbeeck (2015), by including the explicit radial distribution functions.

3. Plasmon spectroscopy

In addition to the research into chiral excitation of core electron transitions which is relevant to the excitation of magnetic sublevels in the inner shell of the atoms, Asenjo-Garcia and García de Abajo (2014) calculated the chiral plasmon response which is due to the coupling of the charges in the vortex beam with the electric field of the collective motion of the valence electrons.

The application of vortex beams to EELS may also have potential in mapping the magnetic response of materials in the form of magnetic plasmon resonances (Mohammadi *et al.*, 2012). Magnetic plasmon resonances in nanoparticle arrays are expected to lead to the production of metamaterials, exhibiting negative permittivity and permeability in the optical range (Podolskiy, Sarychev, and Shalaev, 2002; Sarychev, Shvets, and Shalaev, 2006), such that vortex based magnetic plasmon EELS (vortex-EELS) would provide an invaluable tool for the characterization of metamaterial response. EELS is already well applied in the determination of electric plasmon resonances of nanoparticles (Bosman *et al.*, 2007; Nelayah *et al.*, 2007; Hörl, Trügler, and Hohenester, 2013). Vortex-EELS should provide a complementary technique, with the additional possibility of gathering information on both the electric and magnetic responses of nanoparticles simultaneously in a single experiment, since the electron vortex will also induce electron plasmon resonances in addition to magnetic plasmon resonances.

A theoretical treatment of the magnetic response of an array of split-ring resonators was demonstrated (Mohammadi *et al.*, 2012), allowing direct comparison of the electric and magnetic plasmon resonance spectra and spatial distribution. Making use of the duality of the electric and magnetic fields allows the relationships between the induced resonance field and the beam current (related by Green's functions) to be recast into an induced magnetic field, regulated by a magnetic Green's function and induced by the effective magnetic current of the vortex beam (Mohammadi *et al.*, 2012). From here, the magnetic EELS spectra can be calculated using standard finite-difference time-domain techniques. For a split-ring resonator the results of such simulations show a strong magnetic response on the inside of the ring, contrasting with the electric response at the ends of the arms, as shown in Fig. 21. The calculated spatial profiles are consistent with previous theoretical work on electric and magnetic resonances of nanoparticles of similar sizes and shapes (Enkrich *et al.*, 2005; Sarychev, Shvets, and Shalaev, 2006). Critically, the intensity of the magnetic response is within an order of magnitude of the electric response, indicating that measurement of magnetic plasmon resonances should be experimentally accessible (Mohammadi *et al.*, 2012). Naturally, in an experimental situation, the vortex beam will induce electric plasmon resonances at the same time as the magnetic resonances, which for metamaterial development will necessarily be within similar energy ranges, notably within the visible light spectrum. Energy filtering is therefore insufficient to fully isolate the magnetic component of the EELS spectrum. For nanostructures for which the electric response is well understood, separating the magnetic signal may be possible by subtracting a separately measured non-vortex-EELS signal from the vortex-EELS map, or by filtering the transmitted signal by its OAM content (Mohammadi *et al.*, 2012). This latter method requires further investigation into the role of orbital angular momentum transfer in magnetic resonances, as it is not immediately apparent that OAM transfer is a requirement for vortex-induced magnetic plasmon resonance.

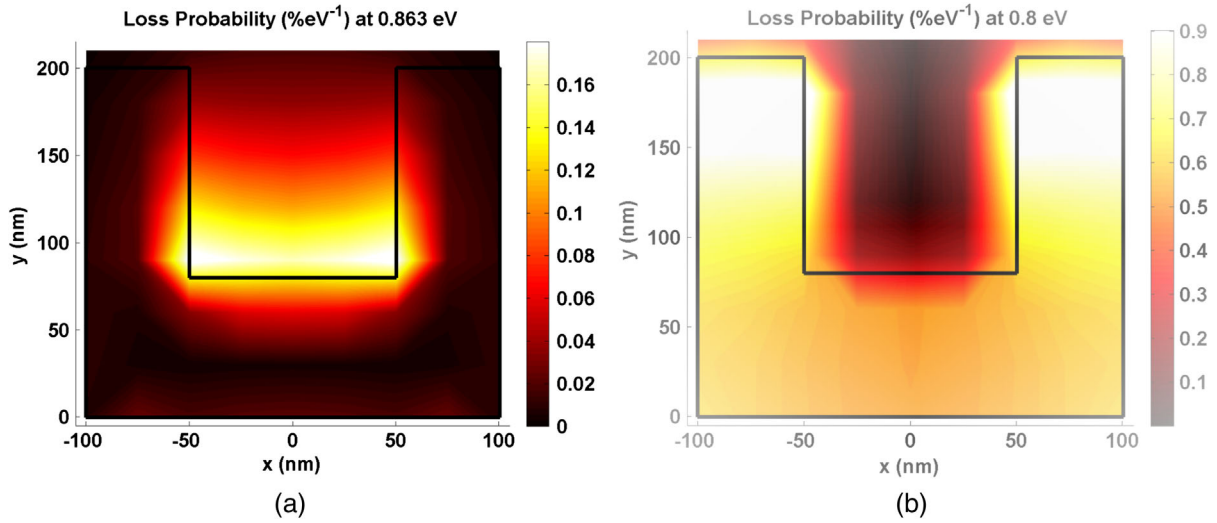

FIG. 21. Spatial maps of electron-energy-loss probability for (a) magnetic resonance at 0.863 eV, with an $l = 1$ beam, and (b) electric resonance at 0.8 eV with a plane wave beam, both at 100 keV beam energy. The two plasmon resonance maps show markedly different spatial profiles, as well as the magnetic resonance response being approximately an order of magnitude less than the electric response. From Mohammadi *et al.*, 2012.

B. Propagation in crystalline materials

In order that experiments involving vortex beams traveling in real materials to be appropriately interpreted, it is necessary that the way such a beam propagates through crystalline structures is well understood. Any electron probe propagating through a crystal will experience strong elastic scattering from Coulomb interaction with the atomic nuclei, proportional to the thickness of the sample and tilt relative to the beam axis, as well as channeling along the atomic columns (Reimer and Kohl, 2008; Williams and Barry Carter, 2009). Because of this scattering potential, the trajectory of the vortex and the local orbital angular momentum density of the beam will be altered, since the crystal potential breaks the cylindrical symmetry of the beam, leading to coherent superposition of OAM eigenstates that change in composition through the crystal (Löffler, Aiello, and Woerdman, 2012). Because of the exchange of orbital angular momentum between the lattice and the beam the local values of orbital angular momentum within the crystal may be quite different from those of the original, incident vortex beam (Löffler, Aiello, and Woerdman, 2012; Lubk, Clark *et al.*, 2013; Lubk, Guzzinati *et al.*, 2013). Additionally the trajectories of the vortex lines are no longer simple, involving oscillatory motions, looping, and the generation of vortex-antivortex pairs (Lubk, Clark *et al.*, 2013; Lubk, Guzzinati *et al.*, 2013). It is worth mentioning that the vortex structure can also be produced by dynamical scattering of crystals by a nonvortex incident electron beam (Allen *et al.*, 2001) because of multiple scattering (Nye and Berry, 1974).

Multislice simulations of the propagation of vortex beams through iron (Löffler, Aiello, and Woerdman, 2012) and strontium titanate (Lubk, Clark *et al.*, 2013) crystals have been carried out to explore the complex dynamics arising from the interaction. Both the Fe and $SrTiO_3$ materials are relevant since Fe is a simple and widely available material and is of specific interest in understanding the chiral spectroscopy EELS results reported by Verbeeck, Tian, and Schattschneider (2010), while the more complex $SrTiO_3$ crystal consists of atomic species of varying mass, allowing for more complex dynamics. In both cases, investigations of the phase and amplitude of the wave function within the crystal demonstrate that the resulting exit wave strongly depends not only on the thickness of the crystal, but also on the position of the incident beam in the unit cell, as well as the topological charge of the vortex.

For an incident vortex beam with $l = 1$ the expectation value of the orbital angular momentum within the iron crystal is found to oscillate with propagation and may take values significantly different to the original, including noninteger values and even reversing in sign (Löffler, Aiello, and Woerdman, 2012). For the $SrTiO_3$ crystal, the vortex is found to strongly channel along the atomic columns and is protected from delocalization compared to a nonvortex beam, remaining in an approximate angular momentum eigenstate within a certain radius, beyond which the wave function exhibits Rankine-like vortex behavior (Swartzlander and Hernandez-Aranda, 2007; Lubk, Clark *et al.*, 2013). Additionally, vortex-antivortex loops are spontaneously generated about the surrounding atomic columns. They manifest themselves as vortex-antivortex pairs in the x-y plane as the vortex forming the loop propagates in the z direction and then turns back on itself (Lubk, Clark *et al.*, 2013). When the vortex beam is incident off center on an atomic column the core of the vortex is found to circulate around the atomic column, while the center of mass line remains stationary.

For higher order vortex beams with $l > 1$ interesting dynamics arise that are dependent on the specific symmetry considerations about the point of incidence. The $l > 1$ vortex beam splits into a number of vortex beams of various orders, the specific order and arrangement of which depend on the specific symmetry. As a result, the local values of orbital angular momentum have a complicated dependence on the strength of the incident vortex state and the specific symmetry of the material as well as the propagation length and position within the unit cell. This is related to the extrinsic nature of the orbital angular momentum as discussed (see Sec. VI.A.2) and indicates that atoms at different positions within the sample will be subject to modes with vastly different orbital angular momenta. This introduces complications in, for example, electron-energy-loss spectroscopy as the atoms within the sample interact with vortices of various strengths. For relatively thick samples then, particular care must be taken in analysis requiring direct observation of phase and intensity contrast; however, filtering the separated scattered vortex states will go some way to ameliorating the phase complications.

It was shown that an electron vortex beam can propagate through atomic columns to a considerable distance by coupling to the $2p$ columnar orbital with the same angular momentum about the propagation axis. This shows that the divergence of the electron vortex beam can be counteracted by interacting with an atomic column (Xin and Zheng, 2012). The interaction of an electron vortex beam with an atomic column was also studied by Xie, Wang, and Pan (2014).

One application of electron vortex beams to crystalline materials is in the determination of the chirality of enantiomorphic crystals through diffraction pattern analysis (Juchtmans *et al.*, 2015; Juchtmans, Guzzinati, and Verbeeck, 2016). The other predicted application of the electron vortex beam is to make use of the interplay between the elastic and inelastic scattering to determine the magnetic dichroism spectroscopy (Rusz and Bhowmick, 2013; Rusz *et al.*, 2014). Here, as discussed earlier, the small size of the electron vortex beam is important in highlighting the advantage of using electron vortex beams over conventional nonvortex beams.

C. Mechanical transfer of orbital angular momentum

The electron vortex beam carries both linear momentum and orbital angular momentum of $\hbar k_z$ and $\hbar l$, respectively, each along the axial direction. As for optical vortices, the total linear and angular momentum of the electron vortex beam have components which are nonzero only in the axial direction, while both the linear and angular momentum density vectors [defined in Eqs. (27) and (31)] have additional components in the radial and azimuthal directions (Lloyd, Babiker, and Yuan, 2013; Speirits and Barnett, 2013). These local densities contribute to the diffractive effects within the beam, and the azimuthal momentum density provides the requisite angular motion contributing to the total angular momentum; however, components of the total orbital angular momentum do not exist neither radially nor azimuthally.

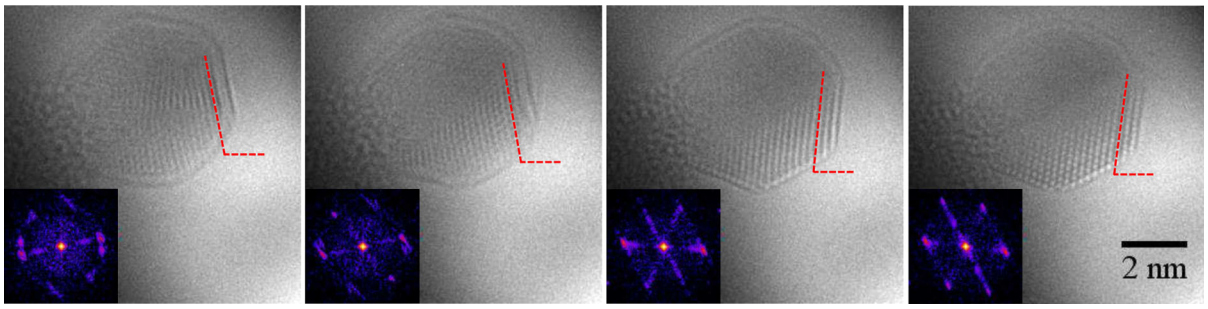

FIG. 22. Four snapshots of Au nanoparticles rotated by second-order vortex beams selected from a video at 1.2 s intervals. The center dark core surrounded by the bright ring of the first-order vortex beams is partially visible at the bottom right corner. The angles of lattice fringes correspond to 99.5°, 99.0°, 87.0°, and 84.5°, respectively. The insets show the corresponding fast Fourier transform.

For the electron vortex, in addition to the mechanical momentum due to the electron mass current, the electric and magnetic fields may also contribute to the total beam momentum and angular momentum. As with mechanical momenta, the contributions to the total linear and angular momentum vectors are found to exist only in the axial directions, despite the field momentum densities having additional radial and azimuthal components (Lloyd, Babiker, and Yuan, 2013). The contributions from the electric and magnetic fields of the electron vortex beam are small; for the typical beam generated within an electron microscope, the linear and angular momentum contributions due to the electromagnetic fields are approximately 10^{-12} and 10^{-14} that of the mechanical momenta, respectively.

As in the case of optical vortices being used to trap and rotate objects from atoms to particles of micron size (He *et al.*, 1995; Barreiro and Tabosa, 2003; Andersen *et al.*, 2006; Franke-Arnold, Allen, and Padgett, 2008; Ruffner and Grier, 2012; Emile *et al.*, 2014), the influence of an electron vortex beam has been shown to induce rotation in nanoparticles (Gnanavel, Yuan, and Babiker, 2012; Verbeeck, Tian, and Tendeloo, 2013). Using the forked holographic mask technique to generate electron vortex beams within a JEOL 2200FS double aberration-corrected scanning transmission electron microscope operated at 200 keV, gold nanoparticles on carbon support were observed to rotate under the influence of the vortex beams (Gnanavel, Yuan, and Babiker, 2012). The nanometer scale vortex beams produced are shown in the focal plane in Fig. 17, having FWHM of 2.6 and 3.4 nm, respectively, for the first- and second-order beams. No central nodes are observed in the first-order beams due to partial coherence effects. In order to minimize these effects, the experiment was performed at a slight defocus such that the beam profile fully covers the 5 nm diameter gold nanoparticle.

The effects of the vortex beam on the nanoparticle were observed using a video capture, with a rate of 0.83 frames per second. Initially, the structural changes, translation, and rotation of the particle are minimal; however, it was found that after approximately 5 minutes of illumination significant damage had occurred to the carbon substrate with the particle essentially detached and having also undergone some structural damage. At this point, the particle is relatively free of the van der Waals interaction and effects due to viscous trapping potentials, and rotation is observed to occur at an average rate of 3.75° per minute, significantly faster than previous reports involving beams with no orbital angular momentum. Selected frames indicating the nanoparticle rotation are shown in Fig. 22. Although the precise mechanism of the rotation is rather complicated, the existence of the azimuthal component of the linear momentum density is necessary to effect rotation about the beam axis. This rotation is shown to occur due to the vortex nature of the beam by the relatively high rotation rate, and the change of the direction of rotation when the particle is illuminated with a similar beam carrying an opposite OAM (Gnanavel, Yuan, and Babiker, 2012). A similar rotation of gold nanoparticles was observed on silicon nitride support (Verbeeck, Tian, and Tendeloo, 2013).

It was proposed that the angular momentum transfer between the beam and the particle leading to rotation arises due to the breaking of the cylindrical symmetry of the beam (Verbeeck, Tian, and Tendeloo, 2013) by the particle. The exact mechanism of orbital angular momentum transfer between the beam and the nanoparticle depends on a number of variables, notably the relative size of the nanoparticle and the beam, as well as the material properties of the particle, which affect the beam scattering dynamics within the crystal potential, in addition to the experimental parameters (Verbeeck, Tian, and Tendeloo, 2013). Furthermore, the requirement that the sample support be damaged before any rotation is observed suggests that friction between the nanoparticle and the support is the limiting factor in this case. Indeed, after prolonged illumination under the beam, the nanoparticle eventually becomes coated with carbon from the support and ceases to rotate.

This suggests that the electron vortex beam may become a useful tool in the investigation of friction at the nanoscale, which is still not well understood (Mo, Turner, and Szlufarska, 2009). Experiments involving the rotation of various species of nanoparticles on a range of supports may thus be considered useful in the characterization of nanoscale friction. Additionally, a friction-free control environment could be provided by rotation of particles while they are levitated by an optical beam (Lloyd, Babiker, and Yuan, 2013). Similar experiments may also be considered to explore viscous forces, for example, by using nanoparticles suspended in liquids in a liquid-cell sample holder. The electron vortex provides a method by which particles may be moved transverse to a surface, so that the friction between various surfaces and particles may be directly investigated; this transverse motion may also find application in nanomanipulation for various uses (Falvo and Superfine, 2000), including molecular biophysics applications (Bormuth *et al.*, 2009; Balzer *et al.*, 2013).

D. Polarization radiation

The magnetic moments associated with the orbital angular momentum of the electron vortex beam can be arbitrarily large, in principle, as the axial orbital angular momentum can be very large. The polarization radiation associated with the passing of a fast moving magnetic dipole moment can display some interesting effects not seen before (Ivanov and Karlovets, 2013a, 2013b; Konkov, Potylitsyn, and Polonskaya, 2014), such as the circular polarization of the emitting radiation. The challenge, however, is to be able to produce coherent vortex beams of high topological charges, not in the form of a distribution of a number of vortices of lower order topological charges (Freund, 1999; Ricci, Löffler, and van Exter, 2012).

VII. APPLICATIONS, CHALLENGES, AND CONCLUSIONS

We outlined the various methods currently used for the realization of electron vortices in the laboratory. We also emphasized the quantum nature of electron vortices as freely propagating de Broglie vortex waves endowed with the property of orbital angular momentum about their propagation axis, which also coincides with the vortex core. The intrinsic properties of electron vortices have been pointed out, specifically their mass and charge distributions and how these determine their momentum and orbital angular momentum contents, as well as their spin and its coupling to the orbital angular momentum. This is particularly illuminating in terms of revisiting some of the basics concepts involved. Progress in the study of their interaction with matter has been summarized, especially in connection with magnetic systems and the issue of transfer of orbital angular momentum to the internal dynamics of atomic systems. The possibility of using electron vortices to rotate nanoparticles and current experimental work on this has also been described.

The study of electron vortex beams and their interactions clearly benefits from the highly advanced state of electron optics used to produce high resolution electron microscopy, electron spectroscopy, and electron beam lithography. This sets electron beam technology apart from all other matter beam technologies, with the neutron, ion, and atom beams being the distant competitors. Currently it is much easier to generate electron vortex beams than other matter vortex beams. The down side of the existing electron optics technology is that they are bulky and, unlike optical systems, not easily reconfigurable because of the connected vacuum system essential for the free passage of the electron beams. This means that most of the existing vortex beam research has to be conducted within the existing electron microscopes designed with the science of advanced materials in mind and time shared with real-world applications as well. Nevertheless, where existing research facilities could be employed with little modification rapid progress has been made. In particular, this is evident in the development of electron vortex beam technology in electron microscopy and our understanding of its characteristics and there is some proof-of-principle demonstrations of its unique capabilities. Much more research is required to understand the intrinsic nature of some of its characteristics as well as the need for developing optimized setups for vortex beam experiments so that practical applications can be properly tested. Among the optimized setups to be realized would be an electron vortex beam source similar to that available for optical vortex beams (Cai *et al.*, 2012). This would be a useful alternative to the various beam conversion schemes that have been discovered so far. There is some encouraging experimental evidence for that (Schmidt *et al.*, 2014). The electron repulsion that would be expected in a high brightness (many-electron) beam needs to be taken into account. A feasibility study on the shape-preserving many-electron vortex beam design has been conducted by Mutzafi *et al.* (2014) and the result is promising, indicating that the generation of a high current electron vortex beam is possible.

It is probably too early to apply vortex beams routinely to study the physics of materials because, although the existing electron beam setups are optimized for electron microscopy, a number of electron vortex beam experiments have already led to applications to be realized in principle. This fact allows us to contemplate on what possible developments in the future might be.

As pointed out at the outset, more applications of electron vortex beams are expected to follow, in which the orbital angular momentum of the beam is expected to provide new information about crystallographic, electronic, and magnetic properties of the sample. Magnetic-dependent EELS has already been demonstrated, based on the principles of electron vortex beams, and it is predicted that the high resolution achievable in the electron microscope will lead to the ability to map magnetic information at atomic or near-atomic resolution. The determination of magnetic structure at the nanoscale has always placed a significant demand on electron microscopy. The linear and chiral dichroic spectroscopies (Yuan and Menon, 1997; Schattschneider *et al.*, 2006), based on non-vortex beams have been developed, with the linear dichroism being useful in the study of spin orientation in antiferromagnetic materials and the chiral dichroism for spin orientation in ferromagnetic materials. Electron vortex spectroscopy offers an alternative method to access chiral-dependent electronic excitations (Yuan, Lloyd, and Babiker, 2013).

The orbital angular momentum and magnetic properties of the electron vortex beams may also find potential uses in spintronic applications, either in the characterization of spintronic devices or in contexts employing spin-polarized current injection, through spin-to-orbital angular momentum conversion processes (Karimi *et al.*, 2012). The reverse process of the spin filter using spin-orbit coupling in electron Bessel beams was investigated theoretically (Schattschneider, Grillo, and Aubry, 2017).

Additionally, the inherent phase structure of the vortex is considered ideal for applications in high resolution phase contrast imaging, as required for biological specimens with low absorption contrast (Jesacher *et al.*, 2005) or in revealing local orbital angular momentum density (Juchtmans and Verbeeck, 2016).

Applications of electron vortex beams are, however, not restricted to spectroscopy and imaging. The orbital angular momentum of the beam may also be used for the manipulation of nanoparticles (Gnanavel, Yuan, and Babiker, 2012; Verbeeck, Tian, and Tendeloo, 2013) leading to electron spanners analogous to the widely used optical spanners. Electron vortex states are also relevant in the context of quantum information

processing and, in particular, low-energy electron vortex beams may potentially be used to impart angular momentum on Bose-Einstein condensates (Fetter, 2001).

It was also predicted that the large magnetic moments associated with electron vortex beams of higher orbital angular momentum can be used to produce novel polarization radiation when passing through materials (Ivanov and Karlovets, 2013a, 2013b). This has led to a drive to produce electron beams with very large topological charges (Grillo *et al.*, 2015).

Both the kinematic and dynamical diffraction of electron vortex beams by chiral crystals have been shown to be sensitive to the helicity of the vortex beam, suggesting a useful characterizing tool for the study of chiral crystals.

The study of an electron vortex beam with strong laser fields has also opened up the possibility of accelerating nonrelativistic twisted electrons using focused electromagnetic fields (Karlovets, 2012) or beam steering using the high electric fields due to an ultrashort pulsed beam (Hayrapetyan *et al.*, 2014; Bandyopadhyay, Basu, and Chowdhury, 2015). Research into laser-electron beam interaction also allows coherent optical vortex beams to be produced (Hemsing *et al.*, 2013). The inverse photoemission process involving an electron vortex beam is another interesting problem for further investigation (Matula *et al.*, 2014; Zaytsev, Serbo, and Shabaev, 2017).

In particle physics experiments, the use of vortex beams instead of approximate plane waves would permit a direct measurement to be made as to how the overall phase of the plane wave scattering amplitude changes with the scattering angle (Ivanov, 2012b; Ivanov *et al.*, 2016; Karlovets, 2016). This may be important for many high energy experiments in hadron physics. It is therefore highly desirable to introduce electron vortex beams into high energy particle accelerators.

Vortex beam-beam interactions also open up the possibility of the creation of two vortex-entangled beams, with implications for quantum information processing (Ivanov, 2012a, 2012b).

In conclusion, our review of the emergent area of electron vortex beams has indicated that much progress has already been made in a relatively short period of time, particularly over the last few years. The emphasis so far has been primarily on the fundamental aspects of the electron vortex beams. However, there are still many unexplored topics, ranging from novel vortex beams (Wang and Li, 2011) to image contrast enhancement and to exploring applications of vortex beams in quantum information processing, just to mention a few. The range and complexity of the phenomena involving electron vortex beams point to a brighter future for further developments in this field.

A. Recent papers

As a sign of growing interest in the vortex beam physics, interesting development was still continuing during the refereeing process of this review. In particular, we highlight the recent proposal to perform a measurement of the OAM content of an electron vortex beam (Larocque *et al.*, 2016) using the microscopic version of the magnetic braking experiment (Saslow, 1992; Donoso, Ladera, and Martín, 2009, 2011) or by weak measurement (Qiu, Ren, and Zhang, 2016), the possible detection of magnetic contrast in magnetic crystal using Zeeman effect (Edström, Lubk, and Rusz, 2016a; Edström, Lubk, and Rusz, 2016b) as well as the recent debate about the existence of vortex structure in relativistic electron beams (Barnett, 2017; Bialynicki-Birula and Bialynicka-Birula, 2017).

LIST OF SYMBOLS AND ABBREVIATIONS

$\mathbf{A}$	vector potential of externally applied axial magnetic field
α	convergence angle of a focused electron beam
$\bar{\alpha}$	parameter characterizing the magnetic correction to the effective vortex beam topological charge
D	effective length of the vortex beam
$\delta\phi$	rotation angle
$\delta_{l,s}$	spin-orbit energy
$\Delta\phi$	phase change
Δt	film thickness of phase masks for electron beams
$\mathcal{E}$	energy eigenvalue of the electron vortex beam
$\mathbf{E}$ and $\mathbf{B}$	electric and magnetic vector fields associated with the electron vortex beam
$F_{\mu\nu}$	electromagnetic field tensor
${}_pF_q$	generalized hypergeometric function
g_s	gyromagnetic ratio
$\Gamma(x)$	gamma function
$\mathcal{H}$	Hamiltonian
I	beam electric current
$\mathcal{I}^n$	nth moment integral of the Bessel function
$J_l(x)$	Bessel function of the first kind of order l
$\mathbf{j}(\mathbf{r},t)$	probability current density
$\mathbf{j}_m(\mathbf{r},t)$	mass current density, equivalent to inertia linear momentum density $\mathcal{P}_m$
$\mathbf{J}$	total angular momentum of the electron vortex beam
$\mathbf{k}$	wave vector of the electron wave.
κ	$\sqrt{1-m/E}$
k_z	axial wave number of the electron vortex beam
$k_\perp$	transverse wave number of the electron vortex beam
l	winding number, also referred to as topological charge or azimuthal index
I_{holo}	hologram intensity
$L_p^l(x)$	generalized Laguerre polynomial with azimuthal index l and radial index p
$\mathcal{L}_m$	inertial angular momentum density of the electron vortex beam

$\mathbf{L}_m$	inertial angular momentum of the electron vortex beam
$\mathcal{L}_{\text{em}}$	electromagnetic angular momentum density of the electron vortex beam
$\mathbf{L}_{\text{em}}$	global electromagnetic angular momentum of the electron vortex beam
L_z	axial component of the orbital angular momentum operator
$\lambda_{p,l}$	pth zeros of Bessel function of order l
$\lambda_{p,l}$	wavelength
$\mathcal{M}_{fi}$	matrix element of interaction Hamiltonian H_{int} between quantum states i and f
$n(\mathbf{r},t)$	probability density $(=\psi^*\psi)$
n_L	quantized Landau level index
n_{eff}	effective refractive index
n	order of diffraction order
N_l	normalization constant for Bessel beam wave function of the order of l
ω_L	Larmor frequency
ω_c	cyclotron frequency
ω	angular frequency of the vortex beam
Ω	angular frequency of nanoparticles
$\mathcal{P}_m$	inertia linear momentum density of the electron vortex beam
$\mathbf{P}_m$	global inertia linear momentum of the electron vortex beam
$\mathcal{P}_{\text{em}}$	linear momentum density associated with the fields of the electron vortex beam
$\mathbf{P}_{\text{em}}$	global electromagnetic linear momentum of the electron vortex beam
p	radial index
$\mathbf{p}$	(canonical) linear momentum vector or canonical linear momentum operator in quantum formalism
$\mathbf{p}^{\text{kin}}$	(kinetic) linear momentum vector operator $(=\mathbf{p}-e\mathbf{A})$
$\hat{\mathbf{p}}$	electron four momentum operator
ϕ	azimuthal variable in cylindrical polar coordinates
$\hat{\boldsymbol{\phi}}$	unit vector in the azimuthal direction
φ	magnetic flux
Φ	electrostatic potential
$\psi(\rho,\phi,z)$	electron vortex wave function in cylindrical coordinates
$\psi^{\text{LG}}_{p,l}$	wave function of Laguerre-Gaussian electron vortex beam of winding number l and radial index p
ψ^{B}_{l}	wave function of Bessel electron vortex beam of winding number l
ψ^{LG}_{B}	wave function of electron vortex wave function in a constant magnetic field B
ψ^{AB}	wave function of electron vortex wave function threading a single magnetic flux
$\psi^{tB}_{p,l}$	wave function of truncated Bessel beam of winding number l and radial index p
Ψ	four-component relativistic wave function of an electron vortex beam
q	topological order of defects in liquid crystal
ρ	in-plane radial variable in cylindrical polar coordinates
$\rho_m(\mathbf{r},t)$	mass density $[=mn(\mathbf{r},t)]$
$\rho_e(\mathbf{r},t)$	charge density $[=en(\mathbf{r},t)]$
$\hat{\boldsymbol{\rho}}$	unit vector in the in-plane radial direction
$\mathbf{r}(\rho,\phi,z)$	position vector in cylindrical coordinates
ρ_m	radius of maximum intensity of the vortex beam
R_{max}	radius of the aperture or mask
$R(z)$	curvature of the wave front of a Gaussian beam
$\mathbf{S}$	spin half angular momentum vector operator
$S(t)$	an odd, self-adjoint operator used in Foldy and Wouthuysen transform
s	spin quantum number
Σ	helicity of the beam
σ_i	ith component of Pauli matrix
$\sigma_{\mu\nu}$	spin tensor
θ	angle of the cone of Bessel plane waves
$\Theta(x)$	Heaviside step function
$u(\rho,z)$	transverse mode function
$w(z)$	beam radius at coordinate z from focus plane
w_0	beam radius at focus
w_B	beam width in the presence of magnetic field
$\mathbf{w}$	two component spinor characterizing the electron polarization in the rest frame with $E=m$.
ξ	spin-orbit coupling constant
z	z variable in cylindrical polar coordinates
$\hat{\mathbf{z}}$	unit vector in the z direction
z_R	Rayleigh range of the focused beam
z_B	magnetic Rayleigh range

ACKNOWLEDGMENTS

The authors thank the UK Engineering and Physical Sciences Research Council (EPSRC) for financially supporting our own research in this area (Grant No. EP/J022098/1).

REFERENCES

Abramowitz, M., and I. A. Stegun, 1972, "Handbook of mathematical functions: with formulas, graphs, and mathematical tables," Technical Report, National Bureau of Standards Applied Mathematics Series 55, 9th ed.

Aharonov, Y., and D. Bohm, 1959, "Significance of Electromagnetic Potentials in the Quantum Theory," Phys. Rev. **115**, 485–491.
Airy, G. B., 1834, "On the Diffraction of an Object-glass with Circular Aperture," Trans. Cambridge Philos. Soc. **5**, 283–291.
Alexandrescu, A., E. Di Fabrizio, and D. Cojoc, 2005, "Electronic and centre of mass transitions driven by LaguerreGaussian beams," J. Opt. B **7**, 87–92.
Allen, L., M. Babiker, W. K. Lai, and V. E. Lembessis, 1996, "Atom dynamics in multiple Laguerre-Gaussian beams," Phys. Rev. A **54**, 4259–4270.
Allen, L., Stephen M. Barnett, and Miles J. Padgett, 2003, *Optical Angular Momentum* (Institute of Physics Pub., Bristol).
Allen, L., M. W. Beijersbergen, R. J. C. Spreeuw, and J. P. Woerdman, 1992, "Orbital angular momentum of light and the transformation of Laguerre-Gaussian laser modes," Phys. Rev. A **45**, 8185–8189.
Allen, L., V. E. Lembessis, and M. Babiker, 1996, "Spin-orbit coupling in free-space Laguerre-Gaussian light beams," Phys. Rev. A **53**, R2937–R2939.
Allen, L., M. J. Padgett, and M. Babiker, 1999, "The Orbital Angular Momentum of Light," in *Progress in Optics*, Vol. XXXIV, pp. 291–372.
Allen, L. J., H. M. Faulkner, K. a. Nugent, M. P. Oxley, and D. Paganin, 2001, "Phase retrieval from images in the presence of first-order vortices," Phys. Rev. E **63**, 037602..
Andersen, M., C. Ryu, Pierre Cladé, Vasant Natarajan, A. Vaziri, K. Helmerson, and W. Phillips, 2006, "Quantized Rotation of Atoms from Photons with Orbital Angular Momentum," Phys. Rev. Lett. **97**, 170406.
Andrews, D. L., L. C. Dávila Romero, and M. Babiker, 2004, "On optical vortex interactions with chiral matter," Opt. Commun. **237**, 133–139.
Andrews, David L., and Mohamed Babiker, 2012, *The Angular Momentum of Light*, edited by David L. Andrews and Mohamed Babiker (Cambridge University Press, Cambridge, UK).
Araoka, F., T. Verbiest, K. Clays, and A. Persoons, 2005, "Interactions of twisted light with chiral molecules: An experimental investigation," Phys. Rev. A **71**, 055401.
Asenjo-Garcia, A., and F. J. García de Abajo, 2014, "Dichroism in the Interaction between Vortex Electron Beams, Plasmons, and Molecules," Phys. Rev. Lett. **113**, 066102.
Babiker, M., C. Bennett, D. Andrews, and L. Dávila Romero, 2002, "Orbital Angular Momentum Exchange in the Interaction of Twisted Light with Molecules," Phys. Rev. Lett. **89**, 143601.
Babiker, M., W. L. Power, and L. Allen, 1994, "Light-induced Torque on Moving Atoms," Phys. Rev. Lett. **73**, 1239–1242.
Babiker, M., J. Yuan, and V. E. Lembessis, 2015, "Electron vortex beams subject to static magnetic fields," Phys. Rev. A **91**, 013806.
Balzer, Bizan N., Markus Gallei, Moritz V. Hauf, Markus Stallhofer, Lorenz Wiegleb, Alexander Holleitner, Matthias Rehahn, and Thorsten Hugel, 2013, "Nanoscale Friction Mechanisms at Solid-Liquid Interfaces," Angew. Chem., Int. Ed. Engl. **52**, 6541–6544.
Bandyopadhyay, Pratul, Banasri Basu, and Debashree Chowdhury, 2014, "The geometric phase and the geometrodynamics of relativistic electron vortex beams," Proc. R. Soc. A **470**, 20130525.
Bandyopadhyay, Pratul, Banasri Basu, and Debashree Chowdhury, 2015, "Relativistic Electron Vortex Beams in a Laser Field," Phys. Rev. Lett. **115**, 194801.
Bandyopadhyay, Pratul, Banasri Basu, and Debashree Chowdhury, 2016, "Unified Approach towards the Dynamics of Optical and Electron Vortex Beams," Phys. Rev. Lett. **116**, 144801.
Bandyopadhyay, Pratul, Banasri Basu, and Debashree Chowdhury, 2017, "Geometric phase and fractional orbital-angular-momentum states in electron vortex beams," Phys. Rev. A **95**, 013821.
Baranek, M., and Z. Bouchal, 2013, "Rotating vortex imaging implemented by a quantized spiral phase modulation," J. Eur. Opt. Soc. **8**, 13017.
Barnett, Stephen M., 2017, "Relativistic Electron Vortices," Phys. Rev. Lett. **118**, 114802.
Barnett, Stephen M., and L. Allen, 1994, "Orbital angular momentum and nonparaxial light beams," Opt. Commun. **110**, 670–678.
Barreiro, S., and J. W. R. Tabosa, 2003, "Generation of Light Carrying Orbital Angular Momentum via Induced Coherence Grating in Cold Atoms," Phys. Rev. Lett. **90**, 133001.
Batson, P. E., N. Dellby, and O. L. Krivanek, 2002, "Sub-ångstrom resolution using aberration corrected electron optics," Nature (London) **418**, 617–620.
Béché, A., R. Juchtmans, and J. Verbeeck, 2017, "Efficient creation of electron vortex beams for high resolution STEM imaging," Ultramicroscopy **178**, 12–19.
Béché, Armand, Ruben van Boxem, Gustaaf Van Tendeloo, and Jo Verbeeck, 2013, "Magnetic monopole field exposed by electrons," Nat. Phys. **10**, 26–29.
Beijersbergen, M. W., L. Allen, H. E. L. O. van der Veen, and J. P. Woerdman, 1993, "Astigmatic laser mode converters and transfer of orbital angular momentum," Opt. Commun. **96**, 123–132.
Bérard, Alain, and Hervé Mohrbach, 2006, "Spin Hall effect and Berry phase of spinning particles," Phys. Lett. A **352**, 190–195.
Berkhout, Gregorius, Martin Lavery, Johannes Courtial, Marco Beijersbergen, and Miles Padgett, 2010, "Efficient Sorting of Orbital Angular Momentum States of Light," Phys. Rev. Lett. **105**, 153601.
Berkhout, Gregorius C. G., and Marco W. Beijersbergen, 2008, "Method for Probing the Orbital Angular Momentum of Optical Vortices in Electromagnetic Waves from Astronomical Objects," Phys. Rev. Lett. **101**, 100801.
Berry, M. V., 2004, "Optical vortices evolving from helicoidal integer and fractional phase steps," J. Opt. A **6**, 259–268.
Berry, M. V., and M. R. Dennis, 2007, "Topological events on wave dislocation lines: birth and death of loops, and reconnection," J. Phys. A **40**, 65–74.
Berry, M. V., and M. R. Dennis, 2012, "Reconnections of wave vortex lines," Eur. J. Phys. **33**, 723–731.
Bhattacharyya, Somnath, Christoph T. Koch, and Manfred Rühle, 2006, "Projected potential profiles across interfaces obtained by reconstructing the exit face wave function from through focal series," Ultramicroscopy **106**, 525–538.
Bialynicki-Birula, Iwo, and Zofia Bialynicka-Birula, 2001, "Motion of vortex lines in nonlinear wave mechanics," Phys. Rev. A **65**, 014101.
Bialynicki-Birula, Iwo, and Zofia Bialynicka-Birula, 2017, "Relativistic Electron Wave Packets Carrying Angular Momentum," Phys. Rev. Lett. **118**, 114801.
Bialynicki-Birula, Iwo, Zofia Bialynicka-Birula, and Cezary Śliwa, 2000, "Motion of vortex lines in quantum mechanics," Phys. Rev. A **61**, 032110.
Bialynicki-Birula, Iwo, Tomasz Mloduchowski, Tomasz Radozycki, and Cezary Śliwa, 2001, "Vortex Lines in Motion," Acta Phys. Pol. A **100**, 29–41.
Bialynicki-Birula, Iwo, and Tomasz Radożycki, 2006, "Pinning and transport of cyclotron (Landau) orbits by electromagnetic vortices," Phys. Rev. A **73**, 052114.
Bjorken, J. D., and S. D. Drell, 1964, *Relativistic Quantum Mechanics* (Mcgraw-Hill College, New York).

Blackburn, A. M., and J. C. Loudon, 2014, "Vortex beam production and contrast enhancement from a magnetic spiral phase plate," Ultramicroscopy **136**, 127–143.

Bliokh, K. Y., *et al.*, 2017, "Theory and applications of free-electron vortex states," Phys. Rep. **690**, 1–70.

Bliokh, Konstantin, Yury Bliokh, Sergey Savel'ev, and Franco Nori, 2007, "Semiclassical Dynamics of Electron Wave Packet States with Phase Vortices," Phys. Rev. Lett. **99**, 190404.

Bliokh, Konstantin Y., Miguel Alonso, Elena Ostrovskaya, and Andrea Aiello, 2010, "Angular momenta and spin-orbit interaction of nonparaxial light in free space," Phys. Rev. A **82**, 063825.

Bliokh, Konstantin Y., Mark R. Dennis, and Franco Nori, 2011, "Relativistic Electron Vortex Beams: Angular Momentum and Spin-Orbit Interaction," Phys. Rev. Lett. **107**, 174802.

Bliokh, Konstantin Y., Avi Niv, Vladimir Kleiner, and Erez Hasman, 2008, "Geometrodynamics of spinning light," Nat. Photonics **2**, 748–753.

Bliokh, Konstantin Y., and Franco Nori, 2012a, "Relativistic Hall Effect," Phys. Rev. Lett. **108**, 120403.

Bliokh, Konstantin Y., and Franco Nori, 2012b, "Spatiotemporal vortex beams and angular momentum," Phys. Rev. A **86**, 033824.

Bliokh, Konstantin Y., Peter Schattschneider, Jo Verbeeck, and Franco Nori, 2012, "Electron Vortex Beams in a Magnetic Field: A New Twist on Landau Levels and Aharonov-Bohm States," Phys. Rev. X **2**, 041011.

Bliokh, Konstantin Yu., 2006, "Geometrical Optics of Beams with Vortices: Berry Phase and Orbital Angular Momentum Hall Effect," Phys. Rev. Lett. **97**, 043901.

Bormuth, Volker, Vladimir Varga, Jonathon Howard, and E. Schaffer, 2009, "Protein Friction Limits Diffusive and Directed Movements of Kinesin Motors on Microtubules," Science **325**, 870–873.

Born, M., E. Wolf, M. Borm, and E. Wolf, 1997, *Optica Acta: International Journal of Optics* (Cambridge University Press, Cambridge, UK).

Bosman, Michel, Vicki J. Keast, Masashi Watanabe, Abbas I. Maaroof, and Michael B. Cortie, 2007, "Mapping surface plasmons at the nanometre scale with an electron beam," Nanotechnology **18**, 165505.

Cai, Xinlun, Jianwei Wang, Michael J. Strain, Benjamin Johnson-Morris, Jiangbo Zhu, Marc Sorel, Jeremy L. O'Brien, Mark G. Thompson, and Siyuan Yu, 2012, "Integrated Compact Optical Vortex Beam Emitters," Science **338**, 363–366.

Cardano, Filippo, Ebrahim Karimi, Sergei Slussarenko, Lorenzo Marrucci, Corrado de Lisio, and Enrico Santamato, 2012, "Polarization pattern of vector vortex beams generated by q-plates with different topological charges," Appl. Opt. **51**, C1.

Carra, Paolo, B. T. Thole, Massimo Altarelli, and Xindong Wang, 1993, "X-ray circular dichroism and local magnetic fields," Phys. Rev. Lett. **70**, 694–697.

Chowdhury, Debashree, Banasri Basu, and Pratul Bandyopadhyay, 2015, "Electron vortex beams in a magnetic field and spin filter," Phys. Rev. A **91**, 033812.

Clark, Charles W., Roman Barankov, Michael G. Huber, Muhammad Arif, D. G. Cory, and Dmitry a. Pushin, 2015, "Controlling neutron orbital angular momentum," Nature (London) **525**, 504–506.

Clark, L., a. Béché, G. Guzzinati, and J. Verbeeck, 2014, "Quantitative measurement of orbital angular momentum in electron microscopy," Phys. Rev. A **89**, 053818.

Clark, L., A. Béché, G. Guzzinati, A. Lubk, M. Mazilu, R. van Boxem, and J. Verbeeck, 2013, "Exploiting Lens Aberrations to Create Electron-Vortex Beams," Phys. Rev. Lett. **111**, 064801.

Clark, Laura, S. Lloyd, Mohamed Babiker, and Jun Yuan, 2012, "Electron Beams with a Twist," J. Phys. Conf. Ser. **371**, 012005.

Coullet, P., L. Gil, and F. Rocca, 1989, "Optical vortices," Opt. Commun. **73**, 403–408.

Courtial, J., and M. Padgett, 1999, "Performance of a cylindrical lens mode converter for producing LaguerreGaussian laser modes," Opt. Commun. **159**, 13–18.

Curtis, Jennifer E., and David G. Grier, 2003, "Structure of optical vortices.," Phys. Rev. Lett. **90**, 133901.

Danev, R., H. Okawara, N. Usuda, K. Kametani, and K. Nagayama, 2002, "A Novel Phase-contrast Transmission Electron Microscopy Producing High-contrast Topographic Images of Weak objects," J. Biol. Phys. **28**, 627–635.

Dholakia, Kishan, Michael Macdonald, Gabriel Spalding, and Michael Macdonald, 2002, "Optical tweezers: the next generation," Phys. World **15**, 31–35.

Donoso, G., C. L. Ladera, and P. Martín, 2009, "Magnet fall inside a conductive pipe: motion and the role of the pipe wall," Eur. J. Phys. **30**, 855.

Donoso, Guillermo, Celso L. Ladera, and Pablo Martín, 2011, "Damped fall of magnets inside a conducting pipe," Am. J. Phys. **79**, 193.

Durnin, J., J. J. Miceli, Jr., and J. H. Eberly, 1987, "Diffraction-free beams," Phys. Rev. Lett. **58**, 1499–1501.

Dwyer, C., C. B. Boothroyd, S. L. Y. Chang, and R. E. Dunin-Borkowski, 2015, "Three-wave electron vortex lattices for measuring nanofields," Ultramicroscopy **148**, 25–30.

Edström, Alexander, Axel Lubk, and Ján Rusz, 2016a, "Elastic Scattering of Electron Vortex Beams in Magnetic Matter," Phys. Rev. Lett. **116**, 127203.

Edström, Alexander, Axel Lubk, and Ján Rusz, 2016b, "Magnetic effects in the paraxial regime of elastic electron scattering," Phys. Rev. B **94**, 174414.

Emile, Olivier, Christian Brousseau, Janine Emile, Ronan Niemiec, Kouroch Madhjoubi, and Bo Thide, 2014, "Electromagnetically Induced Torque on a Large Ring in the Microwave Range," Phys. Rev. Lett. **112**, 053902.

Enkrich, C., M. Wegener, S. Linden, S. Burger, L. Zschiedrich, F. Schmidt, J. Zhou, Th. Koschny, and C. Soukoulis, 2005, "Magnetic Metamaterials at Telecommunication and Visible Frequencies," Phys. Rev. Lett. **95**, 203901.

Erni, Rolf, Marta Rossell, Christian Kisielowski, and Ulrich Dahmen, 2009, "Atomic-Resolution Imaging with a Sub-50-pm Electron Probe," Phys. Rev. Lett. **102**, 096101.

Falvo, Michael R., and Richard Superfine, 2000, "Mechanics and friction at the nanometer scale," J. Nanopart. Res. **2**, 237–248.

Faraday, M., 1936, *Faraday's Diary IV*, edited by T. Martin (G. Bell and Sons, London).

Feng, Simin, and Herbert G. Winful, 2001, "Physical origin of the Gouy phase shift," Opt. Lett. **26**, 485–487.

Fetter, A. L., 2001, "Vortices in a trapped dilute Bose-Einstein condensate," J. Phys. Condens. Matter **13**, R135–R194.

Foldy, Leslie L., and Siegfried a. Wouthuysen, 1950, "On the Dirac Theory of Spin 1/2 Particles and Its Non-Relativistic Limit," Phys. Rev. **78**, 29–36.

Franke-Arnold, Sonja, Les Allen, and Miles Padgett, 2008, "Advances in optical angular momentum," Laser Photonics Rev. **2**, 299–313.

Franke-Arnold, Sonja, Stephen M. Barnett, Eric Yao, Jonathan Leach, Johannes Courtial, and Miles Padgett, 2004, "Uncertainty principle for angular position and angular momentum," New J. Phys. **6**, 103–103.

Franke-Arnold, Sonja, Graham Gibson, Robert W. Boyd, and Miles J. Padgett, 2011, "Rotary photon drag enhanced by a slow-light medium," Science **333**, 65–67.

Freund, Isaac, 1999, "Critical point explosions in two-dimensional wave fields," Opt. Commun. **159**, 99–117.
Fürhapter, Severin, Alexander Jesacher, Stefan Bernet, and Monika Ritsch-Marte, 2005, "Spiral phase contrast imaging in microscopy," Opt. Express **13**, 689–694.
Gabor, D., 1948, "A new microscopic principle," Nature (London) **161**, 777.
Galajda, Péter, and Pál Ormos, 2001, "Complex micromachines produced and driven by light," Appl. Phys. Lett. **78**, 249–251.
Gallatin, Gregg M., and Ben McMorran, 2012, "Propagation of vortex electron wave functions in a magnetic field," Phys. Rev. A **86**, 012701.
Giammanco, F., A. Perona, P. Marsili, F. Conti, F. Fidecaro, S. Gozzini, and A. Lucchesini, 2017, "Influence of the photon orbital angular momentum on electric dipole transitions: negative experimental evidence," Opt. Lett. **42**, 219.
Gnanavel, T., J. Yuan, and M. Babiker, 2012, "Observation of gold nanoparticles movements under sub-10 nm vortex electron beams in an aberration corrected TEM," in *Proceedings of the 15th European Microscopy Congresss*, ii (Royal Microscopy Society, Manchester, UK).
Greenshields, Colin, Robert L. Stamps, and Sonja Franke-Arnold, 2012, "Vacuum Faraday effect for electrons," New J. Phys. **14**, 103040.
Greenshields, Colin R., Robert L. Stamps, Sonja Franke-Arnold, and Stephen M. Barnett, 2014, "Is the Angular Momentum of an Electron Conserved in a Uniform Magnetic Field?" Phys. Rev. Lett. **113**, 240404.
Grier, David G., 2003, "A revolution in optical manipulation," Nature (London) **424**, 810–816.
Grillo, Vincenzo, Gian Carlo Gazzadi, Ebrahim Karimi, Erfan Mafakheri, Robert W. Boyd, and Stefano Frabboni, 2014, "Highly efficient electron vortex beams generated by nanofabricated phase holograms," Appl. Phys. Lett. **104**, 043109.
Grillo, Vincenzo, Gian Carlo Gazzadi, Erfan Mafakheri, Stefano Frabboni, Ebrahim Karimi, and Robert W. Boyd, 2015, "Holographic Generation of Highly Twisted Electron Beams," Phys. Rev. Lett. **114**, 034801.
Grillo, Vincenzo, Jérémie Harris, Gian Carlo Gazzadi, Roberto Balboni, Erfan Mafakheri, Mark R Dennis, Stefano Frabboni, and Robert W Boyd, 2016, "Generation and Application of Bessel Beams in Electron Microscopy," Ultramicroscopy **166**, 48–60.
Grillo, Vincenzo, Ebrahim Karimi, Gian Carlo Gazzadi, Stefano Frabboni, Mark R. Dennis, and Robert W. Boyd, 2014, "Generation of Nondiffracting Electron Bessel Beams," Phys. Rev. X **4**, 011013.
Grillo, Vincenzo, Lorenzo Marrucci, Ebrahim Karimi, Riccardo Zanella, and Enrico Santamato, 2013, "Quantum simulation of a spin polarization device in an electron microscope," New J. Phys. **15**, 093026.
Guzzinati, Giulio, Laura Clark, Armand Béché, and Jo Verbeeck, 2014, "Measuring the orbital angular momentum of electron beams," Phys. Rev. A **89**, 025803.
Guzzinati, Giulio, Peter Schattschneider, Konstantin Y. Bliokh, Franco Nori, and Jo Verbeeck, 2013, "Observation of the Larmor and Gouy Rotations with Electron Vortex Beams," Phys. Rev. Lett. **110**, 093601.
Handali, Jonathan, Pratistha Shakya, and Brett Barwick, 2015, "Creating electron vortex beams with light," Opt. Express **23**, 5236.
Harris, Jérémie, Vincenzo Grillo, Erfan Mafakheri, Gian Carlo Gazzadi, Stefano Frabboni, Robert W. Boyd, and Ebrahim Karimi, 2015, "Structured quantum waves," Nat. Phys. **11**, 629–634.
Harvey, Tyler, Jordan Pierce, Amit Agrawal, Peter Ercius, Martin Linck, and Benjamin J. McMorran, 2014, "Efficient diffractive phase optics for electrons," New J. Phys. **16**, 093039.
Hasegawa, Yuya, Koh Saitoh, Nobuo Tanaka, and Masaya Uchida, 2013, "Propagation Dynamics of Electron Vortex Pairs," J. Phys. Soc. Jpn. **82**, 073402.
Hayrapetyan, Armen G., Oliver Matula, Andrea Aiello, Andrey Surzhykov, and Stephan Fritzsche, 2014, "Interaction of Relativistic Electron-Vortex Beams with Few-Cycle Laser Pulses," Phys. Rev. Lett. **112**, 134801.
Hayrapetyan, Armen G., Oliver Matula, Andrey Surzhykov, and Stephan Fritzsche, 2013, "Bessel beams of two-level atoms driven by a linearly polarized laser field," Eur. Phys. J. D **67**, 167.
He, H., M. E. J. Friese, N. R. Heckenberg, and H. Rubinsztein-Dunlop, 1995, "Direct observation of transfer of angular momentum to absorptive particles from a laser beam with a phase singularity," Phys. Rev. Lett. **75**, 826–829.
Heckenberg, N. R., R. McDuff, C. P. Smith, H. Rubinsztein-Dunlop, and M. J. Wegener, 1992, "Laser beams with phase singularities," Opt. Quantum Electron. **24**, S951–S962.
Heckenberg, N. R., R. McDuff, C. P. Smith, and a. G. White, 1992, "Generation of optical phase singularities by computer-generated holograms," Opt. Lett. **17**, 221.
Hemsing, Erik, Andrey Knyazik, Michael Dunning, Dao Xiang, Agostino Marinelli, Carsten Hast, and James B. Rosenzweig, 2013, "Coherent optical vortices from relativistic electron beams," Nat. Phys. **9**, 549–553.
Herman, R. M., and T. a. Wiggins, 1991, "Production and uses of diffractionless beams," J. Opt. Soc. Am. A **8**, 932.
Hickmann, J. M., E. J. S. Fonseca, W. C. Soares, and S. Chávez-Cerda, 2010, "Unveiling a Truncated Optical Lattice Associated with a Triangular Aperture Using Light's Orbital Angular Momentum," Phys. Rev. Lett. **105**, 053904.
Hörl, Anton, Andreas Trügler, and Ulrich Hohenester, 2013, "Tomography of Particle Plasmon Fields from Electron Energy Loss Spectroscopy," Phys. Rev. Lett. **111**, 076801.
Idrobo, Juan C., and Stephen J. Pennycook, 2011, "Vortex beams for atomic resolution dichroism," J. Electron Microsc. **60**, 295–300.
Ivanov, I. P., D. Seipt, A. Surzhykov, and S. Fritzsche, 2016, "Elastic scattering of vortex electrons provides direct access to the Coulomb phase," Phys. Rev. D **94**, 076001.
Ivanov, I. P., and V. G. Serbo, 2011, "Scattering of twisted particles: Extension to wave packets and orbital helicity," Phys. Rev. A **84**, 033804.
Ivanov, Igor P., 2012a, "Creation of two vortex-entangled beams in a vortex-beam collision with a plane wave," Phys. Rev. A **85**, 033813.
Ivanov, Igor P., 2012b, "Measuring the phase of the scattering amplitude with vortex beams," Phys. Rev. D **85**, 076001.
Ivanov, Igor P., and Dmitry V. Karlovets, 2013a, "Detecting Transition Radiation from a Magnetic Moment," Phys. Rev. Lett. **110**, 264801.
Ivanov, Igor P., and Dmitry V. Karlovets, 2013b, "Polarization radiation of vortex electrons with large orbital angular momentum," Phys. Rev. A **88**, 043840.
Jáuregui, R., 2004, "Rotational effects of twisted light on atoms beyond the paraxial approximation," Phys. Rev. A **70**, 033415.
Jentschura, U. D., and V. G. Serbo, 2011, "Compton upconversion of twisted photons: backscattering of particles with non-planar wave functions," Eur. Phys. J. C **71**, 1571.
Jesacher, Alexander, Severin Fürhapter, Stefan Bernet, and Monika Ritsch-Marte, 2005, "Shadow Effects in Spiral Phase Contrast Microscopy," Phys. Rev. Lett. **94**, 233902.

Jordan, J. A., P. M. Hirsch, L. B. Lesem, and D. L. Van Rooy, 1970, "Kinoform Lenses," Appl. Opt. **9**, 1883.

Juchtmans, Roeland, Armand Béché, Artem Abakumov, Maria Batuk, and Jo Verbeeck, 2015, "Using electron vortex beams to determine chirality of crystals in transmission electron microscopy," Phys. Rev. B **91**, 094112.

Juchtmans, Roeland, Giulio Guzzinati, and Jo Verbeeck, 2016, "Extension of Friedel's law to vortex-beam diffraction," Phys. Rev. A **94**, 033858.

Juchtmans, Roeland, and Jo Verbeeck, 2016, "Local orbital angular momentum revealed by spiral-phase-plate imaging in transmission-electron microscopy," Phys. Rev. A **93**, 023811.

Kanaya, Koichi, Hisazo Kawakatsu, Kazuo Ito, and Haruo Yotsumoto, 1958, "Experiment on the electron phase microscope," J. Appl. Phys. **29**, 1046–1049.

Karimi, Ebrahim, Lorenzo Marrucci, Vincenzo Grillo, and Enrico Santamato, 2012, "Spin-to-Orbital Angular Momentum Conversion and Spin-Polarization Filtering in Electron Beams," Phys. Rev. Lett. **108**, 044801.

Karimi, Ebrahim, Sebastian A. Schulz, Israel De Leon, Hammam Qassim, Jeremy Upham, and Robert W. Boyd, 2014, "Generating optical orbital angular momentum at visible wavelengths using a plasmonic metasurface," Light Sci. Appl. **3**, e167.

Karimi, Ebrahim, Gianluigi Zito, Bruno Piccirillo, Lorenzo Marrucci, and Enrico Santamato, 2007, "Hypergeometric-Gaussian modes," Opt. Lett. **32**, 3053–3055.

Karlovets, Dmitry, 2016, "Probing phase of a scattering amplitude beyond the plane-wave approximation," Europhys. Lett. **116**, 31001.

Karlovets, Dmitry V., 2012, "Electron with orbital angular momentum in a strong laser wave," Phys. Rev. A **86**, 062102.

Khoury, A. Z., and P. Milman, 2011, "Quantum teleportation in the spin-orbit variables of photon pairs," Phys. Rev. A **83**, 060301.

Kirkland, Earl J., 2010, *Advanced Computing in Electron Microscopy* (Springer, Boston).

Kogelnik, H., and T. Li, 1966, "Laser beams and resonators," Proc. IEEE **54**, 1312–1329.

Konkov, a. S., a. P. Potylitsyn, and M. S. Polonskaya, 2014, "Transition radiation of electrons with a nonzero orbital angular momentum," JETP Lett. **100**, 421–425.

Kotlyar, V. V., S. N. Khonina, A. A. Kovalev, V. A. Soifer, H. Elfstrom, and J. Turunen, 2006, "Diffraction of a plane, finite-radius wave by a spiral phase plate," Opt. Lett. **31**, 1597.

Kotlyar, Victor V., Anton a. Almazov, Svetlana N. Khonina, Victor a. Soifer, Henna Elfstrom, and Jari Turunen, 2005, "Generation of phase singularity through diffracting a plane or Gaussian beam by a spiral phase plate," J. Opt. Soc. Am. A **22**, 849–861.

Kotlyar, Victor V., Alexey a. Kovalev, Roman V. Skidanov, Oleg Yu. Moiseev, and Victor a. Soifer, 2007, "Diffraction of a finite-radius plane wave and a Gaussian beam by a helical axicon and a spiral phase plate," J. Opt. Soc. Am. **24**, 1955–1964.

Krivanek, Ondrej L., Jan Rusz, Juan-Carlos Idrobo, Tracy J. Lovejoy, and Niklas Dellby, 2014, "Toward Single Mode, Atomic Size Electron Vortex Beams," Microsc. Microanal. **20**, 832–836.

Kruit, P., and M. Lenc, 1992, "Optical properties of the magnetic monopole field applied to electron microscopy and spectroscopy," J. Appl. Phys. **72**, 4505–4513.

Ladavac, Kosta, and David G. Grier, 2004, "Microoptomechanical pumps assembled and driven by holographic optical vortex arrays," Opt. Express **12**, 1144–1149.

Landau, L. D., and E. M. Lifshitz, 1977, *Quantum Mechanics Non-Relativistic Theory* (Pergamon Press, Oxford), 3rd ed.

Larocque, Hugo, Frédéric Bouchard, Vincenzo Grillo, Alicia Sit, Stefano Frabboni, Rafal E. Dunin-Borkowski, Miles J. Padgett, Robert W. Boyd, and Ebrahim Karimi, 2016, "Nondestructive Measurement of Orbital Angular Momentum for an Electron Beam," Phys. Rev. Lett. **117**, 154801.

Lax, M., W. H. Louisell, and W. B. McKnight, 1975, "From Maxwell to paraxial wave optics," Phys. Rev. A **11**, 1365–1370.

Leach, Jonathan, Johannes Courtial, Kenneth Skeldon, Stephen M. Barnett, Sonja Franke-Arnold, and Miles J. Padgett, 2004, "Interferometric Methods to Measure Orbital and Spin, or the Total Angular Momentum of a Single Photon," Phys. Rev. Lett. **92**, 013601.

Leary, C. C., M. G. Raymer, and S. J. van Enk, 2009, "Spin and orbital rotation of electrons and photons via spin-orbit interaction," Phys. Rev. A **80**, 061804.

Leary, C. C., D. Reeb, and M. G. Raymer, 2008, "Self-spin-controlled rotation of spatial states of a Dirac electron in a cylindrical potential via spinorbit interaction," New J. Phys. **10**, 103022.

Lee, Jae, Gregory Foo, Eric Johnson, and Grover Swartzlander, 2006, "Experimental Verification of an Optical Vortex Coronagraph," Phys. Rev. Lett. **97**, 053901.

Lee, W.-H., 1979, "Binary Computer Generated Holograms," Appl. Opt. **18**, 3661.

Lembessis, V., D. Ellinas, and M. Babiker, 2011, "Azimuthal Sisyphus effect for atoms in a toroidal all-optical trap," Phys. Rev. A **84**, 043422.

Lembessis, V. E., and M. Babiker, 2013, "Enhanced Quadrupole Effects for Atoms in Optical Vortices," Phys. Rev. Lett. **110**, 083002.

Lembessis, V. E., and M. Babiker, 2016, "Mechanical effects on atoms interacting with highly twisted Laguerre-Gaussian light," Phys. Rev. A **94**, 043854.

Lembessis, V. E., D. Ellinas, M. Babiker, and O. Al-Dossary, 2014, "Atom vortex beams," Phys. Rev. A **89**, 053616.

Lloyd, S. M., M. Babiker, and J. Yuan, 2012a, "Interaction of electron vortices and optical vortices with matter and processes of orbital angular momentum exchange," Phys. Rev. A **86**, 023816.

Lloyd, S. M., M. Babiker, and J. Yuan, 2013, "Mechanical properties of electron vortices," Phys. Rev. A **88**, 031802.

Lloyd, S. M., M. Babiker, J. Yuan, and C. Kerr-Edwards, 2012, "Electromagnetic Vortex Fields, Spin, and Spin-Orbit Interactions in Electron Vortices," Phys. Rev. Lett. **109**, 254801.

Lloyd, Sophia, Mohamed Babiker, and Jun Yuan, 2012b, "Quantized Orbital Angular Momentum Transfer and Magnetic Dichroism in the Interaction of Electron Vortices with Matter," Phys. Rev. Lett. **108**, 074802.

Löffler, W., Andrea Aiello, and J. P. Woerdman, 2012, "Observation of Orbital Angular Momentum Sidebands due to Optical Reflection," Phys. Rev. Lett. **109**, 113602.

Löffler, W., D. Broer, and J. Woerdman, 2011, "Circular dichroism of cholesteric polymers and the orbital angular momentum of light," Phys. Rev. A **83**, 065801.

Löfgren, André, Paul Zeiger, Vancho Kocevski, and Ján Rusz, 2016, "Influence of nuclear quantum effects on frozen phonon simulations of electron vortex beam HAADF-STEM images," Ultramicroscopy **164**, 62–69.

Lubk, Axel, Laura Clark, Giulio Guzzinati, and Jo Verbeeck, 2013, "Topological analysis of paraxially scattered electron vortex beams," Phys. Rev. A **87**, 033834.

Lubk, Axel, Giulio Guzzinati, Felix Börrnert, and Jo Verbeeck, 2013, "Transport of Intensity Phase Retrieval of Arbitrary Wave Fields Including Vortices," Phys. Rev. Lett. **111**, 173902.

MacDonald, R. P., S. A. Boothroyd, T. Okamoto, J. Chrostowski, and B. A. Syrett, 1996, "Interboard optical data distribution by Bessel beam shadowing," Opt. Commun. **122**, 169–177.

Magnusson, R., and T. K. Gaylord, 1978, "Diffraction efficiencies of thin phase gratings with arbitrary grating shape," J. Opt. Soc. Am. **68**, 806.

Mair, a., A. Vaziri, G. Weihs, and A. Zeilinger, 2001, "Entanglement of the orbital angular momentum states of photons," Nature (London) **412**, 313–316.

Marrucci, L., E. Karimi, S. Slussarenko, B. Piccirillo, E. Santamato, E. Nagali, and F. Sciarrino, 2012, "Spin-to-Orbital Optical Angular Momentum Conversion in Liquid Crystal q-Plates: Classical and Quantum Applications," Mol. Cryst. Liq. Cryst. **561**, 48–56.

Marrucci, L., C. Manzo, and D. Paparo, 2006, "Optical Spin-to-Orbital Angular Momentum Conversion in Inhomogeneous Anisotropic Media," Phys. Rev. Lett. **96**, 163905.

Marrucci, Lorenzo, 2013, "The q-plate and its future," J. Nanophoton. **7**, 078598.

Matula, O., a. G. Hayrapetyan, V. G. Serbo, A. Surzhykov, and S. Fritzsche, 2014, "Radiative capture of twisted electrons by bare ions," New J. Phys. **16**, 053024.

McGloin, D., and K. Dholakia, 2005, "Bessel beams: Diffraction in a new light," Contemp. Phys. **46**, 15–28.

McMorran, B. J., Amit Agrawal, I. M. M. Anderson, A. A. A. Herzing, H. J. J. Lezec, J. J. J. McClelland, and John Unguris, 2011, "Electron Vortex Beams with High Quanta of Orbital Angular Momentum," Science **331**, 192–195.

McMorran, Benjamin J., Amit Agrawal, Peter A. Ercius, Vincenzo Grillo, Andrew A. Herzing, Tyler R. Harvey, Martin Linck, and Jordan S. Pierce, 2017, "Origins and demonstrations of electrons with orbital angular momentum," Phil. Trans. R. Soc. A **375**, 20150434.

Midgley, Paul A., and Rafal E. Dunin-Borkowski, 2009, "Electron tomography and holography in materials science. Nat. Mater. **8**, 271–80.

Mo, Yifei, Kevin T. Turner, and Izabela Szlufarska, 2009, "Friction laws at the nanoscale," Nature (London) **457**, 1116–1119.

Mohammadi, Zeinab, Cole P. Van Vlack, Stephen Hughes, Jens Bornemann, and Reuven Gordon, 2012, "Vortex electron energy loss spectroscopy for near-field mapping of magnetic plasmons," Opt. Express **20**, 15024.

Molina-Terriza, Gabriel, Juan P. Torres, and Lluis Torner, 2007, "Twisted photons," Nat. Phys. **3**, 305–310.

Mousley, Michael, Gnanavel Thirunavukkarasu, Mohamed Babiker, and Jun Yuan, 2015, "C-shaped electron beams: design, experimental production and application," Proc. SPIE **9581**, 95810C.

Mutzafi, Maor, Ido Kaminer, Gal Harari, and Mordechai Segev, 2014, "Non-Linear Shape Preserving Electron-Beams," in *CLEO: 2014*, 2 (OSA, Washington, D.C.), p. FM3D.7.

Nagayama, Kuniaki, 2011, "Another 60 years in electron microscopy: development of phase-plate electron microscopy and biological applications," J. Electron Microsc. **60**, S43–S62.

Nelayah, Jaysen, Mathieu Kociak, Odile Stéphan, F. Javier García de Abajo, Marcel Tencé, Luc Henrard, Dario Taverna, Isabel Pastoriza-Santos, Luis M. Liz-Marzán, and Christian Colliex, 2007, "Mapping surface plasmons on a single metallic nanoparticle," Nat. Phys. **3**, 348–353.

Nienhuis, G., J. P. Woerdman, and I. Kuščer, 1992, "Magnetic and mechanical Faraday effects," Phys. Rev. A **46**, 7079–7092.

Niermann, T., J. Verbeeck, and M. Lehmann, 2014, "Creating arrays of electron vortices," Ultramicroscopy **136**, 165–170.

Nye, J. F., 2006, "Dislocation lines in the hyperbolic umbilic diffraction catastrophe," Proc. R. Soc. A **462**, 2299–2313.

Nye, J. F., and M. V. Berry, 1974, "Dislocations in Wave Trains," Proc. R. Soc. A **336**, 165–190.

O'Holleran, Kevin, Mark R. Dennis, Florian Flossmann, and Miles J. Padgett, 2008, "Fractality of Light's Darkness," Phys. Rev. Lett. **100**, 053902.

O'Neil, A. T., I. MacVicar, L. Allen, and M. J. Padgett, 2002, "Intrinsic and Extrinsic Nature of the Orbital Angular Momentum of a Light Beam," Phys. Rev. Lett. **88**, 053601.

Padgett, M., 1996, "An experiment to observe the intensity and phase structure of LaguerreGaussian laser modes," Am. J. Phys. **64**, 77.

Pepino, R. a., J. Cooper, D. Meiser, D. Z. Anderson, and M. J. Holland, 2010, "Open quantum systems approach to atomtronics," Phys. Rev. A **82**, 013640.

Petersen, T. C., D. M. Paganin, M. Weyland, T. P. Simula, S. A. Eastwood, and M. J. Morgan, 2014, "Unifying interpretations of the Gouy phase anomaly for electron waves," Phys. Rev. A **89**, 063801.

Petersen, T. C., M. Weyland, D. M. Paganin, T. P. Simula, S. a. Eastwood, and M. J. Morgan, 2013, "Electron Vortex Production and Control Using Aberration Induced Diffraction Catastrophes," Phys. Rev. Lett. **110**, 033901.

Podolskiy, V. A., A. K. Sarychev, and V. Shalaev, 2002, "Plasmon modes in metal nanowires and left-handed materials," J. Nonlinear Opt. Phys. Mater. **11**, 65–74.

Pohl, Darius, Jan Rusz, Jakob Spiegelberg, Sebastian Schneider, Peter Tiemeijer, Kornelius Nielsch, and Bernd Rellinghaus, 2016, "Towards atomic magnetic measurements with single electron vortex beams on nanocubes," in *Proceedings of the European Microscopy Congress 2016* (Wiley-VCH Verlag GmbH & Co. KGaA, Weinheim, Germany), pp. 907–908.

Pohl, Darius, Sebastian Schneider, Jan Rusz, and Bernd Rellinghaus, 2015, "Electron vortex beams prepared by a spiral aperture with the goal to measure EMCD on ferromagnetic films via STEM," Ultramicroscopy **150**, 16–22.

Qiu, Jiangdong, Changliang Ren, and Zhiyou Zhang, 2016, "Precisely measuring the orbital angular momentum of beams via weak measurement," Phys. Rev. A **93**, 063841.

Reimer, Ludwig, and Helmut Kohl, 2008, *Transmission Electron Microscopy Physics of Image Formation* (Springer, Berlin), 5th ed.

Ricci, F., W. Löffler, and M. P. van Exter, 2012, "Instability of higher-order optical vortices analyzed with a multi-pinhole interferometer," Opt. Express **20**, 22961.

Rose, H. H., 2008, "Optics of high-performance electron microscopes," Sci. Technol. Adv. Mater. **9**, 014107.

Ruffner, David B., and David G. Grier, 2012, "Optical Forces and Torques in Nonuniform Beams of Light," Phys. Rev. Lett. **108**, 173602.

Rusz, Ján, and Somnath Bhowmick, 2013, "Boundaries for Efficient Use of Electron Vortex Beams to Measure Magnetic Properties," Phys. Rev. Lett. **111**, 105504.

Rusz, Ján, Somnath Bhowmick, Mattias Eriksson, and Nikolaj Karlsson, 2014, "Scattering of electron vortex beams on a magnetic crystal: Towards atomic-resolution magnetic measurements," Phys. Rev. B **89**, 134428.

Saitoh, Koh, Yuya Hasegawa, Kazuma Hirakawa, Nobuo Tanaka, and Masaya Uchida, 2013, "Measuring the Orbital Angular Momentum of Electron Vortex Beams Using a Forked Grating," Phys. Rev. Lett. **111**, 074801.

Saitoh, Koh, Yuya Hasegawa, Nobuo Tanaka, and Masaya Uchida, 2012, "Production of electron vortex beams carrying large orbital angular momentum using spiral zone plates," J. Electron Microsc. **61**, 171.

Saleh, B. E. A., and M. C. Teich, 1991, *Fundementals of photonics* (Wiley Interscience, New York).
Sarychev, Andrey K., Gennady Shvets, and Vladimir M. Shalaev, 2006, "Magnetic plasmon resonance," Phys. Rev. E **73**, 036609.
Saslow, W. M., 1992, "Maxwell's theory of eddy currents in thin conducting sheets, and applications to electromagnetic shielding and MAGLEV," Am. J. Phys. **60**, 693–711.
Schachinger, T., S. Löffler, A. Steiger-Thirsfeld, M. Stöger-Pollach, S. Schneider, D. Pohl, B. Rellinghaus, and P. Schattschneider, 2017, "EMCD with an electron vortex filter: Limitations and possibilities," Ultramicroscopy **179**, 15–23.
Schachinger, T., S. Löffler, M. Stöger-Pollach, and P. Schattschneider, 2015, "Peculiar rotation of electron vortex beams," Ultramicroscopy **158**, 17–25.
Schattschneider, P., V. Grillo, and D. Aubry, 2017, "Spin polarisation with electron Bessel beams," Ultramicroscopy (to be published).
Schattschneider, P., S. Löffler, M. Stöger-Pollach, and J. Verbeeck, 2014, "Is magnetic chiral dichroism feasible with electron vortices?" Ultramicroscopy **136**, 81–85.
Schattschneider, P., S. Rubino, C. Hébert, J. Rusz, J. Kuneš, P. Novák, E. Carlino, M. Fabrizioli, G. Panaccione, and G. Rossi, 2006, "Detection of magnetic circular dichroism using a transmission electron microscope," Nature (London) **441**, 486–488.
Schattschneider, P., Th. Schachinger, M. Stöger-Pollach, S. Löffler, A. Steiger-Thirsfeld, K. Y. Bliokh, and Franco Nori, 2014, "Imaging the dynamics of free-electron Landau states," Nat. Commun. **5**, 4586.
Schattschneider, P., M. Stöger-Pollach, and J. Verbeeck, 2012, "Novel Vortex Generator and Mode Converter for Electron Beams," Phys. Rev. Lett. **109**, 084801.
Schattschneider, P., and J. Verbeeck, 2011, "Theory of free electron vortices," Ultramicroscopy **111**, 1461–1468.
Schattschneider, Peter, Bernhard Schaffer, Inga Ennen, and Johan Verbeeck, 2012, "Mapping spin-polarized transitions with atomic resolution," Phys. Rev. B **85**, 134422.
Schmidt, L. Ph. H., C. Goihl, D. Metz, H. Schmidt-Böcking, R. Dörner, S. Yu. Ovchinnikov, J. H. Macek, and D. R. Schultz, 2014, "Vortices associated with the wave function of a single electron emitted in slow ion-atom collisions," Phys. Rev. Lett. **112**, 083201.
Seaman, B. T., M. Krämer, D. Z. Anderson, and M. J. Holland, 2007, "Atomtronics: Ultracold-atom analogs of electronic devices," Phys. Rev. A **75**, 023615.
Seipt, D., a. Surzhykov, and S. Fritzsche, 2014, "Structured x-ray beams from twisted electrons by inverse Compton scattering of laser light," Phys. Rev. A **90**, 012118.
Serbo, V., I. P. Ivanov, S. Fritzsche, D. Seipt, and a. Surzhykov, 2015, "Scattering of twisted relativistic electrons by atoms," Phys. Rev. A **92**, 012705.
Shiloh, Roy, Yossi Lereah, Yigal Lilach, and Ady Arie, 2014, "Sculpturing the electron wave function using nanoscale phase masks," Ultramicroscopy **144**, 26–31.
Shiloh, Roy, Yuval Tsur, Roei Remez, Yossi Lereah, Boris a. Malomed, Vladlen Shvedov, Cyril Hnatovsky, Wieslaw Krolikowski, and Ady Arie, 2015, "Unveiling the Orbital Angular Momentum and Acceleration of Electron Beams," Phys. Rev. Lett. **114**, 096102.
Speirits, Fiona C., and Stephen M. Barnett, 2013, "Do Waves Carrying Orbital Angular Momentum Possess Azimuthal Linear Momentum?" Phys. Rev. Lett. **111**, 103602.
Sueda, K., G. Miyaji, N. Miyanaga, and M. Nakatsuka, 2004, "Laguerre-Gaussian beam generated with a multilevel spiral phase plate for high intensity laser pulses," Opt. Express **12**, 3548.
Surzhykov, A., D. Seipt, V. G. Serbo, and S. Fritzsche, 2015, "Interaction of twisted light with many-electron atoms and ions," Phys. Rev. A **91**, 013403.
Swartzlander, Grover A., and Raul I. Hernandez-Aranda, 2007, "Optical Rankine Vortex and Anomalous Circulation of Light," Phys. Rev. Lett. **99**, 163901.
Takahashi, Ryuji, and Naoto Nagaosa, 2015, "Berry curvature and orbital angular momentum of electrons in angle-resolved photoemission spectroscopy," Phys. Rev. B **91**, 245133.
Tamburini, Fabrizio, Bo Thidé, Gabriel Molina-Terriza, and Gabriele Anzolin, 2011, "Twisting of light around rotating black holes," Nat. Phys. **7**, 195–197.
Thidé, B., H. Then, J. Sjöholm, K. Palmer, J. Bergman, T. D. Carozzi, Ya. N. Istomin, N. H. Ibragimov, and R. Khamitova, 2007, "Utilization of Photon Orbital Angular Momentum in the Low-Frequency Radio Domain," Phys. Rev. Lett. **99**, 087701.
Thirunavukkarasu, G., M. Mousley, M. Babiker, and J. Yuan, 2017, "Normal modes and mode transformation of pure electron vortex beams," Phil. Trans. R. Soc. A **375**, 20150438.
Thole, B. T., P. Carra, F. Sette, and G. Van der Laan, 1992, "X-ray circular dichroism as a probe of orbital magnetization," Phys. Rev. Lett. **68**, 1943–1946.
Tonomura, Akira, 1987, "Applications of electron holography," Rev. Mod. Phys. **59**, 639–669.
Turnbull, G., 1996, "The generation of free-space Laguerre-Gaussian modes at millimetre-wave frequencies by use of a spiral phase-plate," Opt. Commun. **127**, 183–188.
Uchida, Masaya, and Akira Tonomura, 2010, "Generation of electron beams carrying orbital angular momentum," Nature (London) **464**, 737–9.
van Boxem, Ruben, Bart Partoens, and Jo Verbeeck, 2015, "Inelastic electron-vortex-beam scattering," Phys. Rev. A **91**, 032703.
van Boxem, Ruben, Bart Partoens, and Johan Verbeeck, 2014, "Rutherford scattering of electron vortices," Phys. Rev. A **89**, 032715.
van Boxem, Ruben, Jo Verbeeck, and Bart Partoens, 2013, "Spin effects in electron vortex states," Europhys. Lett. **102**, 40010.
Van Enk, S. J., and G. Nienhuis, 1994, "Commutation Rules and Eigenvalues of Spin and Orbital Angular Momentum of Radiation Fields," J. Mod. Opt. **41**, 963–977.
Velasco-Martínez, D., V. G. Ibarra-Sierra, J. C. Sandoval-Santana, J. L. Cardoso, and A. Kunold, 2016, "Singularities and internal rotational dynamics of electron beams," Phys. Rev. A **94**, 063815.
Verbeeck, J., P. Schattschneider, S. Lazar, M. Stoger-Pollach, S. Loffler, A. Steiger-Thirsfeld, and G. Van Tendeloo, 2011, "Atomic scale electron vortices for nanoresearch," Appl. Phys. Lett. **99**, 203109.
Verbeeck, J., H. Tian, and P. Schattschneider, 2010, "Production and application of electron vortex beams," Nature (London) **467**, 301–4.
Verbeeck, J. Jo., H. He Tian, and a. Béché, 2012, "A new way of producing electron vortex probes for STEM," Ultramicroscopy **113**, 83–87.
Verbeeck, Jo., Giulio Guzzinati, Laura Clark, Roeland Juchtmans, Ruben van Boxem, He Tian, Armand Béché, Axel Lubk, and Gustaaf Van Tendeloo, 2014, "Shaping electron beams for the generation of innovative measurements in the (S)TEM," C.R. Phys. **15**, 190–199.
Verbeeck, Jo., He Tian, and Gustaaf Van Tendeloo, 2013, "How to Manipulate Nanoparticles with an Electron Beam?" Adv. Mater. **25**, 1114–1117.
Wang, Yan, and Chun-Fang Li, 2011, "Bessel-Gaussian electron beams of cylindrically symmetric spin polarization," Europhys. Lett. **95**, 44001.

Williams, David B., and C. Barry Carter, 2009, *Transmission Electron Microscopy* (Springer, Boston).

Wu, Tai Tsun, and Chen Ning Yang, 1976, "Dirac monopole without strings: Monopole harmonics," Nucl. Phys. B **107**, 365–380.

Xie, L., P. Wang, and X. Q. Pan, 2014, "A perturbation theory study of electron vortices in electromagnetic fields: The case of infinitely long line charge and magnetic dipole," Micron **63**, 9–14.

Xin, Huolin L., and Haimei Zheng, 2012, "On-Column 2p Bound State with Topological Charge 1 Excited by an Atomic-Size Vortex Beam in an Aberration-Corrected Scanning Transmission Electron Microscope," Microsc. Microanal. **18**, 711–719.

Yao, Alison M., and Miles J. Padgett, 2011, "Orbital angular momentum: origins, behavior and applications," Adv. Opt. Photonics **3**, 161–204.

Yuan, J., S. M. Lloyd, and M. Babiker, 2013, "Chiral-specific electron-vortex-beam spectroscopy," Phys. Rev. A **88**, 031801.

Yuan, J., and N. K. Menon, 1997, "Magnetic linear dichroism in electron energy loss spectroscopy," J. Appl. Phys. **81**, 5087.

Yuan, Jun, 2014, "Bright electron twisters," Nature (London) **509**, 37.

Zaytsev, V. A., V. G. Serbo, and V. M. Shabaev, 2017, "Radiative recombination of twisted electrons with bare nuclei: Going beyond the Born approximation," Phys. Rev. A **95**, 012702.

Züchner, Tina, Antonio Virgilio Failla, and Alfred J. Meixner, 2011, "Light microscopy with doughnut modes: a concept to detect, characterize, and manipulate individual nanoobjects," Angew. Chem. **50**, 5274–5293.